Vacuum Arc Propulsion Systems for In Space Refuelling and Small Satellite Applications

Paul Stansell
1618458

Supervisor:
Prof. Phil Ferrer[1]

Co-supervisor:
Dr. Trevor Lafleur[2]

A dissertation submitted in fulfilment of the requirements for the degree of

Master of Science

in

Physics

in the Faculty of Science, University of the Witwatersrand, Johannesburg

5 September 2023

[1]School of Physics, University of the Witwatersrand Johannesburg
[2]School of Engineering and Information Technology, University New South Wales Canberra

Declaration

I, Paul Stansell, declare this dissertation is my own, unaided work. It is being submitted for the degree of Master of Science at the University of the Witwatersrand, Johannesburg. It has not been submitted for any degree or examination at any other university.

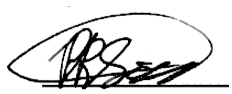

Paul Stansell

5 September 2023

"The amount of it, be sure, is merely a Scream, but sometimes a scream is better than a thesis."

Ralph Waldo Emerson

Abstract

In this work a compact and low power vacuum arc ion thruster and related circuitry were built utilising a vacuum arc thruster (VAT) as the plasma source. A number of VAT designs were tested before the final ion thruster design comprising of a modified coaxial VAT with a copper cathode and an extended anode grid to reduce peak ion currents was chosen. This design was chosen as it produced the best performance and prevented excessive grid arcing which was a problem encountered throughout this work. The final ion thruster required only one liter of volume, excluding electronics, and could be operated at an average power of less than one watt. Pulsed ion beams of up to $20 \pm 1.4mA$ of copper ions with beam energy $3.23 \pm 0.22keV$ lasting on average $320\mu s$ were produced by the system and detected by a plate downstream of the thruster. The grid system was unable to extract the large ion currents produced by the VAT which meant the overall electrical efficiency, thrust to power ratio and specific impulse were low compared to existing gas-fueled gridded ion thrusters; 2.28%, $0.474mN/kW$ and $33s$ respectively. Finally, a metallic meteorite sample was used as the cathode in a planar VAT and the ion current was measured. It was concluded that the vacuum arc ion thruster is a promising propulsion system for small satellites and has potential for refuelling from metals present in the space environment. This study adds a novel, miniature, low power and low beam voltage design to the limited literature on vacuum arc ion thrusters.

Acknowledgements

To my supervisor Phil Ferrer, for always being open to discuss a wide range of topics and always challenging me to improve my physical understanding and intuitions of any system I was working with. For not only supporting me throughout my masters, but also throughout my scientific development all the way back to grade eleven.

To Trevor Lafleur, a true plasma wizard, for all his help on the specifics and practicalities of building an ion thruster. Our discussions radically improved my physical understanding and intuitions around plasma physics. Your technical expertise in the field has been an inspiration to me.

To everyone in the physics workshop, and especially Vincent for all his help and patience with my project especially when I was fixing the vacuum pump.

To Professor Roger Gibson for his help in providing the metallic meteorite sample used in this work, and for some enlightening discussions about the meteorite composition and origins.

To Gerrard Peters, Roger Van Rensburg, Tristan Rencken and Blake Denham for their help and support on the project.

Finally, to my mom and dad, my brother and my girlfriend for all their support during this work.

This research has been supported in part by the South African National Space Agency (SANSA). The author extends his gratitude to the agency for their support.

Contents

List of Figures

List of Tables

List of Abbreviations

VAT	Vacuum Arc Thruster
VAIT	Vacuum Arc Ion Thruster
EMI	Electromagnetic Interference
accel	Acceleration (grid)
PFN	Pulse Forming Network
IGBT	Insulated Gate Bipolar Transistor
kV	kilovolt
mA	milliampere
μ**m**	micrometer
μ**s**	microsecond
km/s	kilometers per second
eV	electronvolt
m_a	atomic mass unit
amu	atomic mass unit
HV	high voltage
OOS	On-Orbit Servicing
NEA	Near Earth Asteroid
RF	Radio frequency
ECR	Electron Cyclotron Resonance
CEX	Charge Exchange (collision)
DC	Direct current
PPU	Pulsed power unit

Chapter 1

Introduction

The growing demand for small satellites with shorter development cycles and lower costs has been accompanied by a renewed interest for in space refuelling as a means of extending operational lifetimes and increasing mission capabilities. However, current ion thruster systems are not well suited to small satellites due to their expensive fuels, Herman & Unfried (2015), low fuel storage densities and various inefficiencies associated with their miniaturisation. Additionally, refuelling technologies require large and heavy propellant transfer systems, presenting a significant challenge for small satellite applications. A vacuum arc between two electrodes produces a dense, high velocity metal plasma from the cathode, Anders (2009). The thrust from this jet of plasma can be used on its own to provide a small impulse to propel spacecraft, known as a vacuum arc thruster (VAT), or the plasma can be further accelerated by an electrostatic grid system - creating a high performance gridded ion thruster known as the vacuum arc ion thruster (VAIT). Because the cathode propellant is much denser than existing ion thruster propellants and the plasma is produced in microscopic regions on the cathode surface - this ion thruster could be made much more compact than existing systems. Refuelling in space by replacing solid metal rods also appears to be simpler than other types of propellant transfer, and it is likely metals could be gathered from the space environment for this refuelling. Additionally, because the vacuum arc can be operated in pulsed mode, very low average powers are required. These factors together make the vacuum arc ion thruster a promising candidate for small satellite applications.

1.1 Electric propulsion

Electric propulsion refers to the use of electric power to propel spacecraft and satellites through space. There are several types of electric propulsion, including electrothermal, electrostatic and electromagnetic, Goebel & Katz (2008). Typically electric propulsion systems generate a plasma, which is the state of matter characterised by a high degree of ionisation and a separation of electrons from atoms or molecules to form positive ions, Piel (2017). Electrothermal propulsion relies on heating a propellant to create thrust, while electrostatic propulsion uses electric fields to accelerate plasma ions. Electromagnetic propulsion uses magnetic fields to accelerate plasma ions. In contrast to electric propulsion, chemical propulsion involves the combustion of a propellant to create thrust. While chemical propulsion is more powerful and can provide short bursts of high thrust, electric propulsion is more efficient and can operate for longer periods of time, making it more suitable for long-duration missions. One specific type of electrostatic propulsion is the gridded ion thruster, which uses a series of grids to create electric fields that accelerate plasma ions to generate thrust. The gridded ion thruster is particularly notable for its high propellant exhaust velocity, which allows for greater fuel efficiency and longer mission durations. Propellant velocities in gridded ion thrusters are typically on the order of 20-100 km/s, compared to 8-15km/s for lower exhaust velocity electric propulsion and 1-3 km/s for chemical propulsion systems. Examining the ideal rocket equation, one can immediately see the advantage of higher exhaust velocities for missions requiring large changes in velocity, Tsiolkovsky (1903),

$$\Delta V = v_e \ln \frac{m_i}{m_f} \tag{1.1}$$

where ΔV represents the required change in the spacecraft velocity, v_e is the exhaust velocity of the propellant and m_i and m_f are the spacecraft initial/launch or wet mass and final or dry mass once the spacecraft has completed its propulsive manoeuvres.

An illustrative example is to consider the effect on the spacecraft mass fraction (the ratio of wet to dry mass), of a 10X increase in exhaust velocity for the same velocity change (ΔV). Rearranging the rocket equation becomes,

$$\frac{m_i}{m_f} = \exp\left(\frac{\Delta V}{v_e}\right) \tag{1.2}$$

Contrast two spacecraft in low earth orbit (LEO) each raising their altitude to geostationary orbit (GEO), a manoeuvre typically requiring a change in velocity of $\Delta V = 3.6km/s$. Spacecraft 1 uses a high thrust chemical rocket with 3km/s exhaust velocity, and spacecraft 2 uses a high fuel efficiency gridded ion thruster with an exhaust velocity of 30km/s.

For spacecraft 1,

$$\frac{m_i}{m_f} = \exp\left(\frac{3.6}{3}\right) = 3.320 \tag{1.3}$$

and the fraction of this spacecraft's mass in LEO dedicated to fuel is:

$$\frac{m_{fuel}}{m_i} = 69.88\% \tag{1.4}$$

For spacecraft 2,

$$\frac{m_i}{m_f} = \exp\left(\frac{3.6}{30}\right) = 1.127 \tag{1.5}$$

the fraction of this spacecraft's mass in LEO dedicated to fuel is only:

$$\frac{m_{fuel}}{m_i} = 11.27\% \tag{1.6}$$

While the high thrust chemical propulsion system used on spacecraft 1 would take a much shorter time to complete this manoeuvre, this spacecraft arrives in GEO with only $\approx$ 30% of its LEO mass, whereas spacecraft 2 arrives with $\approx$ 90% of its mass in LEO. When spacecraft 1 is put into LEO it is over two thirds fuel, meaning there is much less mass for other critical satellite systems. Spacecraft 2 on the other hand, is just over 10% fuel in LEO - allowing it to be a much more capable satellite.

1.2 Gridded Ion Thrusters

Gridded ion thrusters consist of three primary components: the plasma source, the grid system and the neutraliser. The plasma source generates positive ions and negative electrons from a noble gas such as xenon or other propellant. The grid system accepts a flux of these ions, and accelerates them to high velocity to generate thrust. The neutraliser provides electrons into the high velocity ion beam, to ensure that the spacecraft does not become negatively charged. A schematic of an electron bombardment type gridded ion thruster is shown in figure 1.1. In this case the plasma is generated through electron bombardment of neutral gaseous propellant. The electron gun at the left of the figure produces electrons which spiral around magnetic field lines and impact neutral propellant atoms, turning them into ions. These ions then flow to the grid system where they are accelerated by the electric field between the grids. The positive grid is also known as the screen grid, as it screens or shields high energy ions from directly impacting the negative grid, known as the accel grid.

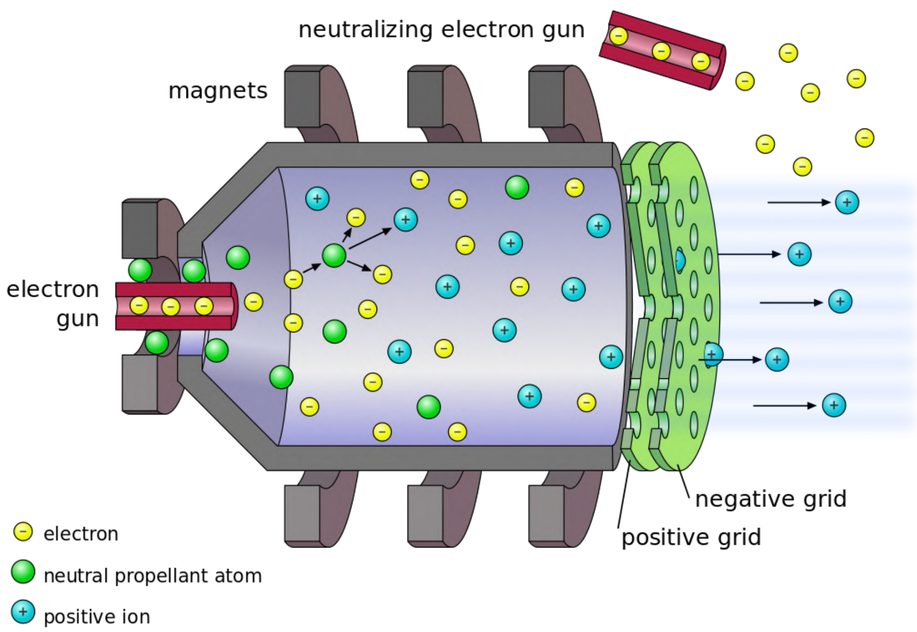

FIGURE 1.1: Schematic of a typical gridded ion thruster, Räisänen (2012)

This grid is the lowest potential that the ions encounter and so they are accelerated most as they pass through this grid. There is sometimes a third grid after the accel grid at spacecraft common potential, and this is known as the decel (deceleration) grid as the ions are decelerated as they pass through it. In order for the ions to be accelerated as they fall through the potential between the grids they must be created at high potential. This means that the entire plasma source that generates the ions is held at a high positive potential, typically several kV, relative to the spacecraft common. The accel grid is biased below spacecraft common to prevent any electrons in the beam from moving up stream into the thruster. For every ion that is accelerated through the grids, an electron is absorbed by the screen grid to maintain the electric field between the grids and this is known as the screen grid current. The screen grid current represents the total electrical ion current that is accelerated by the grid system. Some of this ion current may hit the accel grid on its way out of the thruster, and this is typically the major contribution to the total current drawn by the accel grid, known as the accel grid current. If there are unionised neutrals in the plume they may interact with the ions through a process known as a charge exchange collision (CEX). These CEX collisions produce low energy ions that may be attracted to and impact the accel grid downstream of the thruster and in the inter-grid region, thereby constituting another contribution to the accel grid current. The total ion current that is accelerated and makes its way out of the thruster unimpeded is then known as the ion beam current. In a well operating thruster, the screen grid current will be equal to the ion beam current plus the accel grid current (which is typically a small value). The neutraliser injects electrons into the ion beam to prevent the spacecraft from developing a negative charge. Some other common types of gridded ion thrusters include radio frequency (RF) ion thrusters and microwave electron cyclotron resonance (ECR) ion thrusters. In RF thrusters, the plasma is created and heated through inductive coupling - this type of thruster requires an inductive coil and complex circuitry to supply power to the plasma but typically does not require any magnets. In ECR type thrusters a magnetron is used to generate microwaves which heat the plasma, and magnets are used to produce electron cyclotron resonance which increases the ionisation efficiency.

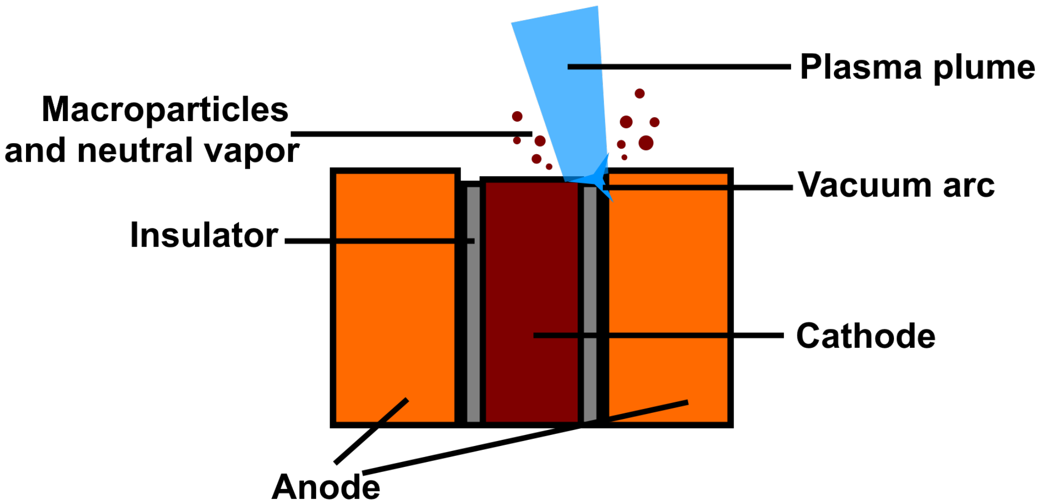

FIGURE 1.2: The vacuum arc thruster. Shown is a cross section of a coaxial design with a cathode rod in the center, surrounded by a tubular insulator and tubular anode. Note the blue plasma plume extending from the arc. In this diagram the arc has anchored to the right hand side of the thruster, it could have anchored to any other side.

1.3 The Vacuum Arc

The vacuum arc, also referred to as a cathodic arc is an electrical discharge in which the current is conducted through plasma produced from the electrodes. The vacuum arc was first investigated in the late 19th century by A. W. Wright for mirror coatings and by T. A. Edison for phonograph molds, Boxman (2001); Waits (2001). The plasma is produced in microscopic ($1 - 10\mu m$) regions on the cathode known as cathode spots, Francombe & Vossen (1994). The conditions are extreme in the cathode spots with current densities on the order of $10^6 - 10^8 A/cm^2$. These intense current densities cause rapid vaporisation of a very small region of the cathode into plasma. The cathode spots also produce neutral metal vapor and liquid metal droplets known as macroparticles, Daalder (1981), because they are much larger than the ions and electrons in the arc. Several macroparticles can be seen on the anode edge in figure 1.3. The ion current in the arc depends on the cathode material but is typically between $5 - 12\%$ of the discharge current. This ion current leaves the cathode at high velocity due to thermal and electromagnetic effects in the cathode spot, Hantzsche (1983). The electron current from cathode to anode is greater than 100% to account for this loss of ions, Anders (2009). The ion velocities are on the order of $4km/s$ for bismuth ($A = 209$) up to $24km/s$ for lithium ($A = 7$) Polk et al. (2008) corresponding to ion energies between 20-200 eV, Francombe & Vossen (1994). The average ion charge state of the ions is typically greater than one, Hashmi (2014), and the arc burning voltage is between 15-25V for most cathode materials Kimblin (1973). Cathode materials of lower cohesive energy typically have lower burning voltages, and lower average ion charge states - an empirical relation known as the cohesive energy rule, Anders et al. (2001). The conditions in the cathode spot are still not completely understood but the cathode spots can best be described by a fractal model as they exhibit significant spatial and temporal self similarity, Anders (2012). This is observed in different spots carrying different currents and at very different time scales appearing to show the same structure. The vacuum arc current and voltage display significant variation and produce large amounts of electromagnetic interference (EMI).

1.3.1 The vacuum arc thruster (VAT)

The vacuum arc thruster (VAT), is a simple form of electric propulsion where the thrust from the high velocity plasma produced in the cathode spots of a vacuum arc is used to move spacecraft, Kolbeck et al. (2016). A cross section of a coaxial VAT design is shown in figure 1.2, it consists simply of an anode and cathode separated by an insulator. The arc occurs across the insulator and anchors to the cathode where a plasma bridge is formed with some plasma connecting across the anode and cathode and completing the circuit. Typically the fraction of plasma that leaves the cathode surface is maximised in an attempt to maximise the thrust produced by the device, Lun (2013a). For this reason a common electrode configuration for VATs is the coaxial design shown in figure 1.2. The unwanted products of the vacuum arc, the neutral metal vapor and macroparticle droplets are also shown in this diagram. Steps are often taken in VAT design to minimise the mass lost to these products. This may include using magnetic fields to steer the cathode spots across the surface, Keidar et al. (2005), or simply using cathode materials of higher cohesive energy. An ignition sequence of a vacuum arc captured by a high speed camera showing the plasma arc and the expansion and cooling of a macroparticle plume is shown in figure 1.4.

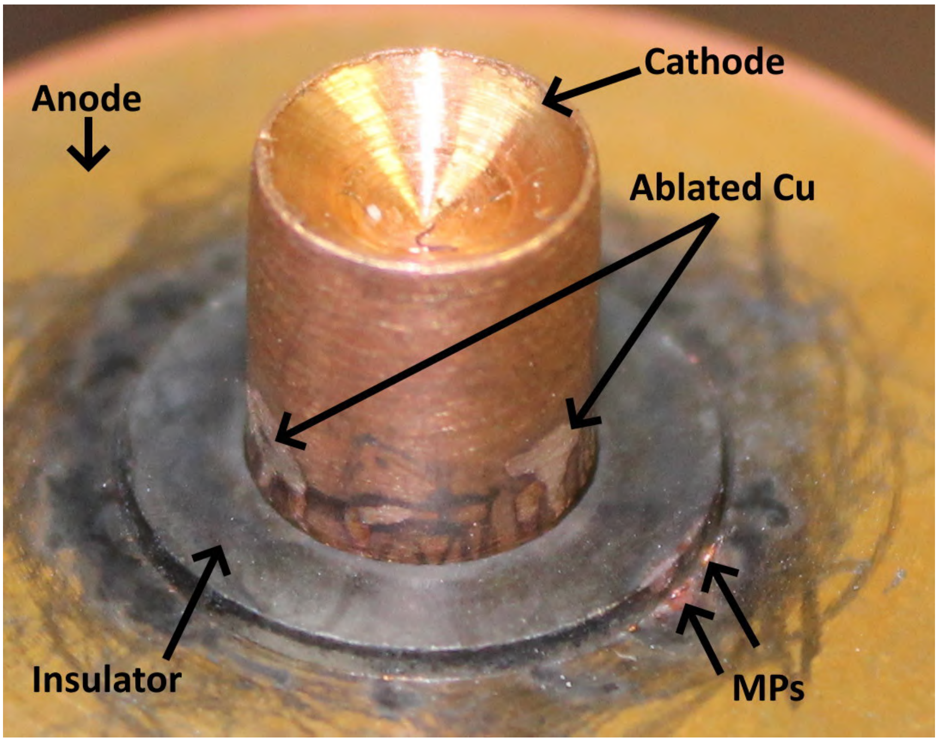

FIGURE 1.3: VAT with raised cathode. Raised center rod is a copper cathode. The grey disk surrounding the cathode is the top surface of the tubular alumina insulator, which has been coated in graphite to aid arc ignition. Surrounding the tubular insulator is the tubular anode which is seen as the large circular plane of copper in this view. Note regions where copper has been ablated away due to arcing on the raised cathode as well as two large macroparticles (labelled MPs) in the bottom right at the anode-insulator boundary.

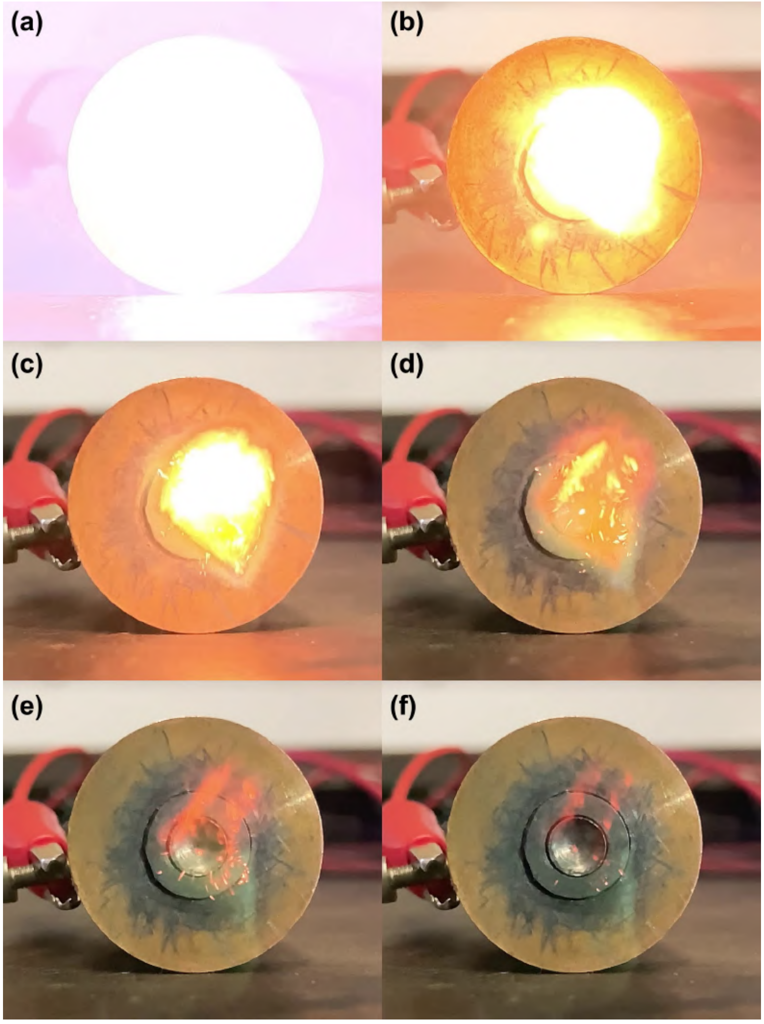

FIGURE 1.4: Arc initiation sequence captured with a high frame rate camera over a period of 20.8ms. Sequence is (a) to (f). Interval between each frame (a-b, b-c etc) is 4.16ms. Due to its speed the plasma (bright pink) is only visible in frame (a). In frame (b) the bight macroparticle plume can be seen to extend far across the cathode and insulator and glows a bright yellow due to its temperature. In frame (c), 4.16ms later, the plume has cooled down significantly and the bright spot is now of reduced size visible in the center of the plume. The outer edge of the plume has cooled to an orange glow. in frame (d), the plume has cooled even more and now emanates a faint red glow with some small regions still yellow-orange. Frames (e) and (f) show this glow dim further to a dark red. This sequence is taken in atmosphere but illustrates the same processes that would occur in vacuum.

1.3.2 VAT triggering

The VAT consists of two electrodes (anode and cathode) separated by an insulator. The voltage between anode and cathode is typically less than 100V and in this work it ranged between 30-60V. These voltages are much lower than that required to trigger a vacuum breakdown and cause an arc between the electrodes which are typically separated by at least 1mm. This is intentional and it allows the pulse to be triggered when desired. Mechanical triggers are the simplest trigger mechanism, where a conductive trigger is placed across the electrodes, thus allowing current to flow, the trigger is then removed and the arc continues to burn. This method is undesirable as it takes a significant time for the trigger piece to be removed and places a mechanical limit on the pulse repetition rate. Alternatively a high voltage pulse of sufficient voltage to cause breakdown (typically several kV) can be provided by a separate circuit to trigger the arc, such a high voltage trigger circuit is employed in the vacuum arc ion source shown in figure 1.7, but requires additional high voltage trigger circuitry.

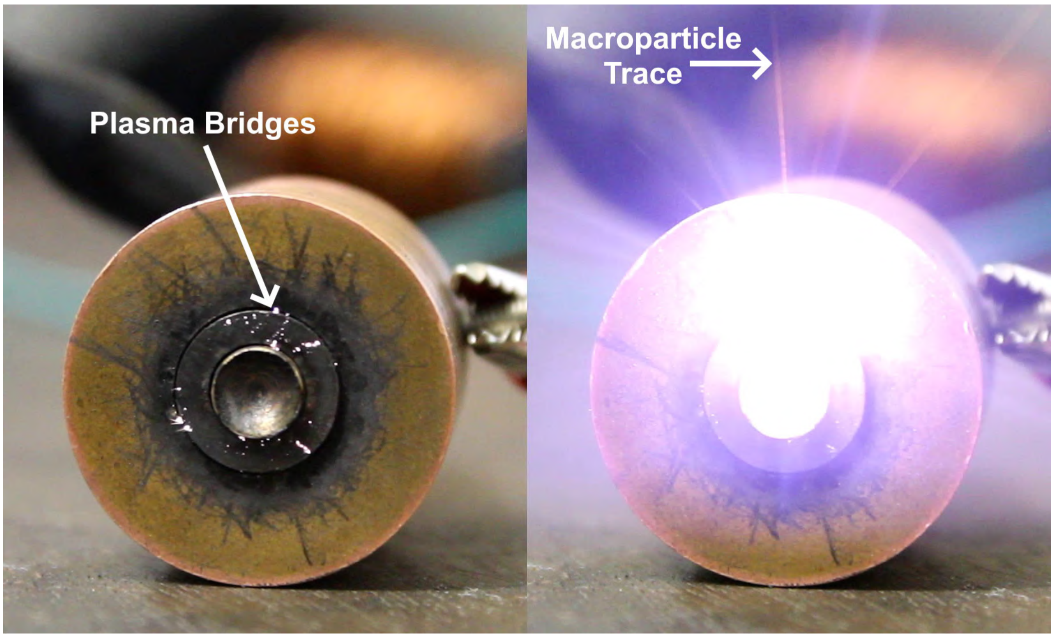

FIGURE 1.5: Left: Tiny plasma bridges from the inductive spike intended to trigger the arc. Right: Full breakdown discharge showing bright plasma arc. Several traces left by glowing macroparticles can also be seen.

’Trigger-less’ triggering of vacuum arcs

If the cathode-insulator-anode surface is coated with a thin conductive layer, such as that applied by drawing across these surfaces with a graphite pencil, then the voltages required to trigger the arc are greatly reduced. Such a vacuum arc thruster with the graphite traces clearly seen is shown in figure 1.5. The graphite layer brings the anode potential much closer to the cathode and the field becomes concentrated at very small regions of the graphite at the interface between the cathode and anode, Anders et al. (2000). A few hundred volts can create enough power deposition in one of these small regions to turn a very small part of this conductive layer directly into plasma, Anders et al. (1998), compared to the several tens of kilovolts typically employed in designs with dedicated high voltage trigger circuits. This voltage can be provided by the electromotive force created by fast turn off of a charged inductor, known as inductive voltage spike or inductive flyback, such as the inductor shown in the circuit diagram in figure 1.6. This type of triggering is known as inductive spike ’trigger-less’ triggering, as it does not require an external trigger circuit, Anders et al. (1998).

Refer to figures 1.5 and 1.6 in the following explanation. The capacitor bank is at a relatively low voltage of 60V (figure 1.6) and is connected in parallel with the VAT anode and cathode. This low voltage itself is insufficient to cause breakdown across the anode to cathode and so no current flows through the thruster. There is an inductor L1 in series with the VAT anode that can be switched to ground through a high power insulated gate bipolar transistor (IGBT) labelled IRG4PH40KD. The thin conductive layer across the anode-insulator-cathode surface was initially applied with a graphite pencil, see the left panel of figure 1.5. To trigger the arc, a square wave signal is sent through a gate driver (which increases the pulse current to switch the transistor quickly), to the gate of the IGBT. This pulse short circuits the inductor to ground, which causes it to charge up and build up a magnetic field, shown by the dotted line labelled charge loop in figure 1.6. After a short charge period (some tens of microseconds), this square pulse signal ends and the IGBT closes. The rapid closing of the IGBT at the end of the pulse causes the rapid collapse of the magnetic field which leads to an inductive spike equal to $V = -L\frac{dI}{dt}$ where L is the inductance of the inductor and $\frac{dI}{dt}$ is the switching speed of the IGBT. This voltage spike is limited to 1200V by an internal diode inside the IGBT, which is more than enough to cause breakdown of a very small part of the thin conductive layer separating anode and cathode. The breakdown of this small layer into a plasma creates a very small amount of plasma across the cathode-anode-insulator surface. Several of these small plasma bridges can be seen tracking across the cathode-insulator-anode surface in the left panel of figure 1.5. This plasma is highly conductive with a resistance of only a few milliohms compared to the kilo ohm resistance of the thin conductive layer before. This low resistance plasma bridge thus allows the full current from the capacitor bank to flow between the cathode and anode - thereby triggering the arc and completing the discharge loop in figure 1.6. This can be seen in figure 1.5, where a trigger plasma bridge of the type shown in the left panel precedes the full arc discharge shown in the right panel. Note that the trigger plasma in the left panel did not fully connect across the anode-cathode surface and so no arc occurred - which allowed this picture to be taken. I.e. the trigger plasma is present without the bright arc plasma that is present in a successful trigger. The right panel is from a pulse just after the left panel where the trigger plasma did bridge across the gap and thus triggered the bright discharge shown in this panel. The thin graphite conductive layer is depleted during triggering but is replenished by a flux of metal ions which replace the graphite and serve the same purpose. Triggering reliability of this type of circuit can be very high and in this work was over 99%. Specific circuit details are discussed in later chapters.

1.3.3 The vacuum arc ion thruster (VAIT)

The metal plasma that streams from the VAT cathode can be accelerated by ion grids to produce a gridded ion thruster known as the vacuum arc ion thruster (VAIT). Using the VAT as a plasma source decouples the ion acceleration from ion creation, enabling much higher performance at the cost of increased complexity, Qi et al. (1998). The vacuum arc ion thruster is known as a vacuum arc ion source when it is used for industrial applications such as heavy ion implantation, and in this case will not include a neutraliser, such a source is shown in figure 1.7 from Brown (2004). In this design the vacuum arc is triggered with an external trigger supply shown next to the cathode. The arc takes place between the cathode and anode, which is placed ahead of the cathode and plasma streams through a hole in this anode towards the grid system. A magnetic coil can be turned on to direct more

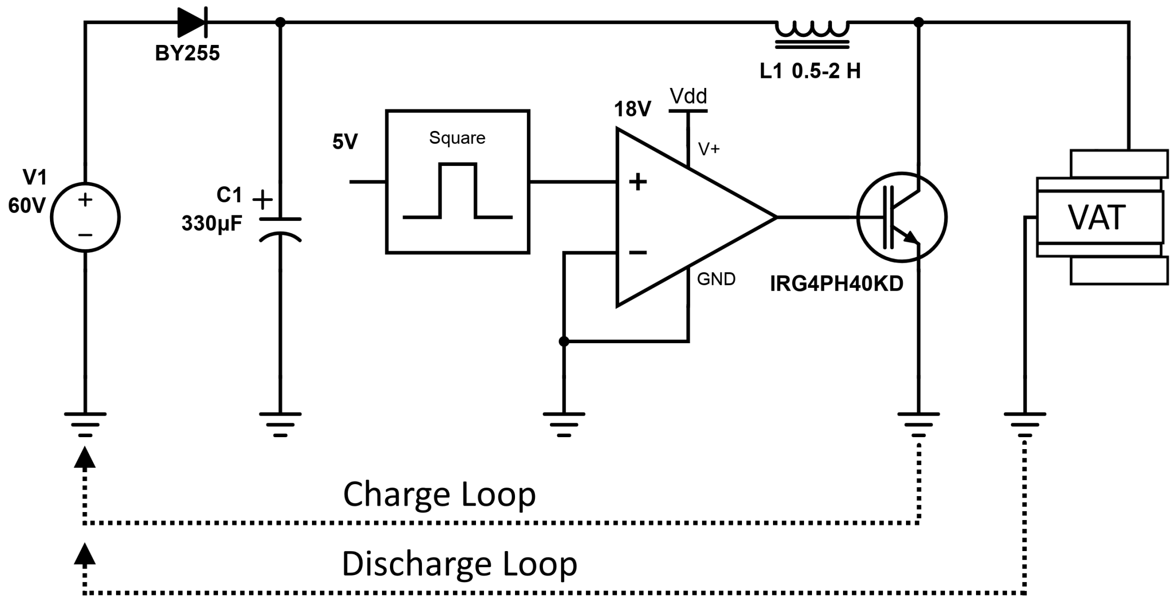

FIGURE 1.6: Pulsed circuit diagram used to initiate and sustain the vacuum arc. A cross section of a coaxial vacuum arc thruster is shown on the right of the diagram with the cathode connection in the middle (where the 'VAT' label is) surrounded by the tubular insulator which is not electrically connected to the circuit, and the tubular anode which is connected as shown.

ions to the grid system. The arc power supply and trigger system are biased to high positive potential by the extractor supply to ensure that the ions are created at high potential. The VAT anode is connected to the screen grid through a resistor - in this way the screen grid will remain close to plasma potential but will be prevented from arcing to the cathode through the highly conductive plasma stream by the resistor. The accel grid is biased negatively by the suppressor supply to prevent electron backstreaming. Finally the last grid is simply biased to ground potential and helps to focus the beam after deceleration.

1.3.4 Disadvantages of traditional ion thrusters and potential of the VAIT

Figure 1.1 showed an electron bombardment gridded ion thruster, which uses the electron gun and magnets to bombard and ionise neutral propellant with electrons. Most state of the art gridded ion thrusters use this technique, typically with xenon

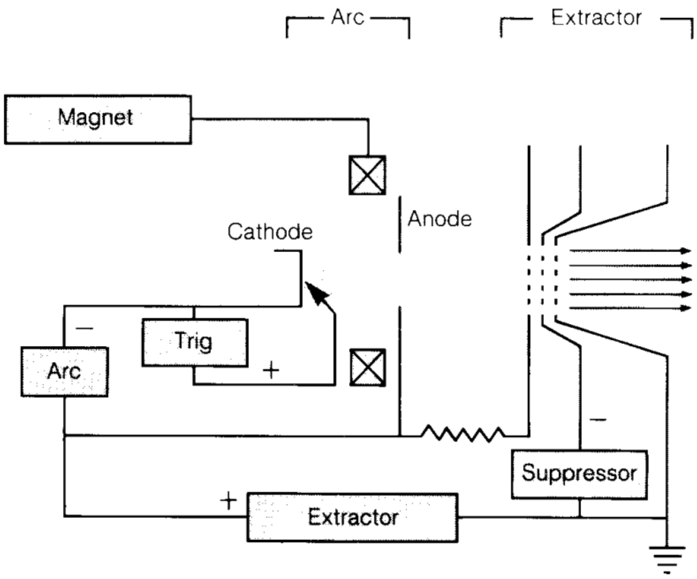

FIGURE 1.7: Electrical schematic of a vacuum arc ion source. This source is designed for industrial applications and so no neutraliser is included. Taken from Brown (2004).

as propellant. Small spacecraft typically cannot use the large discharge chambers and heavy magnets required for this technique and so they typically use a different method such as RF (radio frequency) ionisation which does not require large magnets, but requires an inductive RF coil. Another method of generating the plasma is electron cyclotron resonance (ECR) which requires both magnets and a magnetron to generate microwaves, Foster et al. (2004). The vast majority of ion thrusters (of all types) utilise xenon as the propellant. This is due to xenon's low first ionisation energy ($\approx 12eV$), high atomic mass ($\approx$ 131 amu), storability and chemical inertness. Unfortunately xenon is extremely expensive (approximately 3.5X the price of silver per kilogram), has a number of competing industrial uses and is produced as a bi-product of air liquefaction making it difficult to scale up production, Herman & Unfried (2015). Furthermore xenon is currently subject to geopolitical forces which have introduced significant volatility to its price, Ngoc et al. (2022); DeCarlo et al. (2022).

Recent research has shown iodine to be a promising potential replacement for xenon, Grondein et al. (2016), however it is highly reactive and corrosive, Rafalskyi et al. (2021) and produces multiple ion species. To date, and including the state of the art thrusters in development, all ion thrusters require extensive ionisation equipment such as RF coils, magnets and magnetrons and typically also require tanks, pipes and valves to deliver neutral propellant to be ionised. Therefore the current state of the art ion thrusters still all require: tanks and pipes for pressurised gaseous fuels such as xenon (or complicated heating and sublimation designs for xenon alternatives such as iodine), and some form of ionisation equipment such as ECR magnetrons or RF coils etc. The advantage of the vacuum arc is that it requires neither of these two categories of equipment. As the cathode is the propellant, no pressurised tanks for storage or heaters and sublimation chambers are required - and as the ionisation occurs in the cathode spots of the arc, no additional ionisation equipment is needed either, see figure 1.8.

Another significant advantage of the VAIT is the fact that it is a pulsed system. Traditional ion thrusters run continuously with a duty cycle (ratio of time on to time off) close to 1. This means that the power requirements of the thruster can only be adjusted within a narrow range, typically up to a maximum of $\approx \pm 50\%$ giving a maximum thrust dynamic range of 1:1.5. This means there is a relatively large minimum impulse bit that the thruster can deliver which reduces the potential of these thrusters for applications requiring precise impulse bits such as precision pointing and station-keeping. The thrusters also often need to spend several minutes warming up, before they can be operated. Furthermore, the ionisation efficiency depends strongly on the propellant flow rate which means that it quickly becomes inefficient to try to run the system at lower power levels. The VAIT on the other hand, typically runs in a pulsed configuration with each pulse width on the order of hundreds of microseconds. The VAIT performance is independent of the repetition rate up to a duty cycle of $\approx 10\%$ where cathode heating may become an issue. This means the VAIT can easily have a thrust dynamic range of 1:10000 or more, Qi et al. (1998), with no penalty to performance running at lower power levels.

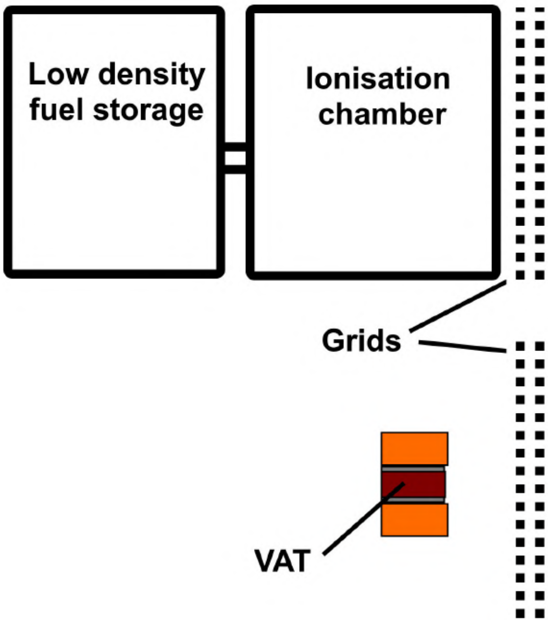

FIGURE 1.8: Diagram showing potential for significant mass, volume and cost savings when switching from a traditional gas based source requiring gas tanks and some type of ionisation chamber to a VAT plasma source.

1.4 In space refuelling

1.4.1 VAIT On-Orbit Servicing

In order to maintain a growing space infrastructure, On-Orbit Servicing (OOS) may be required. OOS involves repair and replenishment of existing space assets to prolong their lifetimes and avoid the costs of a full replacement. One critical aspect of On-Orbit Servicing is the replenishment of fuel reserves that are depleted throughout a satellites operational life, Medina et al. (2017). The vacuum arc ion thruster is an ideal candidate for the next generation of satellites built to be OOS compatible. This is because the VAIT typically uses solid rods of metal as fuel. Replacing solid metal rods appears to be simpler and less complex than performing a pressurised propellant transfer into an aging propellant tank, where the potential for leaks is very high in the vacuum environment. The cost of the metal fuel is also likely to be much less than the cost of a typical noble gas fuel such as xenon or krypton, as discussed earlier.

1.4.2 Refuelling from space resources

All spacecraft propulsion systems used to date have used fuels brought at great expense from the surface of the Earth. Launch costs could be significantly reduced if spacecraft could be put into low earth orbit with minimal fuel and then rendezvous and refuel from a refuelling station already in orbit. The cost of putting one kilogram into low earth orbit varies depending on launch provider and total launch mass. Space exploration technologies corporation offers ride-share launches for a 50kg payload to a standard low earth orbit between $500 - 600km$ for \$325 000 (FY2023 United States Dollars), which is \$6500/kg. If propellant could be gathered from the space environment in an economical manner and delivered to spacecraft in LEO for less than \$6500/kg, then spacecraft could be launched with less fuel - bringing down launch costs and the overall cost of space exploration. One such possible source of propellant in the space environment is from near earth asteroids (NEAs). Yárnoz et al. (2013), recently catalogued twelve easily retrievable objects among the NEA population that could be redirected into a low earth orbit with less than $500m/s$ change in velocity (ΔV). The vacuum arc and vacuum arc ion thruster are ideal candidates for refuelling from space resources as they can be fuelled from any conductive solid, Lun (2013b). Carbonaceous or C-type asteroids contain a high proportion of carbon and metallic or M-type asteroids are almost entirely iron-nickel, Calla et al. (2018); Salter (2016). Therefore to first approximation it appears that refuelling a vacuum arc based propulsion system would be much simpler and require much less processing than attempting to extract chemical fuels or inert gases from these asteroids, Brophy et al. (2012); Sanchez & McInnes (2011); Badescu (2013). Furthermore, several ambitious projects such as the establishment of space based industry could be aided by the mining of these near earth asteroids and a propulsion system that can use simple metals as fuel, Ross (2001); Hein et al. (2020).

The feasibility of using a metallic meteorite as the fuel source for a vacuum arc ion thruster is investigated in this work, see section 4.6.

1.4.3 Space debris

Another potential use case for vacuum arc based propulsion systems is in the clean up of space debris. Space debris is a growing problem that could potentially be solved by using a vacuum arc based propulsion system which could attach to a defunct satellite and use the metal structures of the defunct satellite itself as the reaction mass to safely deorbit the craft, Aslanov & Yudintsev (2013); Haque et al. (2013).

1.5 Basic plasma physics of ion thrusters

Thrust Production in Ion Thrusters

In a simple two grid (diode) system with no ions between the grids the electric field between the grids is simply the potential V divided by the grid separation d. The presence of ions in this region will create some charge density which will change the electric field. From Poisson's equation:

$$\frac{dE(x)}{dx} = \frac{\rho(x)}{\epsilon_0} = \frac{qn_i(x)}{\epsilon_0} \tag{1.7}$$

Where ϵ_0 is the permittivity of free space, $\rho(x)$ is the charge density, $n_i(x)$ is the ion density between the grids and q is the ion charge Goebel & Katz (2008).

The force on an ion in an electric field is $F = Eq$. Thus the total force due to the ions is:

$$F_{ion} = q \int_0^d n_i(x)E(x)dx \tag{1.8}$$

Using (1.7),

$$F_{ion} = q\frac{\epsilon_0}{q} \int_0^d \frac{dE(x)}{dx} E(x)dx = \epsilon_0 \int_0^d E(x)dE(x)$$

thus,

$$F_{ion} = \frac{\epsilon_0}{2} E(x)^2|_0^d = \frac{\epsilon_0}{2}(E_{accel}^2 - E_{screen}^2) \tag{1.9}$$

So the thrust produced by the acceleration of ions is:

$$T = -F_{ion} = -\frac{\epsilon_0}{2}(E_{accel}^2 - E_{screen}^2) \tag{1.10}$$

The ion acceleration force F_{ion} is an electrostatic pressure which transfers the force to the spacecraft via the electric field on the grids. E_{screen} can be thought of as an electrostatic drag and E_{accel} the main thrust. This provides intuition as to how the maximum thrust is achieved when $E_{screen} = 0$, which occurs when the thruster operates at the space charge current limit - which is derived below.

1.5.1 Plasma Sheaths

This section aims to give the reader a brief summary of basic plasma physics relevant to electric propulsion systems and ion thrusters in general. For a comprehensive review of plasma physics see the many books on the subject Francombe & Vossen (1994), Chen et al. (1984). Note that the term electrode is used generically in what follows, and electrode could mean vacuum chamber, probe or ion grid.

ϕ is the plasma potential, i.e., the potential difference between the plasma and electrode, e is the elementary charge, k is the Boltzmann constant and T_e is the plasma electron temperature. The plasma electron temperature represents the average kinetic energy of the electrons in the plasma and is typically equivalent to $\frac{e\phi}{k}$.

Due to their much smaller masses, electrons leave the plasma and are absorbed by boundaries with the plasma (such as an electrode, grid or probe) at much higher rates than ions. This produces a negative potential on the boundary, which in turn attracts ions and repels additional electrons. A region then forms around the boundary where there are only ions and no electrons, this region is the transition region from the bulk of the plasma to the boundary, and it is known as a sheath.

There are three basic cases of sheaths to consider. The case where the potential difference between the plasma and an electrode is very small compared to the plasma electron temperature, $e\phi << kT_e$, the case where the potential difference is very large compared to the electron temperature, $e\phi >> kT_e$, and an intermediate region where $e\phi \approx kT_e$.

1.5.2 $e\phi << kT_e$ and the Debye length

We begin by using Gauss's law to solve for the potential of a stationary charge Q:

$$\oint \mathbf{E} \cdot d\mathbf{s} = \frac{1}{\epsilon_0} \int_V \rho dV = \frac{Q}{\epsilon_0} \tag{1.11}$$

The potential is found by drawing an arbitrary sphere of radius r around the charge such that $\mathbf{E} = \frac{Q}{4\pi\epsilon_0 r^2}\hat{r}$ then, using the fact that $\mathbf{E} = -\nabla\phi$, the solution for the potential is,

$$\phi(r) = \phi_2 - \phi_1 = -\int_{p1}^{p2} \mathbf{E} \cdot d\mathbf{l} = \frac{Q}{4\pi\epsilon_0 r} \tag{1.12}$$

If the charges are mobile however, as they are in a plasma then the charge distribution will react to the test charge. Poisson's equation assuming singly charged ions such that $q = 1$ in 1.7 is,

$$\nabla^2 = \frac{-\rho}{\epsilon_0} = \frac{-e}{\epsilon_0}(n_i - n_e) \tag{1.13}$$

and the electron density is given by the Boltzmann relation,

$$n_e = n_0 \exp\left(\frac{e\phi(r)}{kT_e}\right) \tag{1.14}$$

and it is assumed that $n_i \approx n_0$. Expanding the Poisson equation in spherical coordinates with this electron density gives,

$$\frac{1}{r^2}\frac{\partial}{\partial r}\left(r^2\frac{\partial\phi}{\partial r}\right) = -\frac{e}{\epsilon_0}\left(n_0 - n_0 \exp\left(\frac{e\phi(r)}{kT_e}\right)\right) = \frac{en_0}{\epsilon_0}\left(\exp\left(\frac{e\phi(r)}{kT_e} - 1\right)\right) \tag{1.15}$$

$$= \frac{en_0}{\epsilon_0}\left(\frac{e\phi(r)}{kT_e} + \frac{1}{2}\left(\frac{e\phi(r)}{kT_e}\right)^2\right) \tag{1.16}$$

where a second order Taylor expansion of e^x was used in the last step which is justified as $e\phi << kT_e$. The solution for the potential is now,

$$\phi(r) = \frac{Q}{4\pi\epsilon_0 r} \exp\left(\frac{-r}{\lambda_D}\right) \tag{1.17}$$

Where,

$$\lambda_D = \sqrt{\frac{\varepsilon_0 kT_e}{e^2 n_0}} \tag{1.18}$$

λ_D is the Debye length, ε_0 is the permittivity of free space and n_e is the electron density. The Debye length is the characteristic shielding distance over which the background plasma shields the bare potential of the charged object immersed in it when the potential is small relative to the electron temperature. Consider an expanded copper vacuum arc plasma with a density of $n_e = 10^{17}/m^3$ and an electron temperature of $T_e = 3.5eV = 40615K$ (as determined by Anders et al. (2001)):

$$\lambda_D = \sqrt{\frac{(8.85 \times 10^{-12})(1.38 \times 10^{-23})40615}{10^{17}(1.6 \times 10^{-19})^2}} = 44\mu m \tag{1.19}$$

The sheath thickness for such a plasma will be a few times the Debye length, or on the order of a tenth of a millimeter. Note how in equation 1.12 the potential dropped off as r^{-1}, but now that the plasma is allowed to react to the test charge - it very quickly shields the test charge potential such that it drops off exponentially as $r^{-1} \times \exp(-r/\lambda_d)$, equation 1.17.

1.5.3 $e\phi \approx kT_e$ and the Bohm criterion

For potentials on the order of the electron temperature, $e\phi \approx kT_e$, there is a minimum potential required to maintain a steady state plasma sheath with no discontinuities, known as the Bohm sheath criterion. If we imagine an ion thruster plasma is created at a potential V and that ions fall through an arbitrary potential of ϕ_0 as they move from the plasma center to the sheath edge. From conservation of energy these ions will arrive at the sheath edge with energy,

$$\frac{1}{2}m_i v_0^2 = e\phi_0 \tag{1.20}$$

We denote this potential drop off between the center of the plasma and the sheath edge (not the electrode boundary) the pre-sheath potential. After the sheath edge, these ions will then fall through another potential before they arrive at the boundary:

$$\frac{1}{2}v^2 = \frac{1}{2}m_i v_0^2 - e\phi(x) \tag{1.21}$$

with velocity,

$$v = \sqrt{\frac{2e(\phi_0 - \phi(x))}{m_i}} \tag{1.22}$$

Therefore the ratio of the ion velocity at the sheath edge (after pre sheath acceleration) to the velocity in the sheath is given by:

$$\frac{v_0}{v} = \sqrt{\frac{\phi_0}{\phi_0 - \phi(x)}} \tag{1.23}$$

Since there is only one population of ions we state:

$$n_i v = n_o v_0 \tag{1.24}$$

$$n_i = n_o \frac{v_0}{v} \tag{1.25}$$

$$n_i = n_0 \sqrt{\frac{\phi_0}{\phi_0 - \phi(x)}} \tag{1.26}$$

For $\phi(x) << \phi_0$, valid near the sheath edge the ion density becomes,

$$n_i = n_0 \left(1 + \frac{\phi(x)}{2\phi_0}\right) \tag{1.27}$$

and the Boltzmann electron density becomes,

$$n_e = n_0 \exp\left(\frac{e\phi(x)}{kT_e}\right) = n_0 \left(1 + \frac{e\phi(x)}{kT_e}\right) \tag{1.28}$$

Using Poisson's equation for the potential in one dimension and assuming the ions are singly charged:

$$\frac{d^2\phi(x)}{dx^2} = \frac{-e}{\epsilon_0}(n_i - n_e) = \frac{-e}{\epsilon_0} n_0 \left(\left(1 + \frac{\phi(x)}{2\phi_0}\right) - \left(1 + \frac{e\phi(x)}{kT_e}\right)\right) \tag{1.29}$$

$$\frac{d^2\phi}{dx^2} = \frac{e n_0 \phi(x)}{\epsilon_0} \left(\frac{e}{kT_e} - \frac{1}{2\phi_0}\right) \tag{1.30}$$

For $\phi(x)$ to be a monotonically non-increasing function, which it must be otherwise ions would be slowed or reflected as they enter the sheath edge, the constant bracket must be greater than zero,

$$\frac{e}{kT_e} > \frac{1}{2\phi_0} \tag{1.31}$$

$$\phi_0 > \frac{kT_e}{2e} \tag{1.32}$$

$$v_0 = \sqrt{\frac{2e\phi_0}{m_i}} = \sqrt{\frac{kT_e}{m_i}} \tag{1.33}$$

known as the Bohm velocity, before entering the sheath. For copper vacuum arc plasma, this will be on the order of $2300m/s$. The plasma density at the sheath edge can be calculated,

$$n_e = n_0 \exp\left(\frac{e\phi(x)}{kT_e}\right) = n_0 \exp\left(\frac{-1}{2}\right) = 0.61n_0 \tag{1.34}$$

This value of 0.61 ignores any ionisation that may occur in the pre-sheath region and so it is often adjusted to 0.5 to account for this. Furthermore it may range from $0 - 0.5$ if ion neutral collisions are considered, depending on the pressure, Chabert & Braithwaite (2011).

The current density of ions entering the sheath of the acceleration grids in a gridded ion thruster is then (in the absence of pre-ionisation and collisions):

$$J_i = 0.61n_0 e v_i = 0.61n_0 e\sqrt{\frac{kT_e}{m_i}} \tag{1.35}$$

For the ion thruster developed in this work, the grid area A_g was approximately $30cm^2$, assuming the plasma expands from the cathode spots to reach a density of $n_0 = 10^{17}/m^3$, the total ion current to the grid system for copper vacuum arc plasma could be expected to be,

$$I_i = 0.61n_0 e v_i A_g = 0.61n_0\sqrt{\frac{kT_e}{m_i}}A_g = 0.61 \times 10^{17}\sqrt{\frac{k \times 40615}{63.55amu}}3 \times 10^{-3} = 0.067A \tag{1.36}$$

1.5.4 $e\phi >> kT_e$ and Child Langmuir sheaths

In the case of potential differences between the plasma and the electrode much greater than the electron temperature, when $e\phi >> kT_e$, the electrons will be repelled over the majority of the sheath thickness and their density will go to zero close to the sheath edge. This is the case present at the grid system of an ion thruster. The ion current density,

$$J_i = n_i e v = n_i e \sqrt{\frac{2e(\phi_0 - \phi(x))}{m_i}} \tag{1.37}$$

, writing Poisson's equation again now neglecting the contribution from the electrons,

$$\frac{d^2\phi}{dx^2} = \frac{-en_i}{\epsilon_0} = \frac{-J_i}{\epsilon_0}\sqrt{\frac{m_i}{2e(\phi_0 - \phi(x))}} \tag{1.38}$$

This integral can be solved by multiplying both sides by $\frac{d\phi}{dx}$ and performing integration by substitution on both sides:

$$\frac{d\phi}{dx}\frac{d^2\phi}{dx^2} = \frac{d\phi}{dx}\frac{-J_i}{\epsilon_0}\sqrt{\frac{m_i}{2e(\phi_0 - \phi(x))}} \tag{1.39}$$

$$\int \frac{d\phi}{dx}\frac{d^2\phi}{dx^2}dx = \frac{-J_i}{\epsilon_0}\sqrt{\frac{m_i}{2e}}\int (\phi_0 - \phi)^{-1/2} d\phi \tag{1.40}$$

Choosing, $u = \frac{d\phi}{dx}$ such that $du = \frac{d^2\phi}{dx^2}$ on the left hand side and $k = (\phi_0 - \phi)$ such that $dk = -d\phi$,

$$\int u du = \frac{-J_i}{\epsilon_0}\sqrt{\frac{m_i}{2e}}\int k^{-1/2} dk \tag{1.41}$$

$$\left(\frac{u^2}{2}\right)_0^x = \frac{-J_i}{\epsilon_0}\sqrt{\frac{m_i}{2e}}(2k^{1/2})_0^{\phi} \tag{1.42}$$

Taking $\frac{d\phi}{dx} = 0$ at $x = 0$,

$$\frac{1}{2}\left(\left(\frac{d\phi}{dx}\right)^2 - (0)\right)_0^x = \frac{+2J_i}{\epsilon_0}\sqrt{\frac{m_i(\phi_0 - \phi)}{2e}} \tag{1.43}$$

Taking the square root,

$$\frac{d\phi}{dx} = 2\sqrt{\frac{J_i}{\epsilon_0}}\left(\frac{m_i(\phi_0 - \phi)}{2e}\right)^{1/4} \tag{1.44}$$

$$\int \frac{1}{(\phi_0 - \phi)^{1/4}} d\phi = 2\sqrt{\frac{J_i}{\epsilon_0}}\left(\frac{m_i}{2e}\right)^{1/4} \int dx \tag{1.45}$$

Integrating yields,

$$\frac{4}{3}(\phi_0 - \phi)^{3/4} = 2\sqrt{\frac{J_i}{\epsilon_0}}\left(\frac{m_i}{2e}\right)^{1/4} x_0^d \tag{1.46}$$

Integrating x across a grid gap of distance d, where the potential across the gap is $\phi_0 - \phi = V$:

$$\frac{4}{3}(V)^{3/4} = 2\sqrt{\frac{J_i}{\epsilon_0}}\left(\frac{m_i}{2e}\right)^{1/4} d \tag{1.47}$$

Squaring and solving for J_i:

$$\frac{16}{9}(V)^{3/2} = 4\frac{J_i}{\epsilon_0}\left(\frac{m_i}{2e}\right)^{1/2} d^2 \tag{1.48}$$

$$J_i = \frac{4}{9}\epsilon_0\sqrt{\frac{2e}{m_i}}\frac{V^{3/2}}{d^2} \tag{1.49}$$

We obtain the Child-Langmuir space charge limited current density. For copper vacuum arc plasma, and a grid system with a grid gap of $1mm$ and a voltage of $1500V$ the maximum current density that can be extracted for a planar sheath is:

$$J_i = \frac{4}{9}\epsilon_0\sqrt{\frac{2e}{63.55m_p}}\frac{1500^{3/2}}{(10^{-3})^2} = 395.5A/m^2 \approx 40mA/cm^2 \tag{1.50}$$

Umstattd et al. (2005). In reality, the sheath shape is not planar but is hemispherical, therefore the grid gap d is replaced by l_e which is a good approximation for circular apertures, Goebel & Katz (2008):

$$J_{CL} = \frac{4}{9}\epsilon_0 \sqrt{\frac{2e\langle Z\rangle}{m_i}} \frac{V^{3/2}}{l_e^2} \tag{1.51}$$

For a grid gap of 1mm, and 1mm thick grids which have 1.5mm diameter apertures l_e will become:

$$l_e = \sqrt{(d + t_s)^2 + r_s^2} = \sqrt{(1+1)^2 + 0.75^2} = 2.136mm \tag{1.52}$$

where d is the grid gap as before, t_s is the screen grid thickness and r_s is the radius of the screen grid apertures. The maximum copper ion current density that can be extracted by this grid system is,

$$J_i = \frac{4}{9}\epsilon_0 \sqrt{\frac{2e}{63.55m_p}} \frac{1500^{3/2}}{(2.136 \times 10^{-3})^2} = 86.7A/m^2 \approx 8.67mA/cm^2 \tag{1.53}$$

This example shows the strong dependence of the space charge limited current on the effective grid gap l_e.

$$J_{max} = \frac{4}{9}\epsilon_0 \sqrt{\frac{2e\langle Z\rangle}{m_i}} \frac{V^{3/2}}{l_e^2} \tag{1.54}$$

A key assumption made in deriving this current density was assuming that $\frac{d\phi}{dx} = 0$ in equation 1.43. For a constant l_e this is true only when the ion thruster is operated at the maximum current (the space charge limited current density) such that the electric field goes to zero in the first grid and thus $\frac{d\phi}{dx} = 0$. In reality, this condition is always held and the ion current extracted through the grids is always at the space charge limit. The upstream sheath edge moves and adjusts the value of l_e so that the ion current density in equation 1.51 equals the ion current density to the screen grid. As more ion current enters the screen grid the sheath edge will move further into the screen grid aperture which varies the effective acceleration length l_e such that the space charge limit condition is always satisfied. This movement of the sheath edge further into the screen grid aperture is best visualised with the figure in the perveance section below.

In conclusion, the Child-Langmuir equation places a limit on the maximum current density and thus, maximum thrust density that can be obtained from an ion thruster. Typically, ion thrusters are run at only $50 - 75\%$ of the space charge limit to allow for design margins - meaning the thrust limit is even stricter.

1.5.5 Perveance

For a given grid system and voltage there is an optimal ion current density that will provide the least beam divergence. This is best illustrated in the figure below, which are results from an AXCEL-INP simulation from Brown (2004).

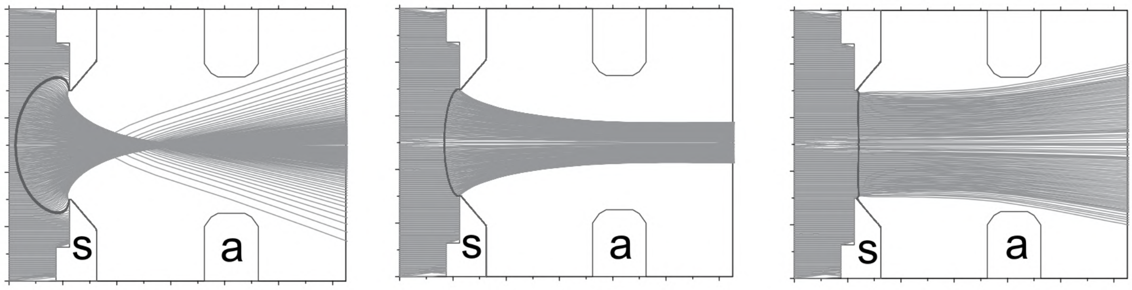

FIGURE 1.9: AXCEL-INP simulation for a given grid set and voltage with three different ion current densities: left to right $j_1 < j_2 < j_3$. (s) indicated screen grid, and (a) indicated accel grid From Brown (2004).

The left condition has the lowest plasma density j_1. This is known as under-perveance, the ion current density is too low for the given grid system and acceleration voltage and so the beam becomes 'over-focused' and takes on a concave shape. This condition can cause ions to cross over each other and directly intercept the accel grid. The rightmost condition with the highest ion current density j_3 is known as over-perveance. In this case the current is too high for the grid system and voltage to handle which leads to improper focusing and a convex beam shape. As the beam widens as it leaves the screen grid aperture it may also cause direct impingement and impact the accel grid. The center condition with the optimal ion current density j_2 is known as optimal perveance. In this case the ion current is well focused by the grid system and the beam has very low divergence - it is said to be perveance matched, Goebel & Katz (2008).

1.6 Thrust corrections: multiply charged ions

In ion thrusters, there is often a small population of doubly charged ions, which reduce the thrust. The reason for this is simple: the thrust is equal to the mass flow rate times the propellant velocity. For each doubly charged ion, the mass flow rate per ion is halved, and due to the ion acceleration, the double charge only grants this ion an extra $\sqrt{2}$ factor of velocity. Thus for each doubly charged ion the thrust is reduced by $\frac{\sqrt{2}}{2}$. Similarly for triply and quadruply charged ions the thrust will be reduced by $\frac{\sqrt{3}}{3}$ and $\frac{1}{2}$ respectively. According to Polk et al. (2008), copper vacuum arc plasma has four detectable ion charge states with relative fractions of: $Cu^{+} = 0.08$, $Cu^{2+} = 0.612$, $Cu^{3+} = 0.291$ and $Cu^{4+} = 0.019$ for an average ion charge state $\langle Z \rangle = 2.253$. Goebel & Katz (2008) derive the doubly charged ion thrust correction factor which can easily be generalised up to quadruply charged ions for copper plasma. The thrust for a given beam current I_b of singly charged ions is:

Singly charged ions ($q = 1$) initially at rest accelerated by a beam voltage of V_b will have a (kinetic) energy $E = eV_b$. Thrust is simply the propellant mass flow rate multiplied by the propellant velocity, for ions this is the product of the ion mass flow rate (which is the ion beam current I_b) and ion velocity: $T = \frac{dm_i}{dt} u_i$. After acceleration the ions have negligible potential energy so we can solve for their velocity with the familiar kinetic energy equation: $\frac{1}{2} m_i u_i^2 = eV_b$ therefore $u_i = \sqrt{\frac{2eV_b}{m_i}}$ and so the thrust for a beam of singly charged ions is simply:

$$T = \sqrt{\frac{2eV_b}{m_i}} I_b \tag{1.55}$$

The modified thrust for a beam consisting of multiply charged ions is:

$$T_m = \sqrt{\frac{2eV_b}{m_i}} I_b \left(Cu^{+} + \frac{Cu^{2+}}{\sqrt{2}} + \frac{Cu^{3+}}{\sqrt{3}} + \frac{Cu^{4+}}{2} \right) \tag{1.56}$$

The thrust correction factor α is the ratio of the modified thrust to the singly charged ion thrust with $I_b = Cu^{+} + Cu^{2+} + Cu^{3+} + Cu^{4+}$:

$$\alpha = \frac{T_M}{T} = \frac{Cu^{+} + \frac{Cu^{2+}}{\sqrt{2}} + \frac{Cu^{3+}}{\sqrt{3}} + \frac{Cu^{4+}}{2}}{Cu^{+} + Cu^{2+} + Cu^{3+} + Cu^{4+}} \tag{1.57}$$

$$\alpha = \frac{1 + \frac{Cu^{2+}}{Cu^{+}\sqrt{2}} + \frac{Cu^{3+}}{Cu^{+}\sqrt{3}} + \frac{Cu^{4+}}{Cu^{+}2}}{1 + \frac{Cu^{2+}}{Cu^{+}} + \frac{Cu^{3+}}{Cu^{+}} + \frac{Cu^{4+}}{Cu^{+}}} \tag{1.58}$$

Putting in the doubly, triply and quadruply ion charge ratios of 7.65, 3.6375 and 0.2375 respectively:

$$\alpha = \frac{1 + \frac{7.65}{\sqrt{2}} + \frac{3.6375}{\sqrt{3}} + \frac{0.2375}{2}}{1 + 7.65 + 3.6375 + 0.2375} = 0.69 \tag{1.59}$$

Therefore, because of the doubly, triply and quadruply charged ions in copper vacuum arc plasma, an ion thruster utilising this plasma will only be 69% as efficient as if all the ions were singly charged.

Beam divergence correction

A typical ion thruster plume can be modelled as cosinusoidal, Goebel & Katz (2008) and this approximation is also true of vacuum arc plasma sources, Keidar et al. (2014). In this case the thrust correction factor is simply the cosine of the beam divergence angle,

$$F_t = \cos\theta \tag{1.60}$$

As the beam divergence could not be measured in this work, and likely could change during the pulse, the beam divergence was assumed to be double that of a state of the art gridded ion thruster of a similar size, the $\mu 10$. $\mu 10$ is a 10cm class ECR type ion thruster used on the Hayabusa missions by the Japan Aerospace Exploration agency (JAXA) and has a beam divergence angle of 12 deg, Tani et al. (2019). Therefore, assuming a beam divergence angle double that of $\mu 10$, gives $F_t = \cos 24 = 0.91$. Therefore the beam divergence reduces performance by 9%.

Combining performance corrections

The combined performance correction factor is then given by,

$$\gamma = \alpha F_t = 0.69 \times 0.91 = 0.63 \tag{1.61}$$

1.7 Vacuum Arc Propulsion Figures of Merit

Polk et al. (2008), extensively derived the theoretical performance of both vacuum arc thrusters and vacuum arc ion thrusters. The equations are presented here for completeness.

The ion fraction value for copper is given as 11.4 % taken from Anders et al. (2005).

1.7.1 Thrust and Specific Impulse: Vacuum Arc Thruster

The total amount of material ablated from the cathode surface is proportional to the discharge current I_d by a material dependent factor E_r, the erosion rate,

$$\frac{dm_t}{dt} = E_r I_d \tag{1.62}$$

which is the total mass lost from the cathode, including losses to neutral vapor and droplets of liquid metal known as macroparticles. The erosion rate can be measured by measuring the arc current and the total mass loss.

The erosion rate is a cathode material property and is given as mass per coulomb of arc charge. Brown & Shiraishi (1990) give a relation for the erosion rate not considering mass lost to neutral vapor and macroparticles,

$$E_r = \frac{f_i m_a A}{e\langle Z\rangle} = 10.4\frac{A f_i}{\langle Z\rangle}\mu g/C \tag{1.63}$$

This relation holds well for most metals with the exception of those with low melting points, such as tin, magnesium, bismuth or lead. For these metals neutral vapor and macroparticle production are the dominant mass loss mechanisms.

The ion fraction is the ratio of total ion current that exits the thruster to the total discharge current:

$$f_i = \frac{I_i}{I_d} \tag{1.64}$$

where I_i is the total ion current.

The ion mass flow rate is simply the total ion current times the ion mass m_i, where the total ion current is equal to the arc current multiplied by the ion fraction f_i, and the average ion charge which can be expressed as the elementary charge e multiplied by the average ion charge state $\langle Z \rangle$,

$$\frac{dm_i}{dt} = \frac{m_i f_i I_d}{e \langle Z \rangle} \tag{1.65}$$

as there is no secondary ion acceleration mechanism, the thrust of a vacuum arc thruster is simply the ion mass flow rate times the ion velocity plus any contribution from neutral vapor and macroparticles:

$$T_{VAT} = \frac{dm_i}{dt} u_i C_t + T_{neut,macro} \approx \frac{dm_i}{dt} u_i C_t = \frac{m_i f_i I_d u_i C_t}{e \langle Z \rangle} \tag{1.66}$$

where the correction factor C_t takes into account the fact that the VAT plasma plume does not all stream directly away from the VAT. The cosinusoidal plasma distribution leads to typical values for C_t of 0.67.
During proper operation, neutral vapor erosion should be minimal and thrust from macroparticles has been shown to be negligible Kolbeck et al. (2016), therefore equation 1.66 is an accurate description.

Specific Impulse (I_{sp}) is the total impulse delivered per unit of fuel spent. In general the specific impulse can be expressed as the ratio of the effective exhaust velocity v_{eff}, which is lower than the ion velocity as this value accounts for losses, to the gravitational acceleration g. This is equal to the thrust T divided by the total mass flow rate $\frac{dm_t}{dt}$ times g, the gravitational acceleration. For a vacuum arc thruster:

$$I_{sp,VAT} = \frac{v_{eff}}{g} = \frac{T}{\frac{dm_t}{dt} g} = \frac{m_i f_i u_i C_t}{e \langle Z \rangle E_r g} \tag{1.67}$$

The thrust of a VAT is proportional to the ion mass m_i , ion current fraction f_i, total discharge current I_d and ion velocity u_i. It is inversely proportional to the charge state distribution factor $\langle Z \rangle$ because higher charge states represent more energy lost into multiply ionizing the ions (Polk et al. (2001); Kolbeck et al. (2016)). Note that in the specific impulse calculation, the total mass flow rate $\frac{dm_t}{dt}$ must be used, as this accounts for neutral vapor and macroparticle mass losses, that do not contribute to the thrust. We can now discuss ion thruster performance.

1.7.2 Vacuum Arc Ion Thruster

In a VAIT, the beam current is the total ion current from the VAT that can be extracted by the grid system. The effective grid transparency is given by ϕ_g. In the VAT we used the thrust correction factor of $C_t = 0.67$ to represent the fact that a significant fraction of the VAT plasma moves at angles away from the VAT surface normal. In the VAIT, the situation is more complex as we must now consider what fraction of the total ion flux from the cathode arrives at the grid system. This is corrected with the ion current correction factor C_j. C_j depends on two factors: the grid radius r_g, and the cathode to grid spacing L. The plasma density from the VAT is well described by a cosinusoidal plume distribution, Kolbeck et al. (2016). In this case C_j is given by, Polk et al. (2008),

$$C_j = \frac{1}{1 + (\frac{L}{r_g})^2} \tag{1.68}$$

For L equal to r_g, $C_j = 0.5$, and it is clear that larger grid radii compared to the cathode to grid distance will allow more of the VAT plasma to be captured and used to produce thrust. A ratio of $\frac{L}{r_g} = 0.5$ is realistic to obtain in a well designed thruster and will give a high value of $C_j = 0.8$.

The cathode cannot be placed arbitrarily close to the grids as this will exceed the peak ion current extraction limit of the grids. The peak ion current density at the screen grid for a circular grid is simply,

$$j_{peak} = \frac{f_i I_d C_j}{\pi r_g^2} = \frac{f_i I_d}{\pi (r_g^2 + L^2)} \tag{1.69}$$

The ion beam current is the total ion current from the VAT that is accepted and accelerated through the grid system,

$$I_b = f_i I_d C_j \phi_g \tag{1.70}$$

where ϕ_g is the effective grid transparency. The sheath that forms around the grid apertures is hemispherical as described above, this effect increases the effective grid transparency over the optical transparency. Note that in the following equations the average ion charge state $\langle Z \rangle$ is used rather than the multiply charged ion ratio correction α, a close approximation. Note that $1/\sqrt{\langle Z \rangle} \approx \alpha$.

The velocity the ions will gain from acceleration through the grids is calculated from conservation of energy,

$$\frac{1}{2}m_i u_i^2 = eV_b\langle Z\rangle \tag{1.71}$$

And the ion velocity is this velocity (from the grid system) plus the initial velocity which is insignificant in most ion thrusters but not in vacuum arc ion thrusters,

$$u_i = \sqrt{u_{VAT}^2 + \frac{2e\langle Z\rangle V_b}{m_i}} \tag{1.72}$$

Here u_{VAT} denotes the average velocity the plasma ions gain from the VAT itself, before entering the grid system. For copper vacuum arc plasma $u_{VAT} = 12800m/s$, Polk et al. (2008). This initial velocity can increase performance by a few percent depending on beam voltage and cathode material.

Writing the ion beam mass flow rate, which is the product of the ion mass flow rate and the correction factors,

$$\frac{dm_{ib}}{dt} = \frac{dm_i}{dt}\phi_g C_j = \frac{f_i I_d C_j \phi_g m_i}{e\langle Z\rangle} \tag{1.73}$$

The thrust neglecting the initial ion velocity from the VAT is,

$$T_{approx} = \frac{dm_{ib}}{dt}u_i \approx f_i I_d C_j \phi_g \sqrt{\frac{2m_i V_b}{e\langle Z\rangle}} \tag{1.74}$$

And the actual thrust is,

$$T_{VAIT} = \frac{dm_{ib}}{dt}u_i = \frac{f_i I_d C_j \phi_g m_i}{e\langle Z\rangle}\sqrt{u_{VAT}^2 + \frac{2e\langle Z\rangle V_b}{m_i}} \tag{1.75}$$

and the specific impulse:

$$I_{sp} = \frac{f_i C_j \phi_g m_i}{E_r g e\langle Z\rangle}\sqrt{u_{VAT}^2 + \frac{2e\langle Z\rangle V_b}{m_i}} \approx \frac{f_i C_j \phi_g}{E_r g}\sqrt{\frac{2m_i V_b}{e\langle Z\rangle}} \tag{1.76}$$

Maximum thrust

The maximum thrust is limited by the Child-Langmuir space charge limit derived above in section 1.5.4. By equating the peak ion current density (equation 1.69) at the screen grid with the space charge limited current density we obtain the maximum discharge current,

$$j_{d,max} = J_{max} = \frac{4}{9}\epsilon_0 \sqrt{\frac{2e\langle Z\rangle}{m_i}} \frac{V^{3/2}}{l_e^2} \frac{\pi r_g^2}{f_i C_j} \tag{1.77}$$

Putting this discharge current into the thrust equation (neglecting u_{VAT}) and adding back the thrust correction factor γ which includes losses from multiply charged ions and beam divergence,

$$T_{max} = \frac{4}{9}\epsilon_0 \sqrt{\frac{2e\langle Z\rangle}{m_i}} \frac{V^{3/2}}{l_e^2} \frac{\pi r_g^2}{f_i C_j} \frac{dm_{ib}}{dt} u_i f_i C_j \phi_g \sqrt{\frac{2m_i V_b}{e\langle Z\rangle}} \gamma \tag{1.78}$$

Taking $V_b = V$, a close approximation yields,

$$T_{max} = \frac{8}{9}\epsilon_0 \left(\frac{V}{l_e}\right)^2 \phi_g \pi r_g^2 \gamma \tag{1.79}$$

The maximum thrust attainable in a gridded ion thruster is independent of the ion mass m_i and depends linearly on the grid transparency, grid area and the thrust correction factor - γ which accounts for the beam divergence and the multiply charged ion losses - and quadratically on the electric field between the grids. This equation uses the area for circular grid apertures (as used in this work) with r_g the circular grid aperture radius.

1.7.3 Electrical efficiency

The electrical efficiency of an ion thruster is simply the ion beam power (which produces thrust) divided by the total power into the system (to create the beam),

$$\eta_e = \frac{P_b}{P_t} = \frac{I_b V_b}{P_t} \tag{1.80}$$

For the vacuum arc thruster, using equation 1.71, the effective beam voltage can be calculated to be,

$$V_{b\ VAT} = \frac{m_i u_{VAT}^2}{2e} \tag{1.81}$$

which is simply the VAT ion energy in eV.

1.8 Research Questions

1.8.1 The VAIT for small satellites

Qi et al. (1998), modified an existing high power vacuum arc ion source, (Mevva, an upgraded version described by Nikolaev et al. (2012a)), into a vacuum arc ion thruster (without neutraliser). Qi et al. successfully produced 3keV bismuth ion beams with beam current up to 3A, for a peak beam power just under 10kW. Kolbeck & Keidar (2019) attempted a low power vacuum arc ion thruster but unfortunately were unsuccessful due to power supply limitations and grid arcing. A review of vacuum arc ion source technology was given by Brown (1994). The majority of the limited vacuum arc ion thruster work that has been published to date has all focused on high peak power, large and heavy systems that have been modified from industrial applications. This work seeks to explore the VAIT for small satellites. Therefore the VAIT is to be operated at much lower beam powers and acceleration voltages and the ion thruster design is intended to be compact and take up less than two liters of volume - making it a suitable candidate for mass and volume constrained small satellites.

Neutraliser clarification

In space, a neutraliser is necessary for operation to prevent the spacecraft from developing a negative charge which would then stall the ion beam. However in laboratory and industrial settings a neutraliser is not strictly necessary. Therefore this dissertation will not include a neutraliser, due to time and complexity constraints, and also because it is reasonable that the VAIT could make use of a number of existing electron sources for neutralisation such as a thermionic cathode Rafalskyi et al. (2021). Therefore this work aims to build and test a compact and low power vacuum arc ion source suitable for small spacecraft and to compare the VAIT to the vacuum arc thruster and modern gridded thrusters.

1.8.2 The VAIT for in space refuelling

As mentioned in section 1.4, OOS and in space refuelling are becoming increasingly important as humanity continues to explore space. The VAIT is unique in this area in that it could potentially utilise metals already in the space environment as fuel for propulsion, such as those found on metallic near earth asteroids. A potential advantage of using metal fuels for a VAIT, compared to extracting gaseous or chemical fuels for other types of propulsion systems - is that the VAIT could use the metallic asteroid material with little to no processing. This work aims to investigate this possibility using a metallic meteorite.

1.8.3 Primary objectives:

1. A: Design, develop and test a miniature low-power vacuum arc ion thruster (VAIT) with a suitable VAT as the plasma source.

2. B: Demonstrate ion thruster operation using cheaper and denser metal fuels.

1.8.4 Secondary objectives:

1. A: Compare the performance of the VAIT to the VAT and critically evaluate its value.

2. B: Compare the VAIT with existing gridded ion thrusters.

3. C: Evaluate the feasibility of using metallic asteroids as fuel for the thruster.

Chapter 2

Measurement Equipment

2.1 Aim of this work

The present investigation involved a systematic and iterative development of various VAT plasma sources, ion thruster plasma containment vessels, and grid systems to identify an optimal working configuration. In this chapter, a comprehensive discussion is provided regarding the measuring equipment employed to conduct electrical voltage and current measurements, ion current measurements using multiple ion collectors, vacuum facilities, and other pertinent equipment. The subsequent chapter on design delves into the VATs, grid systems, and ion thruster plasma containment vessels.

This equipment was developed for the evaluation of four crucial ion thruster parameters, namely the VAT arc current, the screen grid current, the accel grid current, and the ion current to a collector plate. The majority of the work conducted in this thesis was spent developing the vacuum arc ion thruster from scratch, with the measurement of the aforementioned four parameters forming a substantial part of the work. To enhance the readers' comprehension of the methods section, a brief overview of the four parameters is provided: the VAT arc current ultimately determines the ion current presented to the grid system, the screen grid current represents the total ion current accelerated by the grids, the accel grid current corresponds to the fraction of accelerated ions that impact the accel grid and result in losses, while the plate current represents the total ion current from the VAT or VAIT that traverses downstream to impact the plate, essentially serving as a measure of the useful thrust-producing ion beam current.

2.2 Electrical Measurements

2.2.1 Remote Circuit Triggering and camera

The square wave signal shown in figure 1.6 that triggered the VAT pulse was provided by an Arduino Nano microcontroller board. This board was in communication with a Raspberry Pi 3 model B single board computer (SBC). The Raspberry Pi had an HD camera module connected to its camera port. The camera was set to record at 1280x720 (HD) resolution at 30 frames per second (fps). Despite the VAT pulse length being much shorter than the frame time of the camera (hundreds of microseconds vs tens of milliseconds), the code was adjusted so that the first camera frame always coincided with the VAT pulse. In this way, the first pulse of any run could be reliably captured by the camera, even though its frame rate was much below that required to image such short pulses. The VAT pulse and camera capture were controlled by a python script that ran on the Raspberry Pi. This python script was triggered to run through a laptop outside the testing area through a remote desktop connection. This ensured that the high voltage capacitor bank was only charged when the laboratory was empty and so the entire testing procedure met the School of Physics safety standards. The camera setup also provided many of the pictures seen later in this work and was an invaluable resource for diagnosis particularly when solving the arcing problems.

2.2.2 Voltage Measurements

During testing the Picoscope 5444D was used. This is a standard 4 channel oscilloscope with remote triggering and data capture. One high voltage probe (Fluke 80K-40) was used for some limited diagnosis but was not used for testing as its response time was too slow. By setting the Picoscope software to autosave testing could be run remotely with the data automatically captured and the author outside of the laboratory - which was necessary to comply with the school's safety regulations. Running all four channels during testing required approximately 1.5s between pulses which ultimately did place a limit on the speed at which pulses could be run. However, as many other issues discussed later on limited the number of pulses that could be reliably run on the thruster - this data capture speed limit did not significantly hold back testing.

As mentioned, there were four signals measured in this work: the VAT arc current, the screen grid current, the accel grid current and the ion collector current. Due to the VAT circuit floated to high voltage, the VAT arc current and screen grid current were both measured using custom built transducers described below. The accel grid current and ion collector current were measured simply by connecting a standard oscilloscope probe across a measurement resistor that was connected between the bias/accel power supply (which in turn connected to the collector or accel grid) and ground. In this way when ions hit the collector/accel grid, a current is drawn from ground through the resistor to neutralise the positive charge of the ions. The collector/accel grid thus draws a current from the plasma and this current causes the voltage drop across the resistor which is the measured voltage signal. A detailed schematic showing the ion thruster testing setup and the points at which all four signals were measured can be seen in figure 3.9 at the end of the next chapter.

2.2.3 Note on VAT arc voltage

During ion thruster testing, only four signals could be simultaneously captured by the four channel oscilloscope. Therefore the VAT arc voltage was not measured. Only the VAT arc current was measured which gives a direct estimation of the plasma density and is the key VAT metric. The other three oscilloscope channels were dedicated to measuring the screen grid current, accel grid current and plate or beam current.

2.2.4 Current Measurements

In order to measure the VAT arc current, a low value shunt resistor can be placed in series with the VAT and the voltage drop across this resistor measured. If this resistor is sufficiently low valued (tens of milliohms), then the maximum voltage drop can be limited to less than 1 volt for typical arc current levels (50A), and thus one can measure the arc current accurately without affecting it greatly. This method can work well for VAT arc current measurements with an oscilloscope so long as the VAT is connected to ground so that the oscilloscope ground clip can be connected there as well. The problem arises in the ion thruster configuration, where the VAT circuit is now floated to a very high voltage potential. This means that a normal oscilloscope probe cannot be used, as connecting it over this measurement resistor would short the HV supply to ground. Therefore for the ion thruster experiments a variety of current transducers were used. Current transducers use the principle of induction and measure the change in the induced electromagnetic field to determine the current. They therefore provide a perfectly isolated means of measuring currents in a floated high voltage circuit.

Current Transducers

Initially a commercial current transducer was used to measure both the VAT current and the screen / high voltage capacitor bank current. However, after a grid arc caused a current spike of over 600A - the transducer failed and the decision was made to construct adjustable current transducers in the laboratory. By simply taking a large value toroidal inductor and threading one of the VAT wires through the toroid, and connecting the toroidal inductor ends to a low value resistor, a current measurement could be made. This measurement circuit is a simple resistor inductor (RL) circuit with time constant:

$$\tau = \frac{L}{R} \tag{2.1}$$

The measurement circuit has a non-linear response and so would not work as a general purpose current measurement device. However, because the VAT is a pulsed system and the pulse lengths are generally known before experimentation begins we can use these facts to produce an accurate current measurement as follows: we ensure that a sufficiently large value inductor and low value resistor are used, making the time constant much larger than the VAT pulse length. For time constants much larger than the VAT pulse length, the response of the measurement circuit can be considered to be effectively linear over the time scale of the VAT pulse. Then, by recording the voltage response of the measurement circuit in concert with a direct reading using a low value resistor, the measurement circuit can be calibrated. This calibration value can then be used to determine the VAT arc currents once the circuit is floated to a high voltage. The total relative error on this measurement was calculated to be 8%.

2.2.5 Screen grid current measurement

Initially it was thought that the screen grid current, which is the high voltage capacitor bank current, could be measured simply by its voltage drop with a high voltage probe as it is connected to ground and so this does not require a floating probe. However, the rise time of the screen grid current is on the order of 1-10 μs, requiring a probe with significant accuracy at frequencies above 100kHz. The high voltage probe available (Fluke 80K-40) is too slow and the signal rapidly attenuates above 10kHz. Therefore, a second toroidal inductor measurement circuit similar to the one outlined above was constructed. To calibrate this coil, two standard 100MHz oscilloscope probes were used as an effective differential probe to measure the current directly across a measurement resistor at lower voltages (500V, limited by the oscilloscope probes). The two signals were subtracted to give the voltage drop across the known value screen resistor which then gave the screen grid current. This value was then compared to the voltage response of the measurement circuit to calibrate it. In this way, screen grid current measurements were possible at high voltage requiring only one oscilloscope channel, with the same accuracy as above - a relative error of 8%.

2.2.6 Real time capacitor bank voltage reading

To measure the capacitor bank voltage in real time, a 10:1 voltage divider was built with high value resistors and permanently installed on the HV capacitor bank. This enabled a multi-meter to continuously display the voltage on the bank at all times during testing. This was important as it allowed real time knowledge of the bank voltage to determine when it was safe to re-enter the lab after testing completed.

2.3 Vacuum Chambers and Equipment

The vacuum chamber used in this work is shown in figure 2.1, and used a standard rotary mechanical pump and oil diffusion pump combination. The rotary pump pumps down most of the air in the chamber, taking about thirty minutes to do this. While this is happening the oil diffusion pump heats up to operating temperature. Then once the pressure is a few millitorr inside the chamber, the rotary mechanical pump is switched over from pumping down the chamber and now pumps down the diffusion pump, which is then opened to the chamber itself. Now the diffusion pump can reduce the pressure even further by its oil vent action that is backed up by the mechanical rotary pump. After some 10-15 minutes of this mode of operation, the pressure drops to approximately 5×10^{-8} Torr which is considered high vacuum and is a suitable pressure for testing. The pump system can continue to run continuously in this mode almost indefinitely.

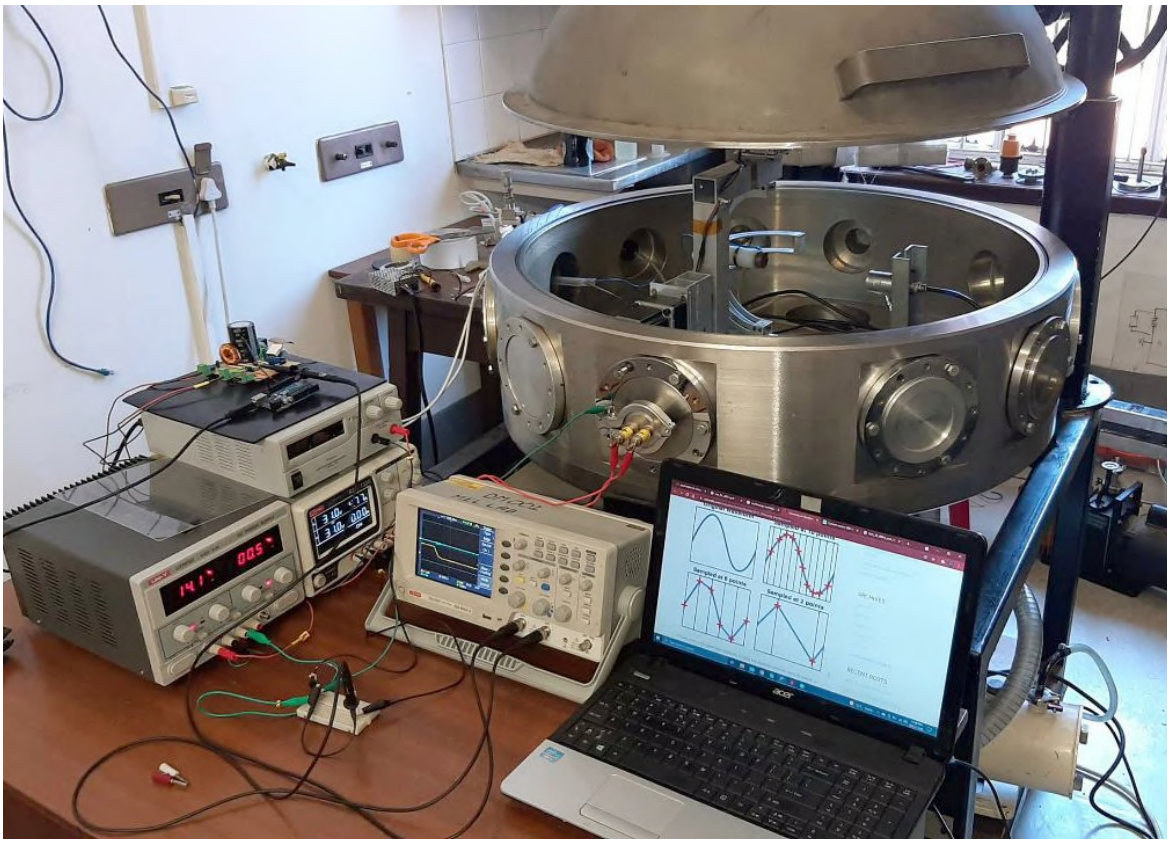

FIGURE 2.1: Some of the testing equipment used in this work. The vacuum chamber can be seen behind the oscilloscope with a mounted VAT and Faraday cup inside. *Photo credit: T. Rencken*

Note on solid metal fuel vacuum considerations

As both the vacuum arc and vacuum arc ion thrusters tested in this work use fuels that are solid at room temperature, the pumping speed of the vacuum pump system does not need to be very high. In conventional gas fed ion thrusters, the pumping speed of the pumps is an important consideration during testing, however in this

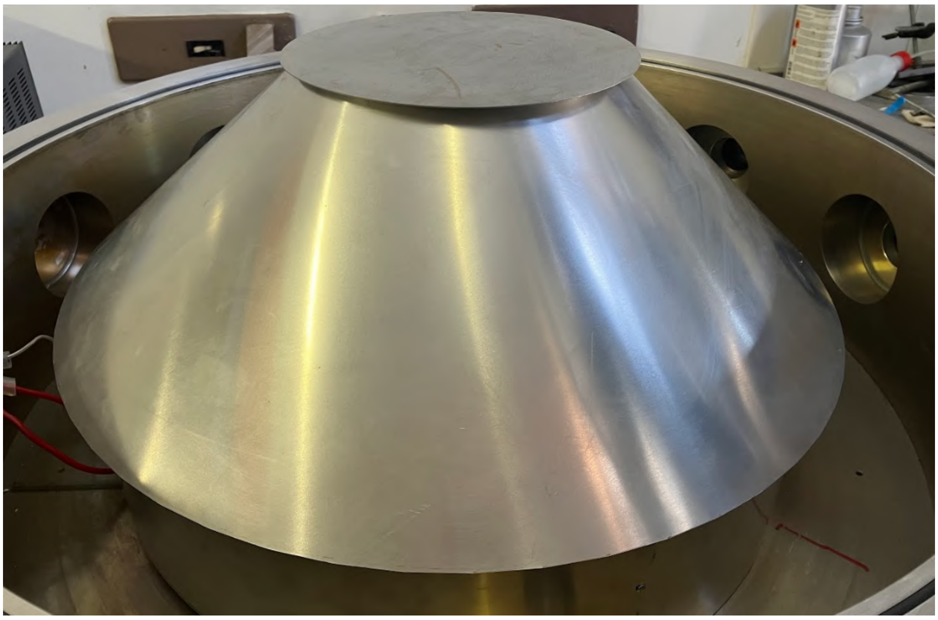

FIGURE 2.2: Total Ion Current Collector

work as only metal plasmas were generated, any neutral metal vapor or plasma present in the chamber rapidly condenses on the chamber walls and thruster components. In a manner reminiscent of a cryogenic pump, where propellant gases condense on a very cold surface, the metal propellant will rapidly condense on the room temperature vacuum chamber walls and in this way the entire chamber and thruster can be considered a pump for the high temperature metal vapor exiting the thruster. While this fact is helpful to the vacuum system, it also means that the chamber, thruster and any components in view of the plasma plume rapidly become coated in a thin metal layer. This caused problems with the grid system where this conductive buildup rapidly led to grid arcing and severely limited the number of pulses that could be run during testing.

2.4 Ion collectors

2.4.1 Total ion current collector for VAT measurements

To perform total ion current measurements, a large ion collector that completely encapsulated the vacuum arc thrusters was used. This large ion collector shown in figure 2.2 was built in a previous work Lun (2013a). A base plate was added to the collector to ensure that any ions directed 180 degrees from the front of the thruster could be captured. As shown in figure 2.3, the ion collector was connected to the negative side of a power supply, the power supply positive was then connected through a 0.3 Ohm resistor to ground. The power supply ensured there was a constant -60V potential on the collector relative to ground. The cathode of the VAT circuit was grounded to ensure that the collector was sufficiently negative relative to the plasma. This was done so that any plasma electrons in the VAT arc plasma would be reflected away by the negative potential. The resistor was sufficiently low valued such that even with an ion current of several amps the voltage drop would be limited to 1 volt and thus the plate negative voltage would remain sufficient to repel electrons during the pulse. As ions hit the collector they deposit their positive charge or alternatively collect negative charge from the collector. As this happens the power supply draws a current of electrons from ground through the resistor to neutralise the positive charge on the plate. In this way the collector draws a net current from the plasma through the measurement resistor which is equal to the ion current.

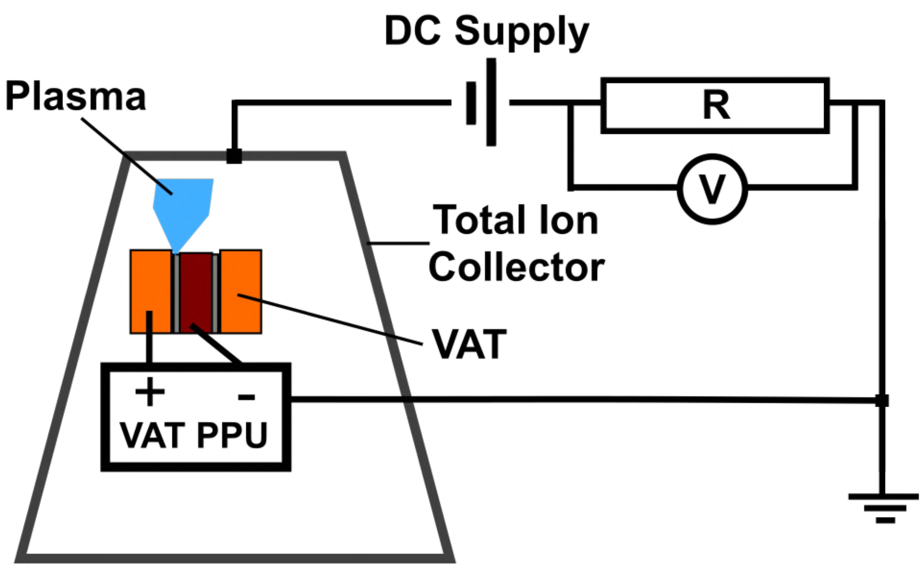

FIGURE 2.3: The total ion collector (dark grey) also shown in figure 2.2 is connected in series through the DC power supply through the measurement resistor R to ground. This ensures a constant negative voltage on the collector to repel electrons. The VAT pulsed power unit (PPU) circuit is connected to the VAT cathode and also to ground, to ensure that the plasma is generated at ground potential. During operation the VAT plasma ions deposit their positive charge on the collector which causes an equal current of electrons to be drawn through the resistor from ground. By measuring the voltage drop V, the ion current from the VAT can be determined.

2.4.2 Ion collector plates

In order to measure the ion beam current from the ion thruster (in contrast to the total ion current measured from the VAT described above), two different methods were considered. Firstly, an indirect method is to measure the screen grid current alone. The screen grid current is an approximation of the beam current, not accounting for losses to the accel grid and any other losses. The screen grid current is the total current drained from the capacitor bank, which during proper operation should be equal to the actual beam current plus the accel grid current. Thus, the screen grid current was measured and used as a baseline of the total ion current accelerated - even if significant fractions of this current did not make it out the thruster. Then, a direct measurement of the beam current was made by using an ion collector plate placed downstream of the thruster. Only the true ion beam current that makes it out of the thruster without impinging on the accel grid and successfully propagates some distance downstream to the plate is measured in this current. Therefore in this work, this ion plate collector current measurement was used as the ion beam current. The screen grid current served as a separate useful measurement of the total ion current separated, but was not used as the beam current.

As no neutraliser was used in this work, the collector plates had to be placed relatively close to the accel grid to prevent the ion beam from stalling in its own space charge and returning to the thruster without hitting the plate.

Plate 1: flat brass plate ion collector

The first plate used was a simple flat brass plate shown in figure 2.4. This plate was initially placed 10 mm from the accel grid.

In gridded ion thrusters, the accel grid is biased negatively to prevent any electrons in the beam from moving 'up-stream' back into the thruster which can cause arcing. This movement of electrons is known as backstreaming, Lafleur & Rafalskyi (2018). A -125V bias was applied to the accel grid, however when operating with the flat brass plate this voltage proved insufficient to stop electron backstreaming arcing. It is possible that the thruster was operating relatively close to space charge limited conditions at certain points in the arc pulse. This could mean that ion space charge in the accel grid holes could significantly raise the grid potential above the

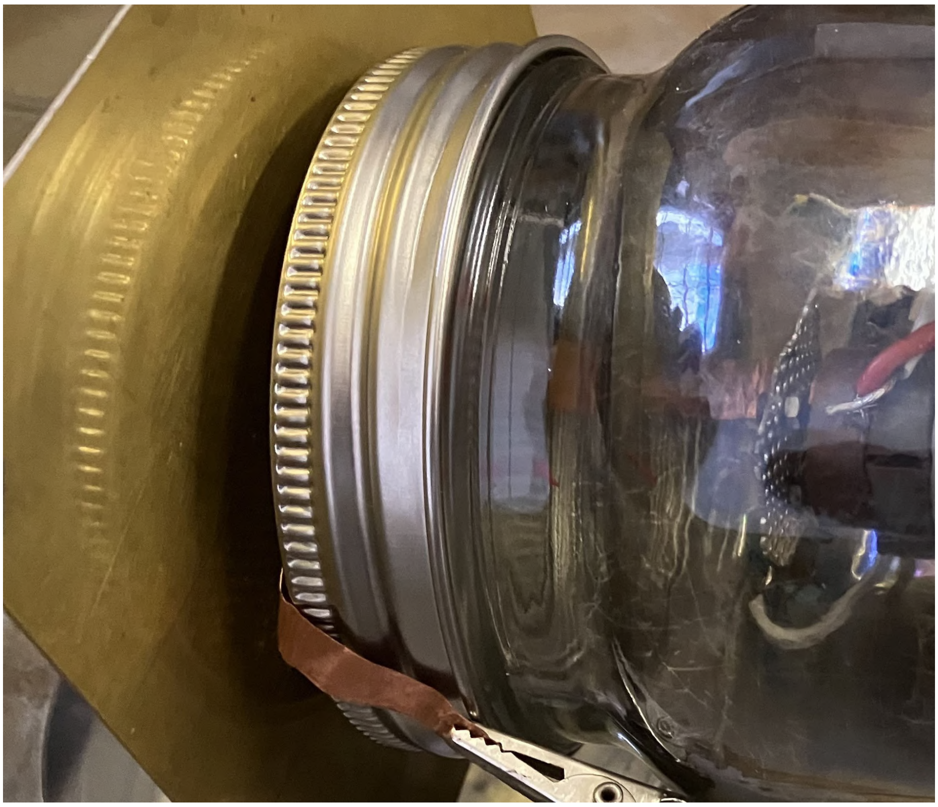

FIGURE 2.4: Flat Brass Plate Ion collector positioned 10mm away from accel grid. The coaxial thruster design with extended anode grid is also visible inside the vessel on the far right. The copper tape at the lower part of the image carries the accel grid connection. The screen grid is connected inside the vessel to the VAT anode.

nominal -125V. In this way electrons may have been able to backstream into the thruster and cause arcing, Goebel & Katz (2008). A second ion collector shown in figure 2.5 that was cylindrical instead of flat and tin-coated solved the arcing issues.

Plate 2: Cylindrical tin plated collector

This can had multiple advantages over the brass plate. Firstly, it could still be placed such that its center line was 10mm away from the center thruster axis - thereby still providing neutralisation to the densest part of the ion beam. However, its cylindrical shape meant that only a small portion of the can was actually as close as 10mm away from the accel grid. Most of the can was further away up to a maximum

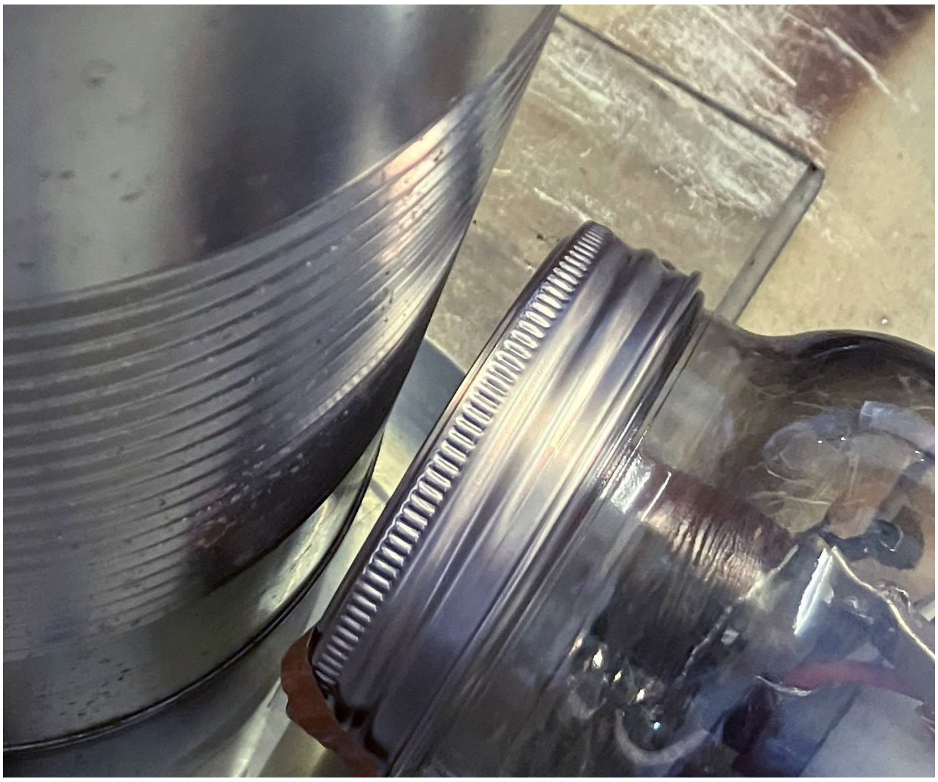

FIGURE 2.5: Tin ion collector. The thruster accel grid is 10mm from the tin. The shape of the tin and the dimpling were expected to reduce secondary electron emission.

distance of 20mm. Thus simply due to its shape, the can could keep most of the secondary electron population further away from the accel grid, thereby reducing the chance of arcing.

Likely due to these reasons, the tin plated can proved a much more effective ion collector reducing the occurrence of this type of grid arc from 50% to below 2%.

2.4.3 Annular coaxial Ion density measurement

In addition to the ion thruster collector plates described above, which made ion thruster beam current measurements, an annular collector plate was produced in order to characterise the ion current density difference between the center and the outside of the plasma beam produced by the VAT plasma source. This was done because it is known that the VAT produces a non-uniform plasma density (Nikolaev et al. (2012b)), which could potentially pose problems for the grid system as the grids are optimised for a narrow range of ion current density. If the plasma density from the VAT is much greater along the axial direction, it may be possible that a narrow region in the center of the grid system becomes overloaded with ion current, while the rest of the grids at higher angles out from the thruster center line may not receive sufficient ion current. In an attempt to quantify this effect, a measuring plate was developed to measure this effect and some basic experiments were performed. The device is shown in figure 2.6. As is shown in the figure, this collector was built into the lid of the glass vessel in order to measure the inner versus outer ion current density at the same location that the screen grid is attached.

FIGURE 2.6: Annular design ion collector for ion current density measurements.

Now that all the measuring equipment has been reviewed, we move on to the design of the VAT and VAIT.

Chapter 3

Design

3.1 Vacuum Arc Thruster Design

3.1.1 Geometry

In a typical VAT, the geometry of the thruster is a critical design factor as it is important that the plasma be directed normally to the thruster axis for maximum thrust. In a VAIT however, it is only important that the plasma streams towards the grids such that a high proportion of the plasma may be captured for acceleration Kolbeck et al. (2016). Two distinct geometries of VAT were tested in this work: a planar thruster which consists of two symmetrical rectangular pieces separated by a rectangular insulator and a coaxial thruster which consists of a cathode rod in the center, surrounded by an annular insulator which itself is surrounded by an annular anode. The coaxial thrusters had cylindrical cathodes 6.25mm in diameter and an alumina ceramic (Al_2O_3) tubular insulator 3mm thick Lun (2013a). The coaxial thruster anodes were copper. The planar thruster had a 1mm flat borosilicate glass insulator separating the anode and cathode which were both mild steel pieces 20mmx5mmx10mm. The planar glass insulator was recessed by 1mm allowing the cathode direct view of the anode. The coaxial thrusters had no recession and the surfaces of the cathode insulator and anode were all in the same plane. A cross section of the geometry is shown in figure 3.1 and the thrusters are shown in figures 3.2 and 3.4. The metallic meteorite sample had previously been mounted in resin for electron microprobe analysis. Therefore the exposed face of the meteorite was simply used as the cathode in a simple planar geometry VAT with an identical 1mm flat borosilicate glass insulator and a 20mmx5mmx10mm mild steel anode (identical to the original planar thruster). This meteorite fueled VAT can be seen in figure

3.3.

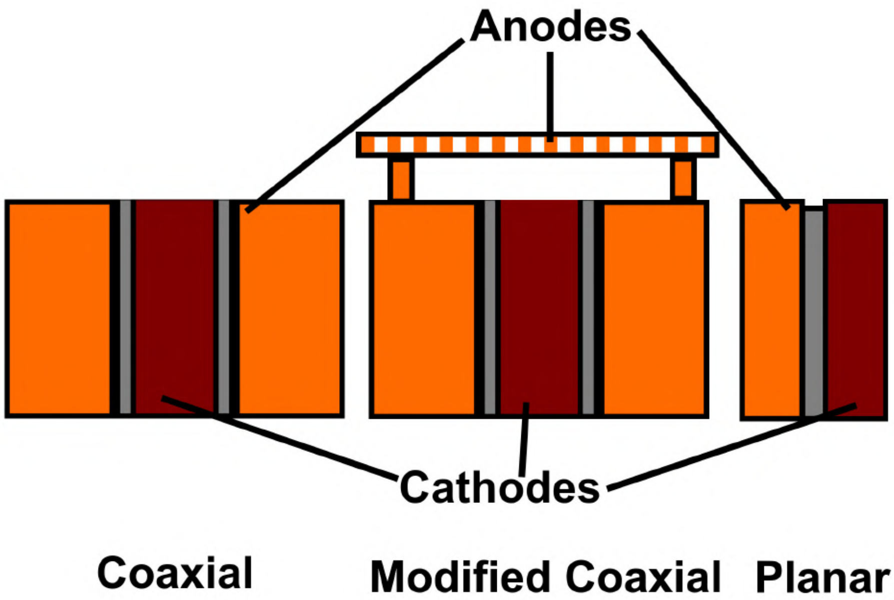

FIGURE 3.1: Cross section of all three VAT geometries used in this work. Left to right: Standard unmodified coaxial thruster, modified coaxial thruster with extended anode grid, planar thruster. Same color indicates the same electrical connection. Anodes are in orange, cathodes in maroon and insulators in grey.

Planar and Coaxial general considerations

The coaxial thruster design is preferred in standard VATs as the cathode has very little line of sight to the anode. This provides the maximum fraction of ion and gas flux normal to the thruster axis, thereby maximising thrust. The planar thruster on the other hand has a significant fraction of the ion flux from the cathode directed straight to the anode. While this reduces the amount of plasma available for extraction, the design offers other advantages. The direct line of sight from anode to cathode can provide a lower resistance arc, potentially allowing stable operation at lower arc currents and voltages. Furthermore due to the increased surface area and anode to cathode line of sight, triggering reliability may be enhanced.

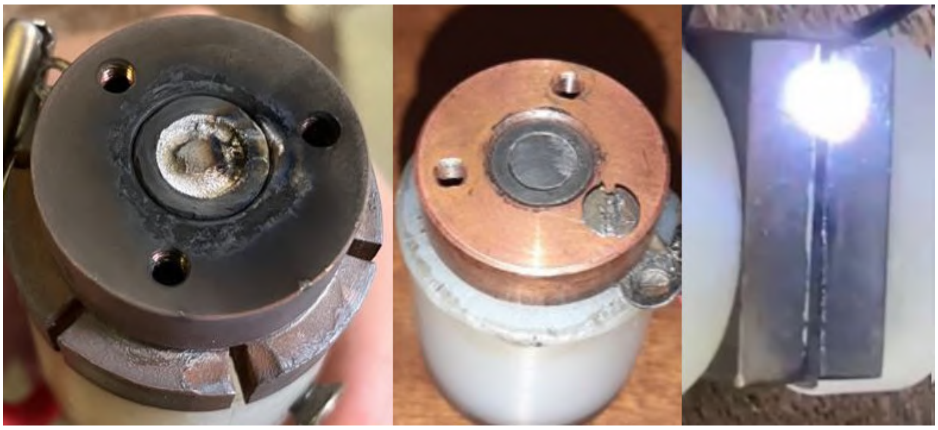

FIGURE 3.2: Left to right: coaxial thruster with bismuth cathode showing erosion, coaxial thruster with steel cathode showing minor erosion, planar steel thruster mid-arc.

Peak Ion Currents; Modified Coaxial Design

To combat the high peak ion currents seen in the standard planar and coaxial designs, a third geometry was developed: the modified coaxial thruster with extended anode. A piece of the grid material (stainless steel, 1.5mm diameter apertures, 1mm thickness, 35% optical transparency) was bolted on to the anode a distance of 5mm away. This extended anode covered the cathode and served two purposes that were advantageous to the ion thruster experiment. Firstly, this extended anode had a transparency of only 35% and so blocked more than half of the ions and neutrals thereby reducing the peak ion current requirements of the grids. Secondly, the extended anode provided a secondary arc attachment point for the vacuum arc in a manner similar to the planar design. This meant that the overall VAT circuit voltage and capacitance could be lowered - thereby providing stability to much lower arc currents, in the range of 30A. In comparison to without the extended anode, the arc currents would have to be increased to approximately 40A or more for stable operation. The modified coaxial VAT is shown in figure 3.4, and the extended anode piece is shown in figure 3.5.

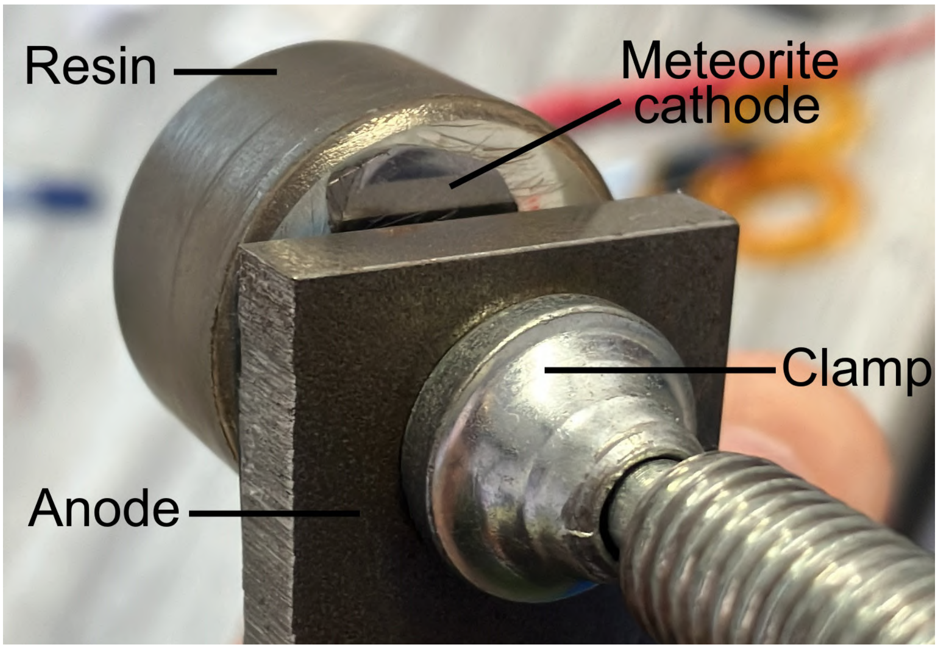

FIGURE 3.3: Meteorite sample as cathode in planar VAT. The glass insulator is hidden behind the anode.

3.2 VAT circuit designs:

3.2.1 Overview of circuit design

The VAT circuit is required to perform two important functions: 1: trigger the arc via a high voltage breakdown across the cathode insulator anode and 2: sustain the arc by supplying the necessary current to maintain it for the desired arc pulse length. As these two requirements are relatively simple, there are a wide range of electrical circuit architectures that can accomplish these two functions. In this work, two different circuit designs were built and tested: 1) a thyristor switched high voltage capacitor bank and 2) a 'triggerless' inductor triggered low voltage circuit. These are briefly reviewed below:

High voltage thyristor switched capacitor circuit:

In this circuit a high voltage capacitor bank was charged up to 850V and then a square wave was sent to a thyristor which triggered the arc. In this design a negative voltage could also be sent to the thyristor to turn off the arc after a given amount of time. The advantages of this circuit architecture are the fact that the arc

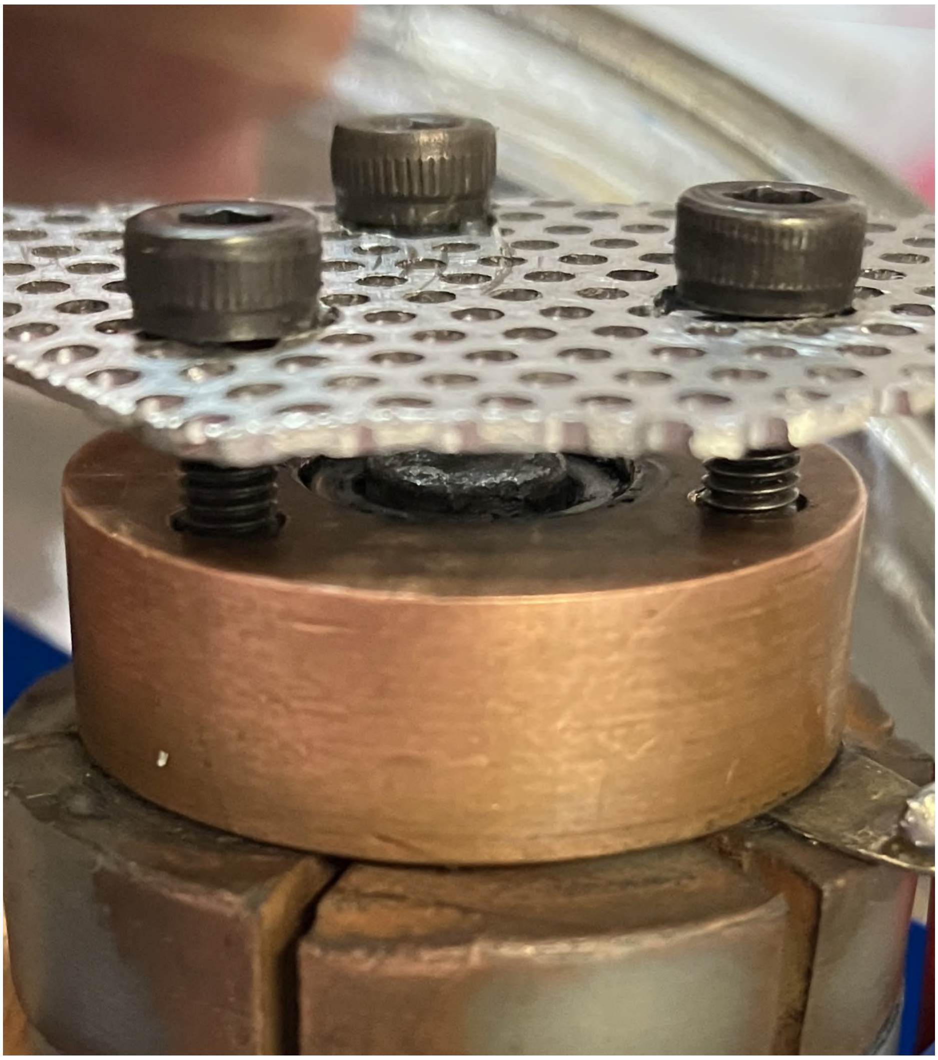

FIGURE 3.4: Modified coaxial VAT design with extended anode. Note the bolts that carry the anode connection to the grid piece which extends 5mm above the cathode surface.

pulse length can be controlled very precisely and if the pulse length is small compared to the time it would take to fully discharge the capacitor: the arc pulse shape will be very square. This circuit performs the required functions of triggering and sustaining the arc at once. The capacitor is charged to a voltage higher than the VAT anode cathode insulator breakdown voltage and so triggering is very reliable, and additionally the same capacitor provides the necessary current to sustain the arc.

The major disadvantage of this circuit architecture is the fact that it requires a dedicated high voltage supply, which was available in the lab but it was a low

FIGURE 3.5: Extended anode piece removed from VAT. Note the metal deposition and signs of arcing. The grid apertures are 1.5mm diameter.

power module which would limit repetition rate. And further this circuit is a considerable safety hazard as the VAT pulse circuitry would now all be high voltage and that would require more complicated operating procedures to operate the circuit safely. For these reasons the circuit architecture that was chosen was the inductive trigger-less circuit design.

Triggerless VAT circuit

The triggerless VAT circuit design Anders et al. (1998) includes a relatively large value inductor. As shown in figure 1.6, a charge pulse is triggered through an IGBT which shorts the inductor to ground, this builds up a current and thus a magnetic field in the inductor. When this pulse abruptly ends, the magnetic field collapses and causes an EMF proportional to the rate of change of the current (how quickly the power transistor switches) and the inductance. This gives a high voltage spike that triggers the arc. There is also a certain amount of energy built up in the inductor and a capacitor is included which together provide the current necessary to sustain the arc. See figure 1.6 and related discussion for more details. The major advantage of this circuit is that the entire circuit voltage can be a modest value of 30-60V. This also makes it much safer to work with than the previous architecture.

The main disadvantage of the circuit is the fact that the the arc pulse length and shape cannot be easily controlled. This is due to the fact that the trigger pulse only controls the charge time of the inductor. The arc burns until the capacitor voltage drops to a level where the arc can no longer be sustained and the arc is extinguished. Another disadvantage of this circuit is also the fact that the inductive spike produces significant EMI and noise which can influence other components. Further, due to the fact that the arc ends when the capacitor voltage drops, there is a period of significant arc instability towards the end of the arc as this chopping current is approached.

A variety of this type of circuit were built in this work with many different combinations of inductors, capacitors, charge times etc.

In general the longer the inductor is allowed to charge, the more energy it will have. If the discharge is purely inductive (no capacitor) then the arc pulse shape is very triangular. However with the right balance of inductors and capacitors the rise time can be delayed and a more flat and approximately more square arc pulse can be attained. By discharging the capacitor through the inductor, the arc current peak is delayed and thus the arc current shape becomes roughly square shaped as opposed to triangular (in a purely inductive or capacitive discharge).

As mentioned previously the ion current produced is directly proportional to the arc current thus to first order, a square arc current pulse will give a roughly square ion current pulse and a triangular arc current pulse will give a triangular ion current pulse.

As the grids are only optimised over a very narrow range of ion current density for a given voltage and grid spacing (Child Langmuir law), a short rise time and flat top which is a square shape are desired.

Of course, this is only to first order, as the arc current produces a plasma which then expands and propagates towards the grids. Depending on the geometry of the thruster and the plasma containment vessel and the distance to the grids the plasma density may have changed somewhat by the time the arc reaches the grids. The final VAT circuit used is shown in figure 3.6.

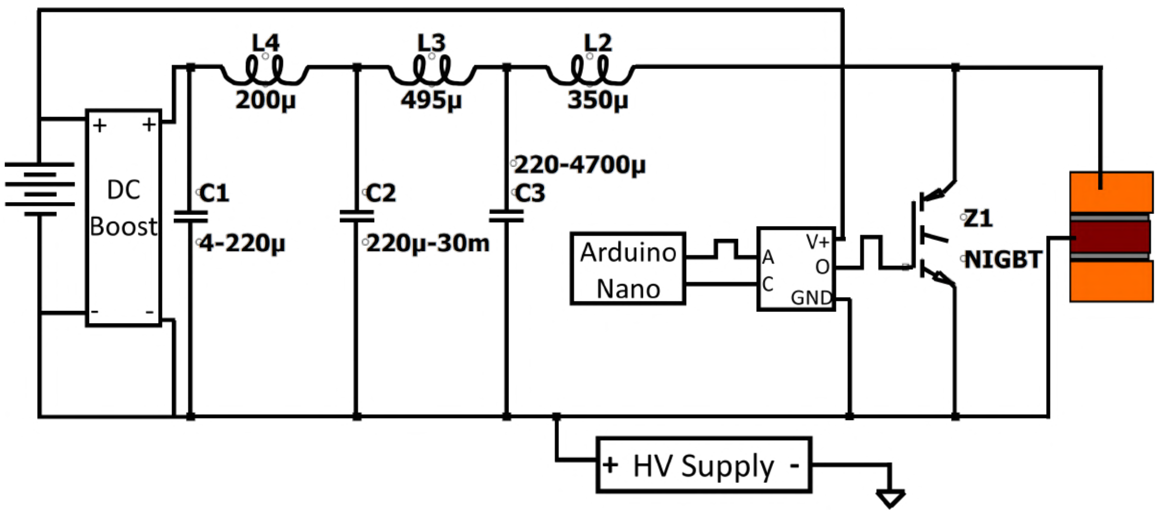

FIGURE 3.6: VAT Circuit Diagram. Standard units apply 200μ is microhenry for an inductor and microfarad for a capacitor.

3.3 Summary of final VAT plasma source

During this work a large variety of VAT designs were tested. Total ion current measurements were taken for both planar and standard coaxial designs and a variety of VAT modifications and circuits were tested in the exploratory phase of this work. For the final ion thruster however, only one VAT design was used. The final VAT source consisted of:

1. A modified coaxial design with extended anode grid piece to reduce peak ion currents.
2. A copper cathode.
3. A 3 stage pulse forming network (PFN) trigger-less circuit design that minimised peak arc currents whilst maintaining arc stability. The circuit had 224 μF of total capacitance and reliably produced 300 μs roughly square shaped arc pulses with peak arc currents between 30-35A.

These points highlight all that is relevant to the ion thruster: that the VAT source provide a suitable plasma for ion acceleration.

3.3.1 Final VAT circuit:

The final VAT circuit used in the ion thruster is shown in figure 3.6. A battery consisting of 6x18650 lithium ion cells powered the circuit with a nominal voltage of 11.1-12.6V. The battery voltage is boosted up to 25-48V by the DC boost converter. The circuit design varied depending on the desired arc pulse length. For the total ion current measurements a single stage PFN design was used with approximately 4.7mF of total capacitance. For the long arc pulses and the final ion thruster tests the 3 stage circuit (as shown) was used. The long arc pulse circuit had approximately 40mF across all three stages. For the ion thruster tests the capacitor values were reduced to the minimum values that would still produce a stable arc with a total capacitance of approximately 224 μF. The python code on the Raspberry Pi SBC sends a signal to one of the Arduino analog inputs, triggering the Arduino to send an 80 μs long charge pulse to the opto-isolated gate driver (TLP 250). The gate driver takes its drive voltage (V+) from the battery. This higher voltage is necessary to switch the power IGBT quickly and trigger the inductive high voltage spike at the end of the pulse that triggers the arc. As the control circuitry is optically isolated from the power circuitry, and the VAT circuit is powered via its own dedicated battery - the VAT circuit can be floated to high voltage such that the plasma it produces is created at a high positive potential relative to ground, which is is necessary for operation of the ion thruster. During total ion current tests, the HV supply would simply be disconnected and the cathode grounded.

3.4 Ion Thruster Design

The ion thruster design must accomplish three primary tasks in order for reliable operation to occur. The first task, generation of a suitable plasma from which a flux of ions will present themselves to the grid system was accomplished by the final VAT plasma source discussed in the previous section. The second task, accelerating these ions into a beam that can produce a meaningful thrust is the objective of this section. As discussed in the introduction, the third task, to provide an equal population of electrons into the ion beam so that it can be neutralised, was not performed in this work. The VAIT is still a very immature technology and so this work seeks to investigate the feasibility of the concept first without any neutraliser. Furthermore, there are a number of existing neutraliser concepts such as thermionic cathodes that could be used for the VAIT, Herniter et al. (1989).

The ion thruster needs to contain the VAT plasma source, and prevent any plasma from leaking out and escaping this enclosure. The ions should not have any other path to escape this enclosure but to be accelerated by the grids, and the electrons must be wholly contained for if any should leak out they could cause grid arcing. For the purpose of plasma containment, borosilicate glass was used throughout this work as it is a very good insulator and has an extremely low outgassing rate making it ideal for operation in high vacuum. Additionally it is optically transparent which was considered an advantage as the plasma flows could be captured on a camera and later analyzed for troubleshooting. This proved useful during the test campaign in diagnosing several of the arcing issues that were encountered. Furthermore, there are a wide variety of laboratory and commercial grade glass vessels and funnels available at very low cost, which was important due to the budget constraints on the project.

Initially, a glass 125mm laboratory funnel was used as the plasma containment vessel before switching to a glass cylindrical vessel. Both of these plasma containment vessels and the grid systems used with them (known as Design 1 and Design 2) had numerous problems and no ion thruster operation was possible with them. Therefore more details of these designs are included in the appendix (A), and the final ion thruster design (Design 3) is summarised below.

3.4.1 Design 3: Final Upgraded cylindrical plasma containment vessel

Design 3 was an improved version of previous designs (which can be found in the appendix) and consisted of a 1 liter volume upgraded cylindrical plasma containment vessel with a threaded screw on lid as seen in figures 3.7 and 3.8. A hole was drilled through the back of the glass vessel to allow for the VAT wires to pass through whilst still maintaining a good seal. The grids were electrical discharge machined (EDM) to be able to fit into the vessel lid and were sealed simply by tightening the lid. The vessel had a circular opening 76±0.5mm in diameter. The grids were identical circles 83±0.5mm in diameter and fitted into the lid which had an 85.5±0.5mm inner diameter. The total grid area available to ions was thus $\pi(3.8cm)^2 = 45.36 \pm 0.38cm^2$, and given the grid transparency of 35% the total optical area available for ion extraction was $0.35 \times 45.36 = 15.88 \pm 0.38cm^2$. The grids were aligned by threading small wires through two apertures on each grid. This worked well to keep the grids aligned but contributed to a conductive layer buildup which lead to grid arcing. The grids (screen grid and accel grid) were held apart by four $0.75 \pm 0.05mm$ thick acetate polymer pieces that had a collective area of $3.8 \pm 0.38cm^2$. Therefore the grid open area was approximately $15.88 - 3.8 = 12.08 \pm 0.38cm^2$.

The maximum ion current density a grid system can accelerate is given by equation 1.54 repeated here:

$$j_{max} = \frac{4}{9}\epsilon_0 \sqrt{\frac{2e\langle Z\rangle}{m_i}} \frac{V^{3/2}}{l_e^2}$$

Design 3 used laser cut stainless steel grids with 1.5mm diameter circular apertures giving an optical transparency of 35%. The grids (accel and screen) were identical and both 1mm thick. Thus Design 3 had a grid gap of $d = 0.75mm$, a screen grid thickness of $t_s = 1mm$ and screen grid aperture radii $r_s = 0.75mm$. Design 3's effective length is thus:

$$l_e = \sqrt{(1 + 0.75)^2 + 0.75^2} = 1.90 \pm 0.15mm \tag{3.1}$$

The maximum ion current density of copper ions produced in a vacuum arc with average charge state $\langle Z\rangle = 2.04$ (Polk et al. (2001)) that Design 3 could extract at 1500V is,

$$j_{CL} = \frac{4}{9}\epsilon_0 \sqrt{\frac{2e \times 2.04}{63.55amu}} \frac{1500^{3/2}}{(1.90 * 10^{-3})^2} = 159.3 \pm 4.5\frac{A}{m^2} = 15.93 \pm 0.45\frac{mA}{cm^2} \tag{3.2}$$

and the maximum ion current that can be extracted is,

$$I_{max} = 15.93 \frac{mA}{cm^2} \times 12.08 cm^2 = 192.48 \pm 11.49 mA \quad (3.3)$$

FIGURE 3.7: Design 3: Final upgraded cylindrical plasma containment vessel with grids attached and lid screwed on.

FIGURE 3.8: Final plasma containment vessel with grids attached without lid showing copper tape connection point for screen grid. Note also the grid alignment wires (white).

3.5 Ion thruster Circuit Design

3.5.1 Two grid design

The two grid system used in this work, and many production ion thrusters consists of one grid at the screen potential known as the screen grid. The screen grid is in direct contact with the plasma. The screen grid potential is slightly lower than that of the plasma potential, due to the plasma sheath that forms around the grid, typically $5 \times T_e$, Brown (2004). The second grid is the accel grid. This grid is biased negative relative to the spacecraft common and neutraliser and during laboratory testing is biased negative relative to ground or vacuum chamber common. This is to ensure that any electrons downstream of the thruster (either from a neutraliser or secondary electrons produced by the ion beam) have no way of moving upstream into the thruster and contacting the high potential of the screen grid/ plasma which would cause arcing.

The circuit must also float the VAT circuit to a high voltage potential known as the screen voltage so that the ions produced in the plasma may flow down this high potential and be accelerated. The ion thruster circuit must consist of at least two power supplies. One power supply is used to bias the VAT circuit and the screen grid to the screen potential relative to ground, and the second supply is used to bias the accel grid negative relative to ground. Both the screen supply and accel supply must be able to provide enough current to maintain the voltage potentials even as beam and accel currents are drawn.

In this work a single high voltage supply capable of a maximum of 6mA current up to 10kV was available to be used. This presented a challenge if a peak beam current of more than 6mA was desired. To work around this limitation, a large high voltage capacitor bank capable of providing much higher peak currents was developed. Initially the capacitor bank design consisted of three ceramic capacitors which provided $1\mu F$ each of capacitance. The capacitor bank size could be computed by determining the total beam charge in a single pulse:

$$Q_{pulse} = t_{pulse} J_D f_i C_c \tag{3.4}$$

Where C_c accounts for the intentional and unintentional losses of the ion current. For instance, a 60A average arc pulse lasting for 500 microseconds with an assumed ion fraction of eight percent would constitute a charge of some 2.4 millicoulombs. The three capacitors at 1 microfarad each at 1500V store approximately 4.5 millicoulombs of charge. Therefore to first approximation one may have assumed that this size of capacitor bank would be sufficient. However while there is enough charge in the bank to accommodate this pulse, the bank would discharge by more than 50% leading to a similar drop in the voltage between the grids. Such a large voltage drop would ruin any stable operation of the thruster and likely cause grid arcing as the lower voltage could not accommodate the same ion current density throughout the pulse. Therefore it was decided that the maximum capacitor bank depth of discharge be limited to 5% to prevent these issues. 12 electrolytic capacitors were wired together to produce a 115 microfarad capacitor bank rated up to 2000V. With this bank, the same arc described above would only discharge the capacitor by 1.4% and so the voltage could be maintained during a pulse. This capacitor bank used a 680$k\Omega$ safety resistor that would bleed the bank empty after approximately $5 \times \tau = 5 \times 0.68 \times 115$ = 391s, or approximately six and a half minutes, while only consuming 2.2mA of leakage current (at 1500V).

3.5.2 Note on safety procedure

The HV power supply was connected to a relay switch which was controlled by the Arduino Nano in communication with the raspberry pi. Through a remote desktop connection, the HV could be switched on and off from outside the lab. Furthermore, at the end of testing the HV supply was turned off remotely and the voltage on the bank monitored until it was below 200V, at which point it was deemed safe to enter the lab.

3.5.3 Limited ion thruster operation with controlled arcing

As shown in figure 3.9, the capacitor bank was charged up by the HV power supply, the bank was connected in series with a resistor to the VAT circuit cathode or anode. This resistor was known as the screen resistor and its value was varied during testing. While the resistor does dissipate power and therefore constitutes an energy loss, it served the purpose of limiting the screen grid current to prevent arcing. This screen resistor enabled a degree of operation even whilst grid arcing issues were prevalent. Specifically, in numerous tests where the plasma properties were not right to operate the thruster without grid arcing the screen resistor enabled a degree of operation as follows: the grid system would be operational for some tens of microseconds before the plasma properties changed and a grid arc was initiated. When this grid arc was initiated, it would cause a short circuit between the grids which would cause a sudden current spike across the screen grid resistor. The screen resistor was sized so that it would allow the screen or beam current to flow (some milliamps) without a large voltage drop. However, as this arc was initiated, the screen resistor voltage drop would be high enough to extinguish the arc, thereby extinguishing it in less than a microsecond. Now with the grid arc extinguished, the voltage would return to operational levels and the thruster could extract more beam current. In this way, partial operation of the thruster was enabled.

3.6 Final Ion thruster design and circuit used

3.6.1 Summary of ion thruster geometry

In conclusion, the final ion thruster design consisted of the modified coaxial VAT with extended anode grid encapsulated in the final plasma containment vessel which had a hole in the back for the VAT anode and cathode wires. The grids used were 1mm thick stainless steel perforated plates with 1.5mm diameter apertures constituting an open area fraction of 35%. The two grid system consisted of a screen grid which was in contact with the plasma and made connection with the VAT anode through a 100 ohm resistor. The accel grid was separated from the screen grid by four $0.75 \pm 0.05mm$ thick acetate insulators. The grid apertures were kept aligned by threading four 1mm diameter insulated wires through aligned apertures on both grids. These insulators and grid alignment wires were both in direct view of the plasma and this is what ultimately limited the operational lifetime of the thruster. This effect is discussed in more detail in section 5.2.

3.6.2 Summary of ion thruster circuitry

As shown in figure 3.9, the ion thruster circuitry consisted of the 6mA HV power supply, connected to the 115 μF HV capacitor bank capable of charging up to 2000V, although test voltages were limited to 1800V to provide some margin. This high voltage capacitor bank was connected in series through a 268-1000 ohm resistor to the anode of the VAT circuit. The screen grid was then connected in series to the VAT anode through a 100 ohm (R1) resistor. In this way the screen grid potential was kept very close to the high voltage supply potential but with reduced chance of arcing due to this screen grid resistor.

3.6.3 Summary of measurement equipment

With the structures and circuitry outlined above the ion thruster was able to operate well over a range of voltages from 800-1700V and reliably produce ion beam pulses of 30-40mA lasting 200-300 μs. The VAT arc current and the screen grid current were both measured using the inductive transducers outlined in section 2.2.4. The accel grid current and the ion collector plate current were both measured simply by the voltage drop of their resistors going to ground.

In summary, vacuum arcs generated plasma at high potential by the modified coaxial VAT design and floated VAT circuit with an arc current measurement being made. The majority of these ions condensed on the VAT extended anode grid and the glass walls of the plasma containment vessel. A small fraction of the VAT ions streamed towards the screen grid where they were accelerated with the high voltage capacitor bank providing the current to do this. This current was measured with a second transducer and is known as the screen grid current. Some of these accelerated ions impacted the accel grid on their way out of the thruster due simply to misalignment or imperfect focusing of the ion beam due to space charge effects and this current was measured by the voltage drop across the accel grid resistor. Another fraction of these ions impact the grid insulators and alignment wires as they are in direct view of the beam. This contributed to the conductive build-up which ultimately lead to arcing issues described in detail in section 5.2. The majority of the ions accelerated by the grids finally make their way out of the thruster where they either impact and stick to the ion collector plate, or collect an electron from the plate, recombine and depart as a neutral. In both these cases a net current is drawn from ground through the plate resistor and this is known as the beam current.

3.7 Chapter summary and review of final ion thruster

To conclude this chapter and prepare us for the results that follows, let us review the final ion thruster design and the measurement setup once more.

The final ion thruster setup is shown in figure 3.9. The VAT PPU shown in this diagram is a simplified block representing the circuit shown in figure 3.6. The VAT is shown inside the glass plasma containment vessel and is arcing and producing a plasma plume shown in blue. The VAT used is the modified coaxial design with the extended anode grid to reduce the peak arc currents. The VAT anode and cathode are connected to the VAT PPU. As in figure 3.1, the anode and extended grid anode are shown in orange, the VAT insulator in grey and the VAT cathode in maroon. The VAT arc current is measured with a custom built current transducer described in the beginning of this chapter and labelled T1 in this diagram. The current transducer is placed on the cathode lead of the VAT and provides the arc current measurement to the oscilloscope whilst remaining completely isolated from the VAT circuit. The high voltage supply is connected in parallel with the high voltage capacitor bank. Together, the bank and supply are connected in series through the screen resistor R_{screen} and then to the anode lead of the VAT PPU. Typical test values for the high voltage supply were $800-1800V$. The screen resistor value was 268Ω. The screen grid current measurement is made through a second custom transducer labelled T2. The screen grid is connected to the VAT anode through a 100Ω resistor R1. Thus the screen grid makes its connection to the high voltage capacitor bank through the resistors R1 and R_{screen}. The accel grid was connected to negative side of the accel supply through a 220Ω resistor R2. The resistors R1 and R2 are not strictly necessary but helped to prevent grid arcing. The accel supply is then connected to ground through the measurement resistor R_{accel}. The accel grid current is measured across this resistor as V1. The accel supply voltage was 125V throughout testing. Finally the ion collector plate was connected to the negative side of the plate supply. This supply was not necessary as during proper operation the ion thruster produced only ions and no electrons and so there was no need for the negative plate supply voltage to reflect electrons. Testing showed that there was no difference to the ion current measured as the plate supply was changed from 0-32V. The plate supply was then connected through the measurement resistor R_{plate} to ground. The plate current, which is simply the total ion current that leaves the thruster and hits the plate can be considered to be the beam current and was measured through the voltage V2. The vacuum chamber, oscilloscope and high voltage supply negative terminal were all connected to the earth ground shown in the figure 3.9. It should be noted that figure 3.9 is not to scale. During testing the VAT was approximately $90mm$ from the screen grid, the accel to screen grid separation was $0.75mm$, and the ion collector plate distance from the accel grid was varied between $10-25mm$ with no change in the measured ion current.

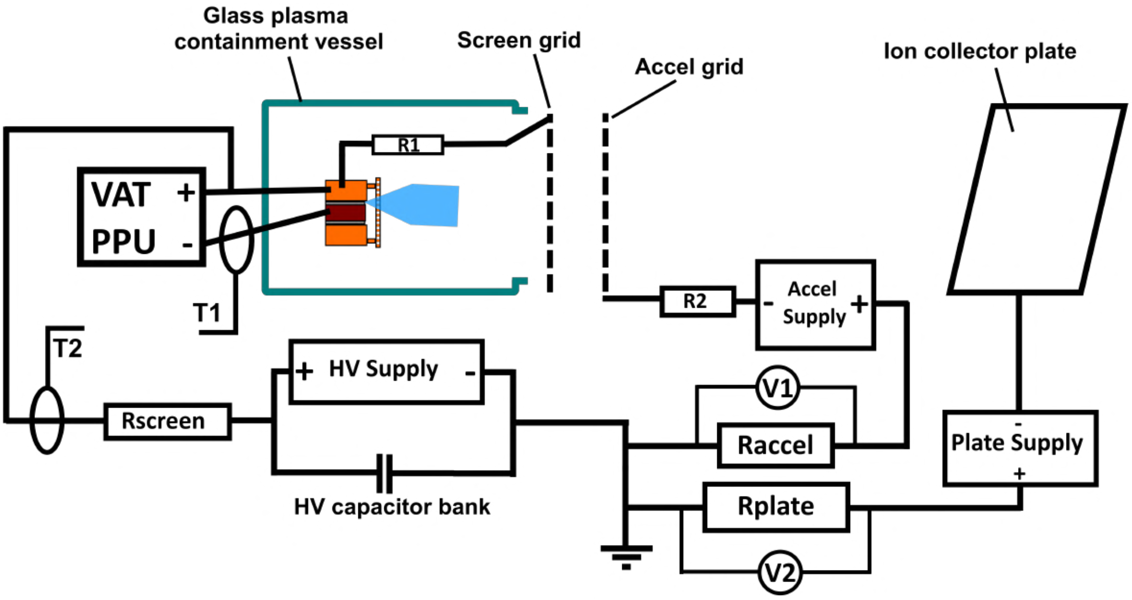

FIGURE 3.9: Schematic showing the final ion thruster testing setup including all four signals that were measured.

The equipment outlined in chapter 2 enabled measurements of the thrusters just discussed and these results are discussed in the following chapter.

Chapter 4

Results

In line with the goals of this dissertation, the results section can be separated into two broad categories: First, there were tests that characterised the VAT plasma sources. These tests aimed to determine the suitability of the VAT plasma for an ion thruster and to determine improvements that could be made to produce a working thruster. This includes the total ion current measurements made on the various candidate VAT plasma sources, and also the inner versus outer ion current density tests conducted with the annular collector shown in figure 2.6. The second set of tests focused on the operation of the ion thruster, and the various grid arcing issues that were encountered.

The total ion current measurements were done early on in this work to determine the suitability of the VAT as a plasma source for an idealised ion thruster. Thus the key result of these tests was the measurement of the ion fraction, which ultimately determines the ionisation efficiency of the source. Design 3 had a space charge limited current maximum of 190mA (equation 3.3), and the lowest ion current produced by any VAT tested was several amps. All the VATs tested in this work produced many times more ion current than could be accommodated by Design 3's grid system - thus, the ion fraction of the final VAT source used (modified coaxial) was not relevant, and in fact was purposefully reduced so that an appropriate amount of ion current would be presented to the grids. The total ion current and ion fraction measurements then provide upper bounds on the efficiency of the VAT plasma source for an ideal ion thruster that could utilise all of this ion current.

4.0.1 Cathode and anode materials

During the total ion current measurements, cathodes of pure bismuth (99.9%) and mild steel were tested. The mild steel was 98.7 % iron. The final VAT source used (modified coaxial with extended anode) ran a pure (99.9 %) copper cathode. Copper was chosen as the cathode material because it is the most well researched vacuum arc cathode, which allows easy analysis to the literature and to use accurate literature values for certain calculations - such as the copper vacuum arc electron temperature and erosion rate. All thruster anodes were pure copper except for the planar thruster which had a mild steel anode - identical to its cathode. All thrusters used the 'trigger-less' arc triggering method described in the introduction and in Anders et al. (1998). Thus there was a thin graphite layer drawn across the anode-insulator-cathode of all the thrusters. Thus the author notes that there may have been some carbon plasma in the arc, however this was not considered to be significant. Additionally all tests allowed several arcs to take place before measurements were taken - this ensured that the arcs had 'burned-in' and stabilised and also reduced the possible contamination of carbon in the plasma Anders (2009).

4.1 Inner vs outer ion current density measurements

Using the annular ion collector shown in figure 2.6, the difference in current density between the middle of the grids and the outer area could be determined. The inner collector had an ion surface collection area of $7.085 \pm 0.05cm^2$ and the outer ring collector an area of $19.72 \pm 0.05cm^2$. Two tests were run, a high ion current density test where the thruster was just $65 \pm 0.5mm$ away from the vessel lid, approximately in the middle of the vessel, and a low ion current density test where the thruster was $95 \pm 0.5mm$ away, close to the back of the vessel.

Distance (mm)	Inner collector (mA/cm^2)	Outer collector (mA/cm^2)	% increase
65±0.5	18.87±0.3	13.90±0.3	36
95±0.5	1.41±0.3	1.15±0.3	23

TABLE 4.1: Inner compared to outer ion current density measurements

As can be seen from the results in table 4.1, there was a maximum 36% increase in the ion current density along the thruster centerline when compared to the region at the outskirts of the grids. This difference was reduced to just 23% when the thruster was moved back 30mm. As all ion thruster testing was conducted with the thruster approximately $90 \pm 5mm$ away from the vessel end, it was concluded that this modest increase in ion current density would not significantly affect the performance of the device. Most ion thrusters can tolerate an increase or decrease in the beamlet current over a narrow range of approximately plus or minus 50% (Goebel & Katz (2008)). While the above test was not able to measure individual beamlet currents, the ion current density in the center can be considered an average of the center beamlets beam current density - and vice versa with the outer ring. Thus, the modest 23 % increase was deemed to be acceptable for testing.

4.2 Total Ion Current Measurements

The testing circuit was a standard one stage VAT circuit with a single 4.7mF capacitor and 55mH inductor shown in figure 3.6. The vacuum chamber was pumped down to $5 \times 10^{-8} Torr$ before testing began. The only parameter changed during the tests was the negative bias voltage on the ion collector. All other parameters were kept constant across the three different tests with only the VATs changing. The three VATs tested are shown in figure 4.1. The total ion collector was set up as shown in figure 2.2.

FIGURE 4.1: The three VATs used for the total ion current tests. Left to right: Bismuth coaxial thruster showing clear cathode erosion, coaxial steel thruster with minor erosion and planar steel thruster during arc operation.

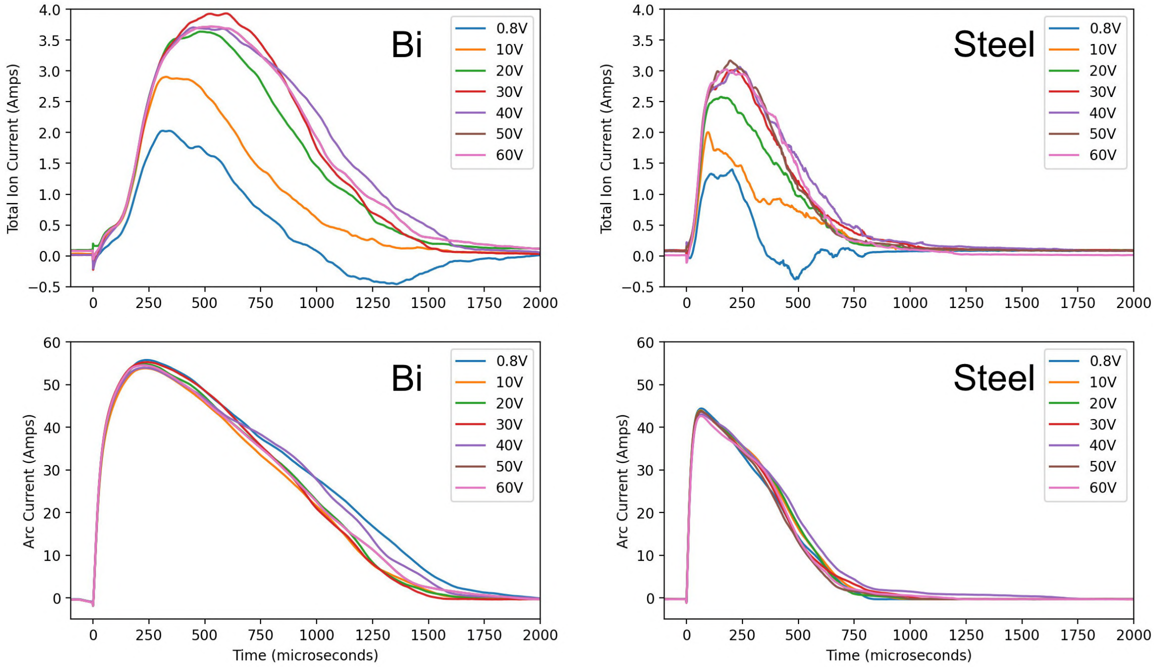

FIGURE 4.2: Coaxial thruster total ion and arc currents over the range of ion collector negative bias voltages tested. Left: bismuth. Right: Steel. The legend denotes the negative bias voltage on the collector plate. At the small negative bias of 0.8V, a large proportion of the electron current is not yet repelled sufficiently, leading to the negative ion current (electron current) readings at this value.

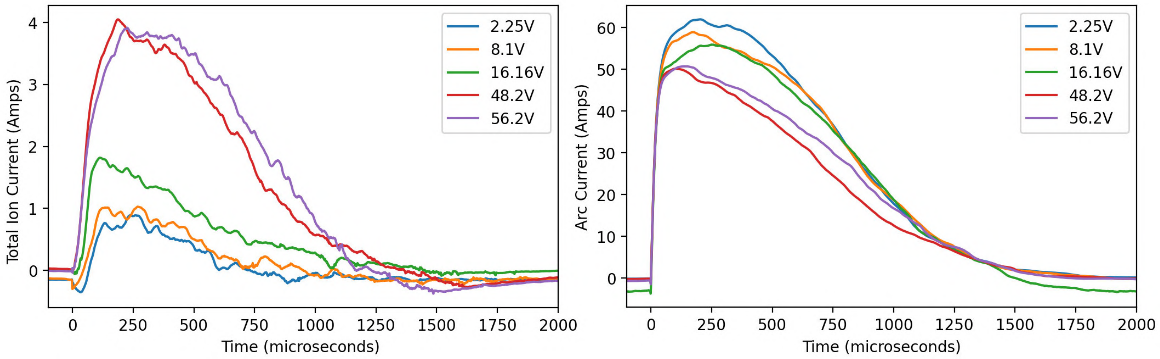

FIGURE 4.3: Planar steel thruster ion and arc currents over the range of ion collector negative bias voltages tested denoted by the legend.

4.2.1 General findings

Average total ion and arc current measurements are shown in figure 4.2 for the coaxial thrusters, and in figure 4.3 for the planar steel thruster. The legends in figures 4.2 and 4.3 denote the negative bias voltage on the ion collector. The time has been zeroed to the start of the arc pulse. The arc burns until the current drops below the minimum threshold necessary to sustain the arc, the arc chopping current. As bismuth has a lower discharge voltage than iron, 15.6V compared to 22.7V, Polk et al. (2008), it can sustain the arc for longer before reaching the chopping current. This is clearly seen by the difference in arc length between the two coaxial thrusters in figure 4.2. The coaxial bismuth arcs lasted approximately 1500μs while the coaxial steel arcs lasted only 750μs. The planar steel thruster arcs lasted 1500μs despite having the same cathode material as the coaxial steel thruster and thus the same higher discharge voltage. This may be due to the geometrical differences. The planar thruster had a 1mm thick insulator compared to the 3mm insulator of the coaxial thrusters. This could have reduced the plasma resistance as there was less distance for the arc to bridge from anode to cathode thus prolonging the arc. Secondly, the cathode had a direct line of sight view of the anode in the planar design, compared to the coaxial design where the plasma bridge would have to be above both cathode and anode. Note again that the circuit used and all other testing parameters were identical between the three different tests, only the VAT thruster was changed.

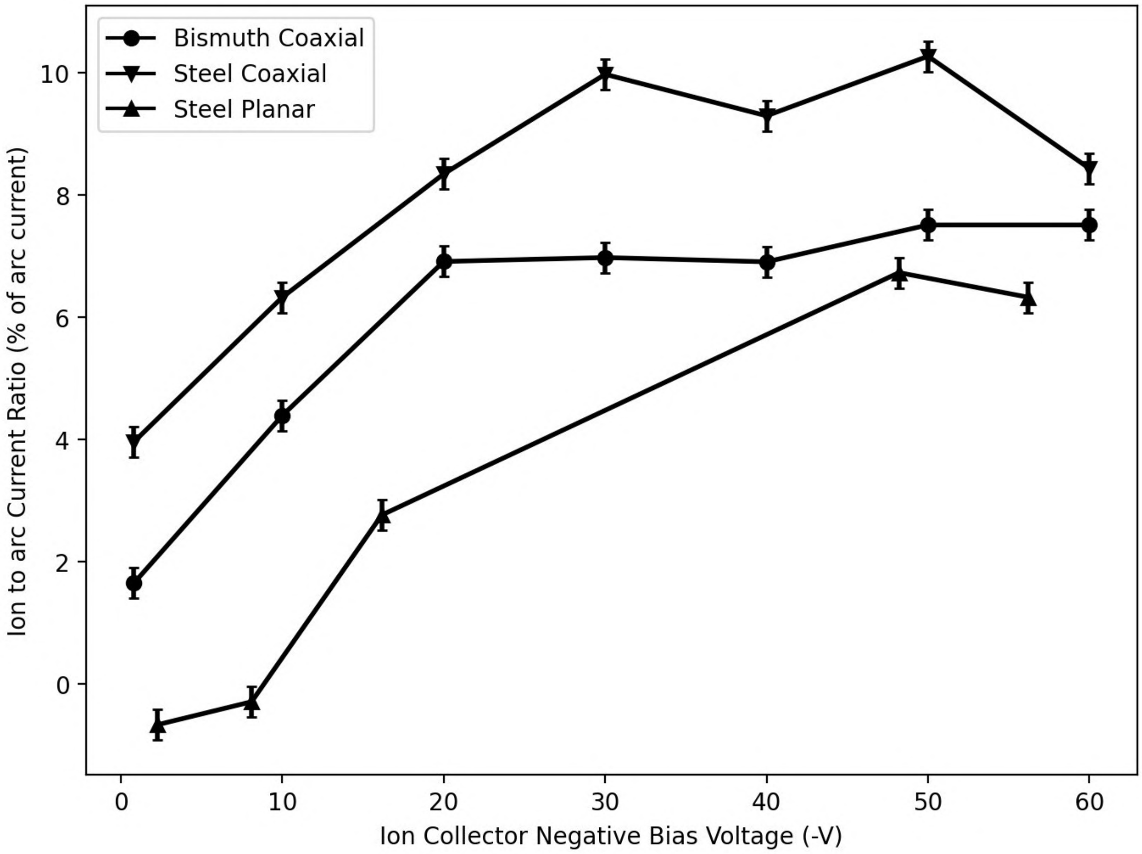

FIGURE 4.4: Ion to arc current ratio versus ion collector negative bias voltage, expressed as a percentage of the arc current.

4.2.2 Ion to arc current ratios

Figure 4.4 shows the ion to arc current ratio expressed as a percentage of the arc current for all three thrusters. As bismuth has a much lower cohesive energy than iron, 2.18 vs 4.28 eV/atom Kittel & McEuen (2018), it was expected that the coaxial bismuth thruster would produce the highest ion to arc current ratio Anders (2009). However, it was the coaxial steel thruster that had the highest ratio measured at $10.27 \pm 0.5\%$, followed by the bismuth thruster at $7.5 \pm 0.5\%$ and finally the planar steel thruster at $6.73 \pm 0.5\%$. These values are in broad agreement with the literature where ion fractions of $5 - 10\%$ are commonly observed. However, bismuth is often reported to have a higher ion fraction than other materials, up to about 12% Boxman (2001). The fact that the coaxial steel thruster produced significantly more ion current for a given arc current is interesting and warrants further investigation.

One possibility is that the bismuth cathode began melting and so produced fewer ions. The fact that the bismuth arcs burned at higher arc currents and for approximately twice as long as the steel arcs, coupled with bismuth's much lower melting point lend support to this idea Anders (2009).

4.2.3 Ion current plateau

Anders (1997) used ion charge state distributions to calculate the vacuum arc plasma electron temperatures for a wide variety of metals. From these results, bismuth was shown to have an electron temperature $T_e = 1.8eV$, iron $T_e = 3.4eV$ and carbon $T_e = 2.0eV$. The electron temperate of carbon is relevant because it may have slightly lowered the overall electron temperature of the steel cathode. Comparing the steel coaxial and bismuth coaxial thrusters to avoid any geometrical effects possible with a comparison with the planar thruster, figure 4.4 clearly shows a plateau in the ion to arc current ratio as the negative bias is increased. For the bismuth coaxial thruster this plateau is clearly seen to start at $V = -20V$ bias, whereas it appears to start around $-30V$ for the coaxial steel thruster. Equation 1.14 gave the Boltzmann electron density relation, repeated here.

$$n_e = n_0 \exp(\frac{e\phi(r)}{kT_e}) \tag{4.1}$$

Plugging in the electron temperatures from Anders et al. (2001) and the negative bias voltages, and assuming the initial densities are the same, the relative electron densities of iron and bismuth plasmas at the ion collector held at a constant negative $20V$ is,

$$\frac{n_{e\ Fe}}{n_{e\ Bi}}|_{-20V} = \frac{n_0 \exp(\frac{-20}{3.4})}{n_0 \exp(\frac{-20}{1.8})} = 186 \tag{4.2}$$

In other words, at -20V the electron density of iron plasma should be almost 200 times higher than that of bismuth plasma. This is why the bismuth coaxial thruster ion to arc current ratio plateaus before the steel coaxial thruster.

4.2.4 Note on data exclusion

During the planar steel thruster ion current measurements, there was an issue with the power supply limiting the current. These results were excluded and new tests were repeated with the same supply used for the coaxial thruster tests but at higher voltages. Unfortunately this lead to a lack of data points over the range 20-40V, however the trend of ion current saturation does still appear if somewhat less robustly.

4.3 Grid Arcing

As the ion grids consist of two conductive perforated metal sheets spaced less than 1mm apart (the insulators separating the screen and accel grid during testing were $0.75 \pm 0.05mm$ thick), and with a potential difference of up to 2000V, it was easy for an arc to form. And given that there is a large capacitor bank connected to the grids this results in a powerful discharge seen in figures 4.5 and 4.6, which was confirmed by the voltage traces. The grids arc when there is a conductive path provided for them to short circuit to each other. This can happen, and was observed in a number of different ways:

4.3.1 Conductive buildup short circuit arcing

Firstly, due to the design of the thruster, the insulators and grid alignment wires were in direct path of the plasma. This meant that after only a short amount of VAT operation, there was enough of a conductive coating layer built up that would short out the grids. Using copper cathodes, this happened after only 20-30 arc pulses and ultimately placed a hard limit on continuous operation of the system, as the chamber had to be vented, the grids disassembled and then the insulators and grid alignment wires cleaned in a methanol ultrasonic bath before the thruster could be operated again. This arcing was unavoidable with the final design that placed the insulators and grid alignment wires in direct view of the plasma. This is called conductive buildup short circuit arcing. Evidence of arcing on the grids and insulators can be seen in figures 4.7 and 4.8 and arcing on one of the grid alignment wires can be seen in figure 4.9.

FIGURE 4.5: Typical grid to grid arc.

FIGURE 4.6: Typical grid to grid arc.

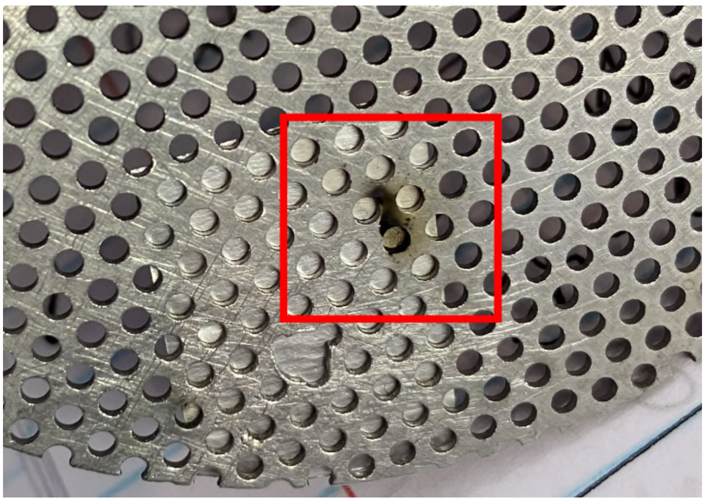

FIGURE 4.7: Evidence of grid arcing on the disassembled grids.

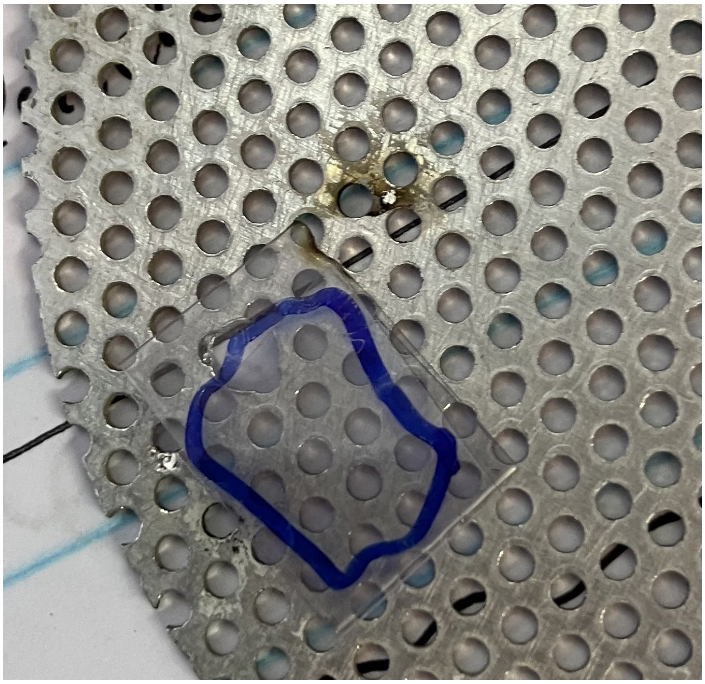

FIGURE 4.8: Another example of grid arcing on the disassembled grids. The blue rectangle shape was drawn onto the grid insulators so that they could be positioned properly between the grids. It is simply a cosmetic feature to help with grid assembly.

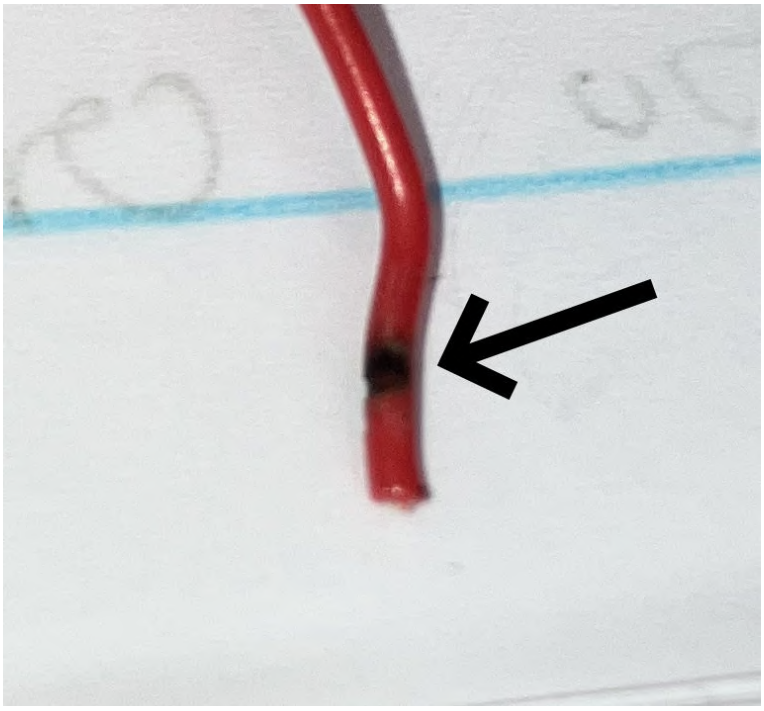

FIGURE 4.9: Clear signs of arcing on the grid alignment wires.

4.3.2 Space charge limit arcing

The second kind of grid arc is caused by space charge effects. From the Child Langmuir equation, there is a hard limit on the maximum ion current density that can be extracted by a grid system for a given electric field strength. This depends on the grid voltage and the grid gap, and to some extent the aperture size plays a role. Essentially, as more and more positive charge builds up between the grids the electric field between them eventually drops to zero. At this point, the maximum ion current is being extracted and the condition is known as the space charge limit. If the ion density is not well matched to the grid system, more ions may try to move into the grid gap, as this happens electrons will unavoidably be pulled into the gap at the same time to balance out the space charge of the ions. Now the grid gap is full of a highly conductive plasma and so the grids will arc together. Due to the fact that all the VATs used in this work produced orders of magnitude higher peak ion currents than could be tolerated by the grid systems, this type of arc was by far the most common and can be seen in figures 4.5, 4.6 and 4.13.

4.3.3 Plate arcing likely from secondary electron emission

In this type of arc, the arc begins between the grid system and the ion collector plate some 10mm downstream from the accel grid. In this arc, the thruster and grids behave nominally, and the arc is triggered through an interaction with the plate.

Secondary electron yields

When high energy ions impact a surface they will produce a population of secondary electrons primarily depending on the secondary electron yield (SEY) of the surface and the energy of the incoming ion, Haque et al. (2019). The SEY of the surface may also change depending on what type of ion impacts the surface, even for constant ion energy, and there is also a dependence on the angle of incidence of the incoming ion. The surface structure and any impurities may also have a large effect on the SEY. While the SEY was not measured in this work an estimate of the SEY can be made from data in the literature. The brass plate used as the ion collector was over two thirds copper and the angle of incidence was 0°. The SEY for copper under bombardment of 1.5keV protons was calculated to be 0.25 by Haque et al. (2019). Svensson et al. (1981), found that for 40keV incoming ions on a polycrystalline copper target - the SEY under bombardment of copper ions was up to 250% higher than when the same target was bombarded with noble gas ions of the same energy. Assuming a SEY coefficient on the order of 1 would imply that for each mA of incoming ion beam current, there would be an approximately equal secondary electron current generated.

Potential mechanism for arcing

The accel grid was biased to -125V to prevent any electrons generated downstream from moving upstream into the thruster and causing arcing. However, it is possible that during the pulse the ion charge in the beamlets (individual ion beams from each aperture) could have raised the space charge potential in the accel grid apertures. This would mean that even though the accel grid was at -125V, the potential inside a narrow region of the aperture would be compensated by the positive ion space charge and therefore the potential at this region in space could be much closer to 0V, Wirz et al. (2011). This increase in the potential would allow some of these

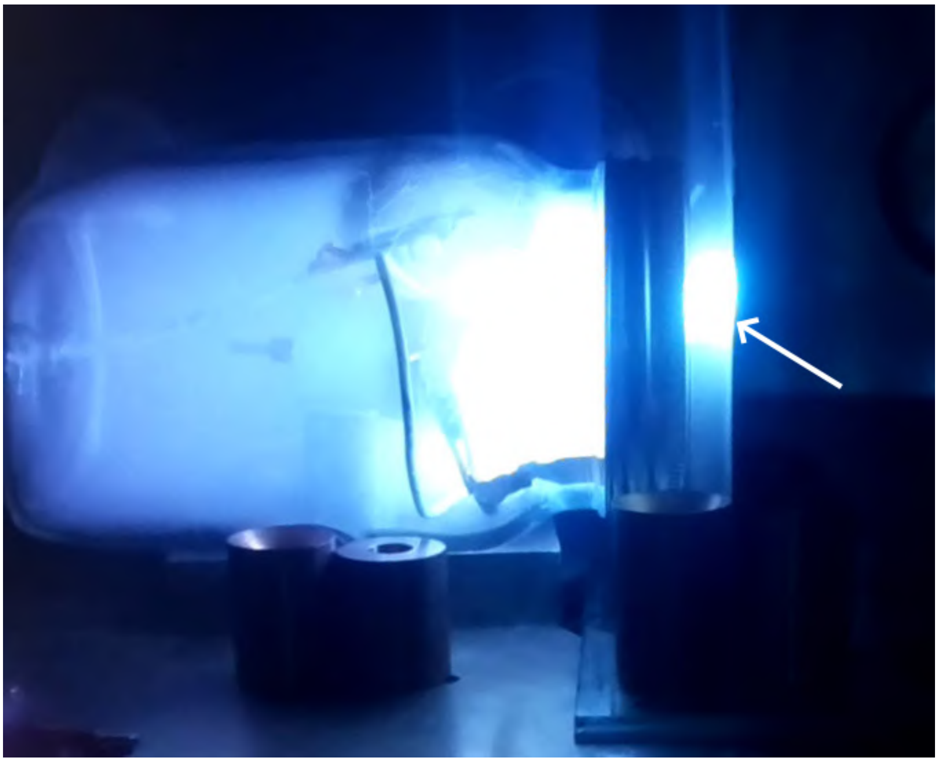

FIGURE 4.10: Grid to plate arc. Note the arc attachment on the ion collector plate 10mm downstream from the accel grid, shown by the arrow.

low energy secondary electrons to move upstream into the thruster and initiate the arc.

Evidence of this arc type

Figure 4.10 shows an example of such a grid to plate arc believed to have been caused by this interaction via secondary electrons. The next section discusses the observation of a transition from a grid to plate arc which was most likely caused by secondary electron emission - to a grid to grid arc. A grid to grid arc was triggered likely without the ion current density from the VAT exceeding the grid extraction capabilities.

4.3.4 Arc Transition

In tests where the ion thruster beam impacted a collector plate placed a short distance downstream (some 10-20mm), an interesting arc transition was observed. Looking closer at the oscilloscope trace showing the arc transition in figure 4.11 it is clear that for the first 100us of the arc everything operates nominally. The arc current (cyan) produces the ions that are accelerated by the grid system shown by the screen supply voltage drop (turquoise). A small number of these ions then strike the accel grid (black) causing a small increase in this signal, while most of the ions hit the ion collector plate (purple). After approximately 120us into the arc (at time 0.22ms on the x axis), both the screen current and ion collector plate current shoot up to infinity. Note that by infinity we mean the maximum possible value of current that occurs during a short circuit and is off the scale. This is the signature of a screen grid to plate arc. There is no accel grid involvement in this arc and its value stays relatively constant during this period. It is likely that this initial screen grid to plate arc was caused by the secondary electron and ion charge compensation described above. The dotted line at 0.3ms is a point during which the screen grid to collector plate arc is continuing with no accel grid involvement. Note that the screen grid is only 1mm away from the accel grid, whereas it is 11mm away from the collector plate. At time t=0.4ms the arc transitions from this screen grid to plate arc to an accel grid to screen grid arc. This is seen by the sharp drop in the plate current which coincides with the sharp rise in the accel grid current to infinity. The plate current drops to a level below both the level when it was participating in the arc (effectively infinity) and the level during proper operation in the beginning of the pulse. The plate current value after the transition of a few milliamps is consistent with the ion bombardment from the grid-grid arc happening 10mm from the plate. Note also that this arc transition occurred at a higher arc and ion beam current level. During this particular pulse, the arc current reaches a peak above 35A (compared to the typical 30A) and the ion beam current that intercepts the plate peaks at over 30mA, compared to typical values of 20-25mA. This higher than usual ion beam current likely lead to this arc for two reasons. Firstly, the higher ion beam current could have caused more space charge compensation in the accel grid apertures thus raising the potential in these regions. Secondly, this higher ion beam current would have caused a larger number of secondary electrons to be emitted from the plate. The combination of these factors most likely caused this type of arc.

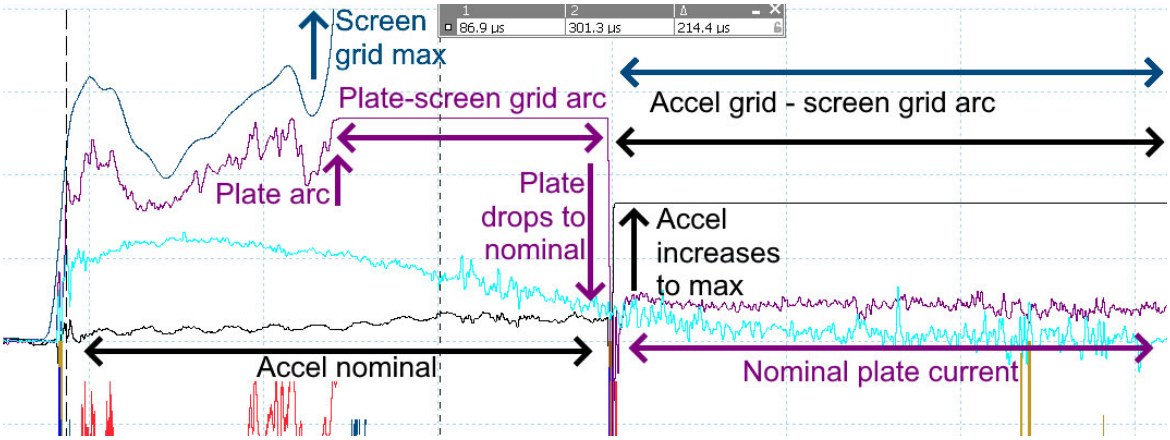

FIGURE 4.11: Oscilloscope trace showing arc transition: The screen current (dark turquoise/blue), plate current (purple) and accel grid current (black) are all on the same scale from 0-48mA. The arc current is in cyan and has its scale from 0-120 amps. The arc transitions at t=0.4ms.

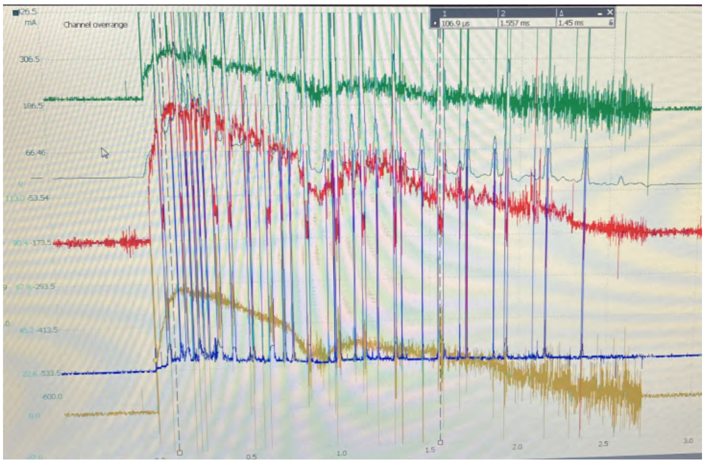

FIGURE 4.12: Mini arcs

4.3.5 Semi-stable Ion thruster operation results

As should be clear from the previous section, grid arcing was a constant source of error during testing. Before proper ion thruster operation was achieved, a semi-stable mode of operation was achieved. The thruster was able to briefly operate correctly with a number of mini-arcs. Essentially due to the chosen resistor values, every time an arc was initiated the voltage would quickly drop to zero and the arc would be extinguished. This led to the large number of spikes as shown in the oscilloscope trace seen in figure 4.12 - each spike represents an arc.

FIGURE 4.13: Grid arc sequence: Top: t=0 During the VAT pulse, no sign of arcing. Middle: t=42ms the VAT pulse has long extinguished and the grids are arcing. Bottom: t=84ms the grid arc continues at lowered intensity; sufficient time has passed for the VAT capacitor to partially recharge and due to the abundant conductive plasma from the grid arc the VAT reignites.

4.4 Proper Ion Thruster Operation

This section summarises the results obtained from the final ion thruster and VAT plasma source that worked together.

4.4.1 Setup

Using the final three stage PFN circuit shown in 3.6, with 224 μF of total capacitance, firing a copper cathode in the modified coaxial VAT with extended anode shown in figure 3.4 placed 90mm away from the screen grid, and using the electrical setup for measurements as shown in figure 3.9. The VAT circuit voltage was 35V. The screen grid voltage was 1530V, the accel grid voltage was -125V and the collector plate voltage was -30V.

4.4.2 Relative Errors

Using linear error propagation the relative errors of the voltage measurements were calculated. The oscilloscope used in all four measurements had a relative error of 2%, the accel grid and plate currents used 5% resistors for a total relative error for these measurements of $5 + 2 = 7\%$. The arc current and screen grid current measurements used the same 5% error resistors, with the same oscilloscope but there was an additional 1% error associated with the inductance measurement for a total relative error of $5 + 2 + 1 = 8\%$

Arc Current	Accel grid current	Screen grid current	Plate current
8%	7%	8%	7%

TABLE 4.2: Relative errors of the four key measurements.

4.4.3 Note on data processing

The final data set presented here is from 18 consecutive pulses out of a pulse chain of 20 pulses, the first pulse did not trigger properly and the second pulse displayed high amounts of noise and most likely this first pulse burned through some oxidation layers on the cathode. The following 18 pulses all worked perfectly and it is the data from these pulses that is represented and averaged. Note that as many pulses

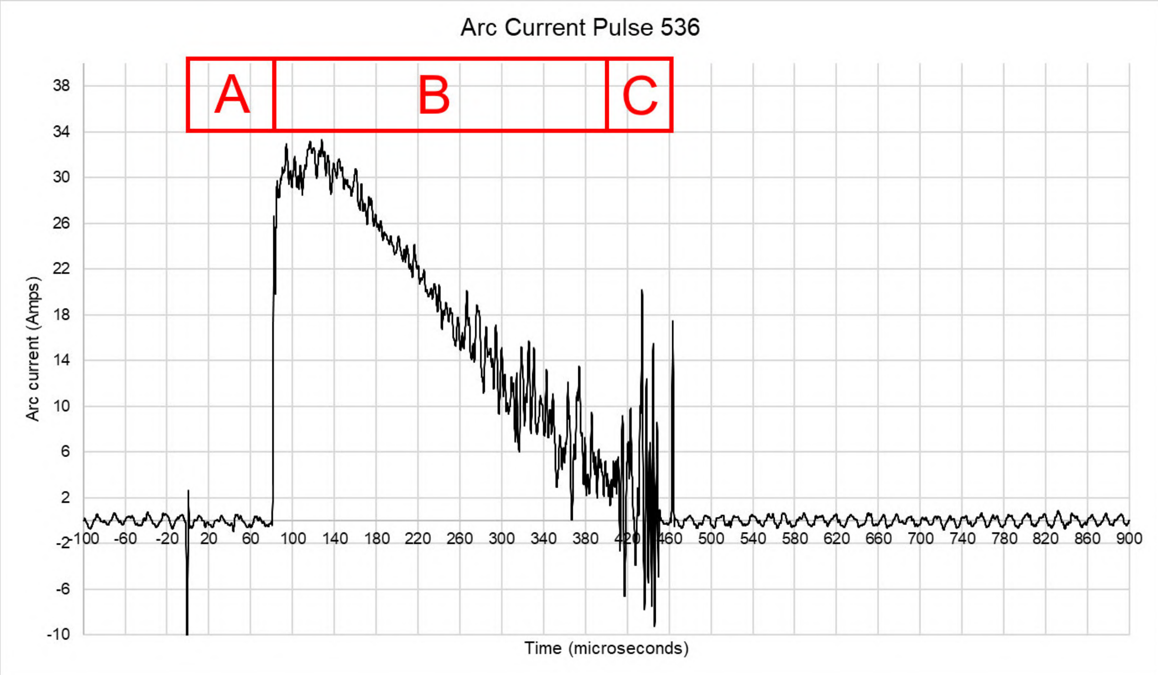

FIGURE 4.14: Arc current trace for pulse 536 illustrating the different regions of arc operation. In region A, the inductor charges for 80 microseconds before the arc ignites. In region B the arc burns reaching its peak and continuing to burn stably until it reaches an arc current level too low for stable operation, leading to a final stage of unstable arc burn and extinguishment in region C.

were run the pulse names are higher than the total pulse number. For instance a particular pulse is referred to as pulse 536, because that was the 536th pulse fired on that day of testing. The conductive build up problem meant that the system developed arcing issues within approximately 40 pulses of operation. That is why the final data set that is analysed below of proper ion thruster operation includes only 18 pulses.

There was also a slight offset in the signals for all four measurements, which was removed from the data. The offsets are summarised below:

Arc Current (A)	Accel grid current (mA)	Screen grid current (mA)	Plate current (mA)
0.72 ±0.06	0.26 ±0.02	0.64 ±0.05	1.9 ±1.33

TABLE 4.3: Current value offsets removed from data.

4.4.4 Arc Currents

The circuit and VAT reliably produced arc current traces such as the one shown in figure 4.14. Three regions characterise the arc current trace: the charge pulse and arc initiation region A, the stable burning of the arc B and the unstable arc burn leading to extinguishment C.

In region A, the IGBT opens to charge the inductor which can be seen as a sharp spike in the current trace at t=0. Once this charge pulse ends at t=80, the IGBT closes and the arc begins to burn (region B). The arc current reaches its peak within 50 $\pm$5 microseconds of ignition, and then gradually decreases throughout the burn. After burning for 320 microseconds, the arc current has reduced to a level below which it cannot continue to burn - known as the arc chopping current, approximately 5A for this arc. Thus the arc enters a region of significant instability leading finally to its extinguishment (C). A full millisecond of data is presented to show that after the arc operation ends, there are no grid arcs or any other unwanted phenomena.

Turning our attention to the next graph, figure 4.15; which shows the screen grid current, plate current and accel grid current for the same pulse. We see that the ion thruster is working. The plate current, which represents the captured ion beam current downstream of the thruster, closely follows the screen grid current. In other words, the arc plasma ions are successfully accelerated by the screen grid and then successfully travel downstream out of the thruster where they impact the plate. Thus the plate current closely resembles the screen grid current, with a small delay - exactly as expected. This is especially clear when looking at the moderate screen current drop which causes a similar drop in the plate current just a few microseconds later. The accel grid current shows a roughly constant value throughout the pulse representing that small fraction of the total ions accelerated that do not make it out of the thruster and instead impact the accel grid.

4.4.5 Beam interception and Accel to Screen grid current ratio

When an ion thruster is operating at the optimal ion current density and voltage for its grid geometry it will be able to extract a maximum amount of beam current. This was shown in figure 1.9. Figure 4.16 shows the accel grid to screen grid current ratio averaged over the 18 pulse data set and gives insight into how this ratio changed

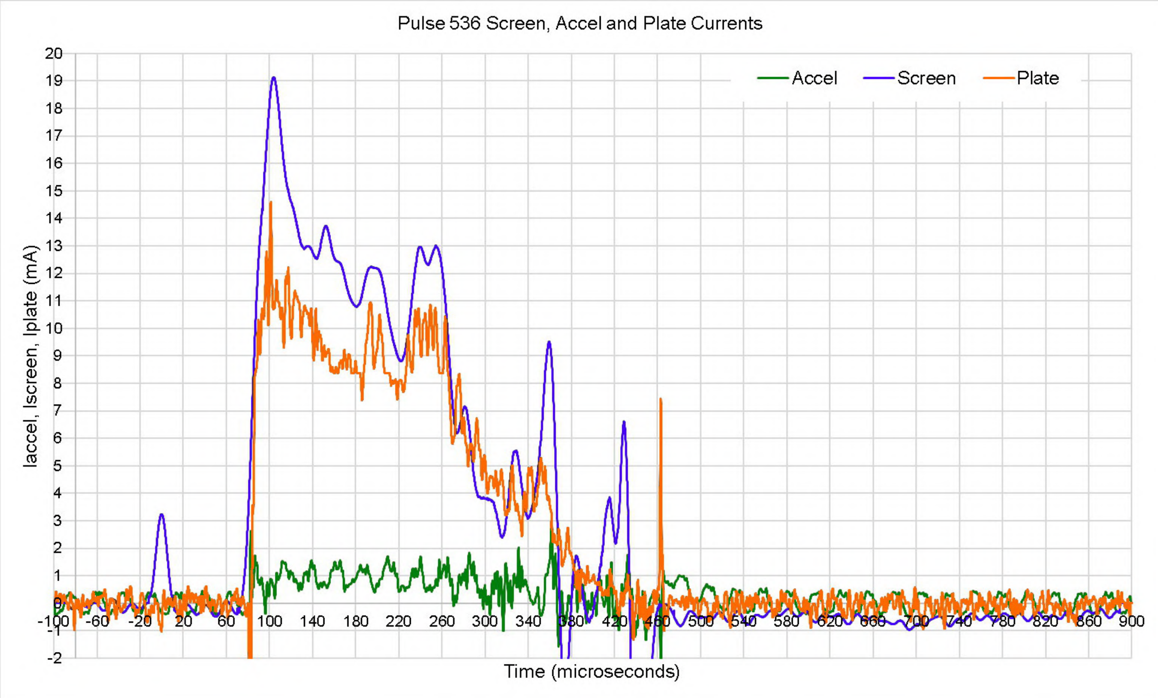

FIGURE 4.15: Screen accel and plate current trace for pulse 536

over the pulse. Note that the ratio is undefined before the pulse begins (around 85 μs) and after it ends (around 420 μs). As shown in figure 4.14 the arc current and thus the ion current have a rapid rise time with a long decreasing slope for the rest of the pulse after the peak. As the ion current drops toward the end of the pulse, two effects come into play. The lower ion current means that there are simply fewer ions around to impact the accel grid and so we expect this to reduce the ratio. On the other hand, the lower ion current necessarily means that for the same grid system and voltage, assuming the source was operating at under perveance, see equation 3.3, the lower ion current will lead to more cross over impingement on the accel grid thus increasing the ratio.

Percentage of space charge limited current

As described in equations 1.54 and 3.3, the maximum space charge limited current that Design 3's grid system could extract was calculated to be $\approx 190mA$. In this particular pulse (figure 4.15) the peak value of the screen grid current is just over

19mA, the average screen current peak over the 18 pulses shown in figure 4.17 is only 16mA.

$$I_{screen}/I_{max} = \frac{19}{190} \approx 10\% \tag{4.3}$$

this suggests the ion thruster is operating far from the space charge limit and is in the under-perveance regime. As can be seen in figure 4.16 the ratio is nearly constant from $t = 100\mu s$ to $t = 280\mu s$. From $t = 280\mu s$ until the end of the pulse at $t = 420\mu s$, the accel to screen grid current ratio sharply increases. This provides more evidence that the source was operating in an under-perveance regime, because as the total ion current decreases, the accel grid current increases. If the source were operating in an over-perveance regime, then a decrease in the ion current would correspond to more optimal perveance and the accel grid current would go down. We conclude that the ion thruster is operating far from space charge limited conditions in the regime of under-perveance. This is likely the reason for the high ratio of $I_{accel}/I_{screen} = 0.1$ during the pulse, with neutral CEX collisions (discussed in the next chapter) and grid misalignment potential contributing factors as well.

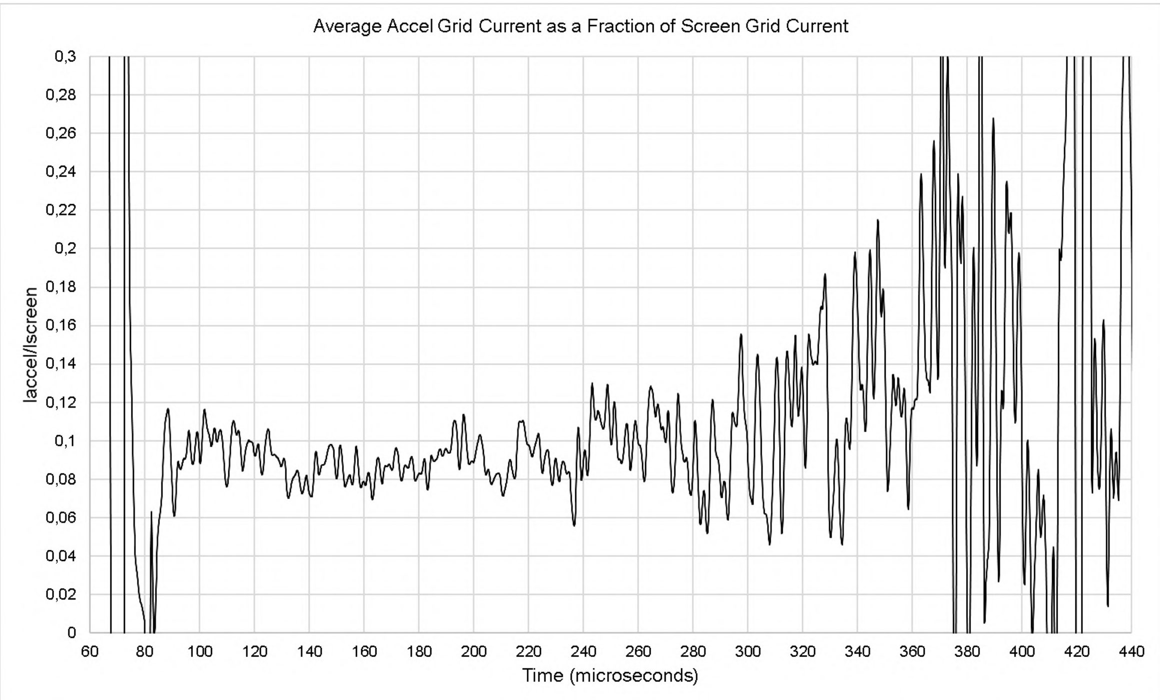

FIGURE 4.16: Accel to screen current ratio

4.4.6 Stable operating point: Accel grid, screen grid and collector plate measurements

Figure 4.17 shows the averaged screen grid current, accel grid current and plate current on the primary axis (left hand side). The averaged arc current is also plotted with its scale on the secondary axis (right hand side). From this graph we can see the entire operation of the ion thruster. At t=0, the arc trigger pulse is initiated , this causes a sharp spike on the arc current trace. A spike is also recorded by the screen grid current even though there is no screen grid current flowing - this is simply due to the EMI generated by the pulse that is picked up by the inductive measurement circuit. The arc ignites at t=80μs.

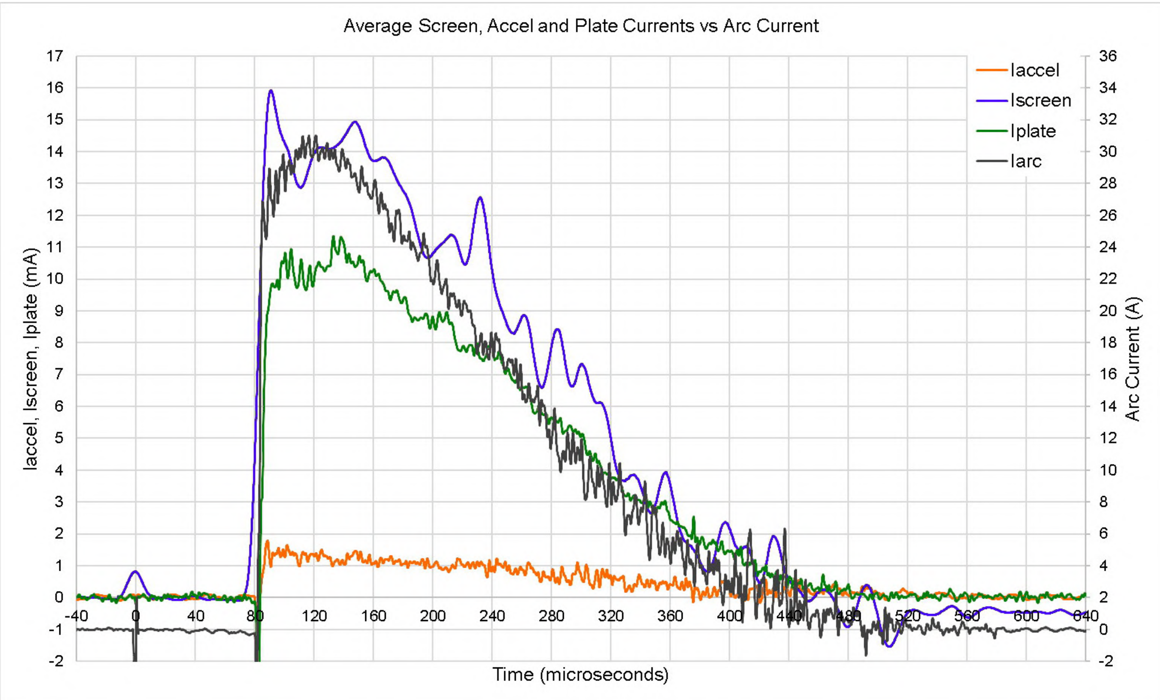

FIGURE 4.17: Average Screen, Accel and Plate Currents vs Arc Current

In an ion thruster one desires a uniform and consistent plasma density. In the VAIT, this is determined by the arc current trace which in turn is determined by the VAT circuit architecture. As discussed, one desires a roughly square pulse with short rise and fall times. In other words, the arc current should rapidly get up to its desired level, stay there for the required amount of time and then rapidly decay back to zero at the end of the pulse. The final circuit reliably produces arc traces of the shape seen in figure 4.14. These arc traces clearly have the short rise times desired, however they have very long decay times. Another problem is that the final 50μs of the arc pulse are extremely noisy and unstable. Ideally the arc current pulse would be much more square with a much shorter decay time. With this in mind, we may examine the first 100μs of ion thruster operation and consider this the stable operating point from which we can take average readings. This is justified because it is reasonable to expect that a circuit architecture could be used that has very short rise and decay times. An example of such a VAT circuit used for heavy ion bombardment in nuclear fusion applications where the short rise and fall times are critical to operation can be found in Liu et al. (1998). This region starts at t=90μs, approximately 10μs after the pulse begins to account for the pulse rise time, and ends 100μs later at t=190μs, before the traces begin to sharply decay - this region is expanded in figure 4.18. As can be seen in the figure, all of the traces are fairly constant in this region and their average values are summarised in the table below.

Arc Current (A)	Accel grid current (mA)	Screen grid current (mA)	Plate current (mA)
28.0 $\pm$2.24	1.2 $\pm$0.08	13.8 $\pm$1.10	10.1 $\pm$0.71

TABLE 4.4: Average values for the 100 microsecond long stable operating region at the beginning of the pulse.

These values can be considered realistic stable operation values for the ion thruster and are used in the following section to calculate the average performance of the thruster.

4.5 Performance Analysis

In this section an ion fraction of $f_i = 0.1$ and average charge state $\langle Z \rangle = 2.04$ are used for copper in the calculations, Daalder (1976); Oks et al. (2006); Anders et al. (2005). In terms of ion thruster performance there is one major inefficiency that must be dealt with first. Because the final VAIT (Design 3) grid system could only accommodate 190mA peak ion current (equation 3.3), and the minimum ion currents that could be produced from the final VAT used were over 1.5A - the maximum ion utilisation efficiency was limited to 10%. Then, because the VAIT was run at only $\approx 7 - 10\%$ of this maximum peak ion current, the ion utilisation efficiency

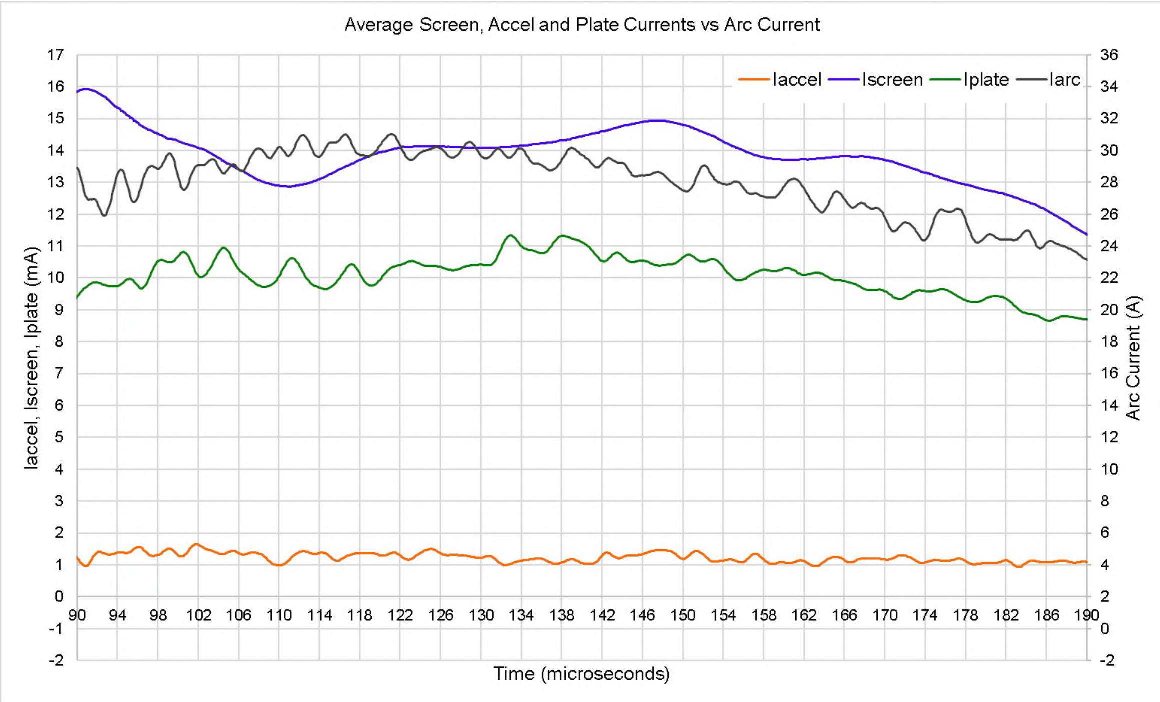

FIGURE 4.18: Stable operating point

was reduced again by a factor of 10. Therefore, before any of the other losses are taken into account, the ion thruster grid system could only use less than one percent of the ions that were produced by the VAT plasma source.

The thrust of a VAIT is given by equation 1.75,

$$T_{VAIT} = \frac{dm_{ib}}{dt} u_i = \frac{f_i I_d C_j \phi_g m_i}{e\langle Z \rangle} \sqrt{u_{VAT}^2 + \frac{2e\langle Z \rangle V_b}{m_i}} \tag{4.4}$$

The coefficients: ion fraction, discharge current, correction factor and grid transparency simply give the total ion current that is extracted by the grids. We have measured the total beam current as the plate current and so we use this value in the calculation. The cathode was copper, and the beam voltage is assumed to be the screen voltage, 1530V. For copper the average ion charge state is 2.04, and $u_{VAT} = 12800m/s$ Polk et al. (2008). Note that these values give an average ion beam energy of $E = e(V_b + V_{bVAT})\langle Z \rangle = (1530V + 54V) \times 2.04e = 3231eV$, see equations 1.81 and 1.71. Thus the average thrust during stable operation is:

$$T_{VAIT} = 10.1mA\frac{63.55m_a}{e \times 2.04}\sqrt{12800^2 + \frac{2e \times 2.04 \times 1530}{63.55m_a}} = 0.321mN \tag{4.5}$$

and the specific impulse is, assuming a mass loss of $35\mu g/C$ of arc charge,

$$I_{sp} = \frac{T}{E_r g} = \frac{0.321 \times 10^{-3}}{35 \times 10^{-9} \times 9.8 \times 28} = 33s \tag{4.6}$$

The total power used during this stable operating point is the sum of the arc discharge power, the screen grid power and the accel grid power.

$$P_t = P_d + P_s + P_a \tag{4.7}$$

The arc current is the measured average discharge current, the arc voltage is the standard literature value, 23.4V.

$$P_d = I_{arc} * V_{arc} = 28A * 23.4V = 655.2W \tag{4.8}$$

$$P_s = I_{screen} * V_{screen} = 13.8 * 10^{-3} \times 1530V = 21.1W \tag{4.9}$$

$$P_a = I_{accel} * V_{accel} = 1.2 * 10^{-3} \times 125V = 0.15W \tag{4.10}$$

Thus the total power drawn during stable operation (not accounting for circuit losses) is:

$$P_t = P_d + P_s + P_a = 655.2 + 21.1 + 0.15 = 676.45W \tag{4.11}$$

Thus the thrust to power ratio is then,

$$\frac{T}{P} = \frac{0.321}{0.676} = 0.474mN/kW \tag{4.12}$$

The total electrical efficiency of the thruster can be calculated as the ratio of the energy that produced a useful thrust, which is the total ion beam power $P_b = I_b V_{screen}$, to the total energy put in to create it,

$$\eta_e = \frac{P_b}{P_t} = \frac{10.1 \times 10^{-3} \times 1530}{676.45} = 2.28\% \tag{4.13}$$

which is very low because of the large ion current that took significant power to create in the VAT, but could not be accelerated by the grid system.

4.5.1 Pulsed operation

Both the VAT and VAIT are typically operated in pulsed mode to limit cathode heating. The calculations above were performed in the steady state for continuous operation. The VAT and VAIT could be run at a duty cycle up to 5% without excessive cathode melting, provided the cathode is large enough to transfer the heat load. Pulsed operation is an advantage to the VAT and VAIT compared to traditional systems because there is no sacrifice in efficiency at very low pulse rates - whereas in traditional systems, the thrusters have a much smaller thrust dynamic range because there are minimum mass flow rates and minimum propellant quantities required for efficient ionisation.

During ion thruster testing the thruster was run at 1 pulse every 1.5s for a repetition rate of 0.67Hz. The pulse length was approximately 320 μs in total although we only consider the first 100 μs to be the stable operating region. In the case of 320μs long pulses the duty cycle D is,

$$D_{320} = \frac{320\mu s}{1.5s} = 2.1 \times 10^{-4} = 0.021\% \tag{4.14}$$

And in the case of the 100 μs long stable pulses,

$$D_{100} = \frac{100\mu s}{1.5s} = 6.67 \times 10^{-5} = 0.0067\% \tag{4.15}$$

which leads to an average power consumption of,

$$P_{av} = D_{100} \times P_t = 0.045W \tag{4.16}$$

an extremely low power draw. Without the addition of cooling mechanisms, the thruster cathode would likely melt if operated at a duty cycle higher than 5%, Anders (2009). Therefore the maximum average power draw possible is,

$$P_{max} = 5\% \times 676.45 = 33.82W \tag{4.17}$$

Which is a reasonable power requirement for a small satellite, Wertz et al. (2011). At this power level the thrust produced would be,

$$T_{max} = 0.474\frac{mN}{kW} \times 0.03382kW = 16\mu N \tag{4.18}$$

4.5.2 Comparison with VAT

The thrust of the VAT from 1.66,

$$T_{VAT} = \frac{m_i f_i I_d u_i C_t}{e\langle Z\rangle} = \frac{63.55 * m_p * 0.1 * 28 * 12800 * 0.67}{e * 2.04} = 7.80mN \tag{4.19}$$

thrust to power ratio,

$$\frac{T}{P} = \frac{7.8}{0.6552} = 11.9mN/kW \tag{4.20}$$

specific impulse,

$$I_{sp,VAT} = \frac{T}{\frac{dm_t}{dt}g} = \frac{T}{E_r I_d g} = \frac{7.8 \times 10^{-3}}{35 \times 10^{-9} \times 28 \times 9.8} = 812s \tag{4.21}$$

and electrical efficiency using the effective VAT beam voltage from equation 1.81,

$$\eta_{e\ VAT} = \frac{P_b}{P_t} = \frac{0.1 \times 0.67 \times 28 \times 54}{28 \times 23.4} = 15.46\% \tag{4.22}$$

4.5.3 Theoretical best case performance

The reason why the VAIT tested in this work had very poor performance is the large mismatch between the ion current that could be extracted by the grids and the ion current produced by the VAT. If the grid system was scaled up to accommodate 90% of the ion current instead of the ≈ 1% in reality, or alternatively if the arc current was reduced so that the grid system could accommodate 90% of the ion current, then the performance would improve significantly. Both of these options should be feasible with careful design, to make the grids much larger is simple - but it would increase the size of the thruster significantly and it may no longer be suited to small satellites. Reducing the arc current, on the other hand - while not performed successfully in this work, should also be possible with careful circuit design. Puchkarev & Murzakayev (1990) showed vacuum arc operation with currents as low as $\approx 1A$. This would allow the grid system to remain roughly the same size that it is in this work, but be able to accommodate 90% of the ion current produced. In either case, the beam current would then become $0.9 \times 0.1 \times I_d$. We take the case of increasing the grid size and keeping the VAT arc current measured in this work as the key performance parameters of specific impulse and thrust to power ratio are independent of size. Recalculating the performance for this best case scenario and using the superscript^T to denote that it is a theoretical performance, in this case the beam current would become $0.9 \times 0.1 \times 28A = 2.52A$ and so the new screen power,

$$P_s^T = I_{screen} * V_{screen} = 2.52 \times 1530V = 3855.6W \tag{4.23}$$

It is also assumed that the grid system is designed properly and there is no ion beam impingement, therefore the accel power is neglected, $P_a = 0$, the discharge power is unchanged $P_d = I_{arc} * V_{arc} = 28A * 23.4V = 655.2W$ and the new total power would be,

$$P_t^T = P_d + P_s + P_a = 655.2 + 3855.6 = 4510.8W \tag{4.24}$$

The thrust at this beam current becomes,

$$T_{VAIT}^T = 2.52 \times \frac{63.55m_a}{e \times 2.04}\sqrt{12800^2 + \frac{2e \times 2.04 \times 1530}{63.55m_a}} = 80.2mN \tag{4.25}$$

and the thrust to power ratio,

$$\frac{T}{P}^T = \frac{80.2}{4.51} = 17.78mN/kW \tag{4.26}$$

at a very high specific impulse of,

$$I_{sp}^T = \frac{T}{\frac{dm_t}{dt}g} = \frac{T}{E_r I_d g} = \frac{80.2 \times 10^{-3}}{35 \times 10^{-9} \times 28 \times 9.8} = 8350s \tag{4.27}$$

The electrical efficiency of this theoretical VAIT would then be,

$$\eta_e^T = \frac{P_b}{P_t} = \frac{2.52 \times 1530}{4510.8} = 85\% \tag{4.28}$$

Operating at the maximum 5% duty cycle,

$$P^T_{max} = 5\% \times 4510W = 225.5W \tag{4.29}$$

which is likely too high for many small satellites, operating at 1% would solve this problem and make $P^T_{max} = 45.1W$ and give a thrust,

$$T^T_{max} = 1\% \times 17.78\frac{mN}{kW} \times 0.0451kW = 802\mu N \tag{4.30}$$

4.5.4 Effect of increased arc current

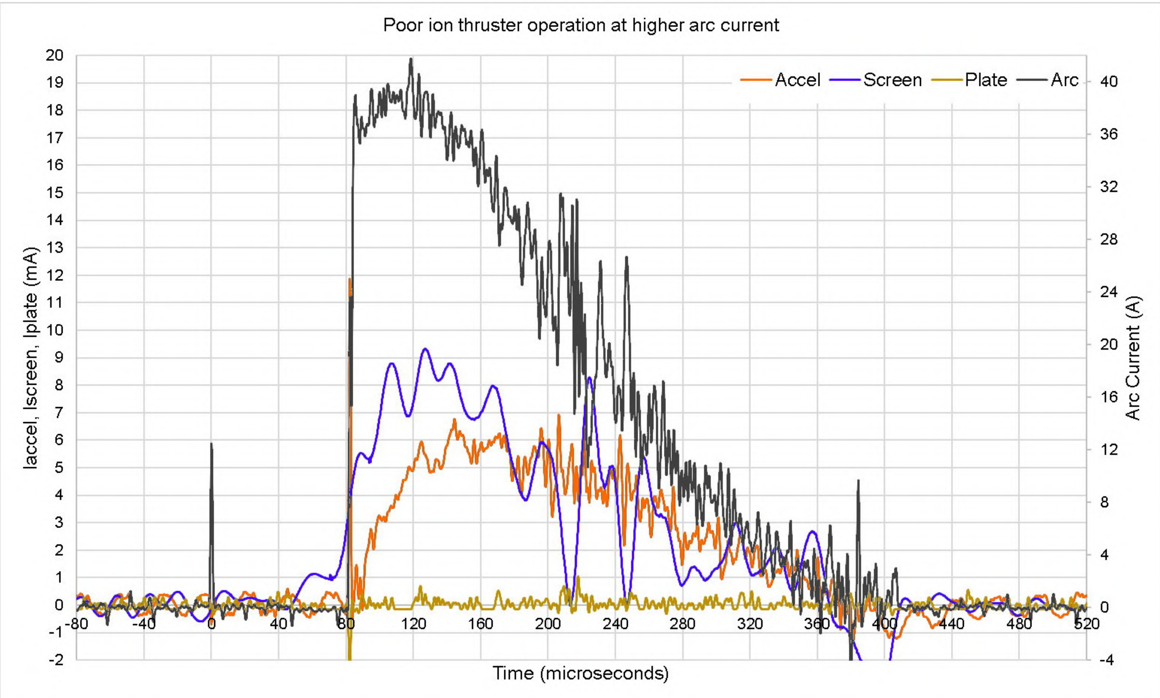

FIGURE 4.19: Current traces for moderately higher arc currents showing poor operation and the sensitivity of the grid system.

The ion thruster was very sensitive to changes in the operating parameters, especially the arc current. Some tests were run with an added 100 μF increased capacitance for a total of 324 μF. This resulted in peak arc currents of approximately 40A, as opposed to 30A that were seen with the 224 μF circuit. This moderate increase in the arc current, and thus the ion current dramatically reduced the performance as shown in figure 4.19. At just $40/30 \approx 33\%$ higher arc currents, the grid system can only accelerate approximately 8mA of ions and almost all of them impact the accel grid - leading to an almost undetectable signal on the plate. It is possible that the increased arc current produced more neutrals or some other flux that dramatically reduced performance, this possibility is discussed in the next chapter.

4.6 Feasibility of refuelling the VAT and VAIT from metallic asteroids

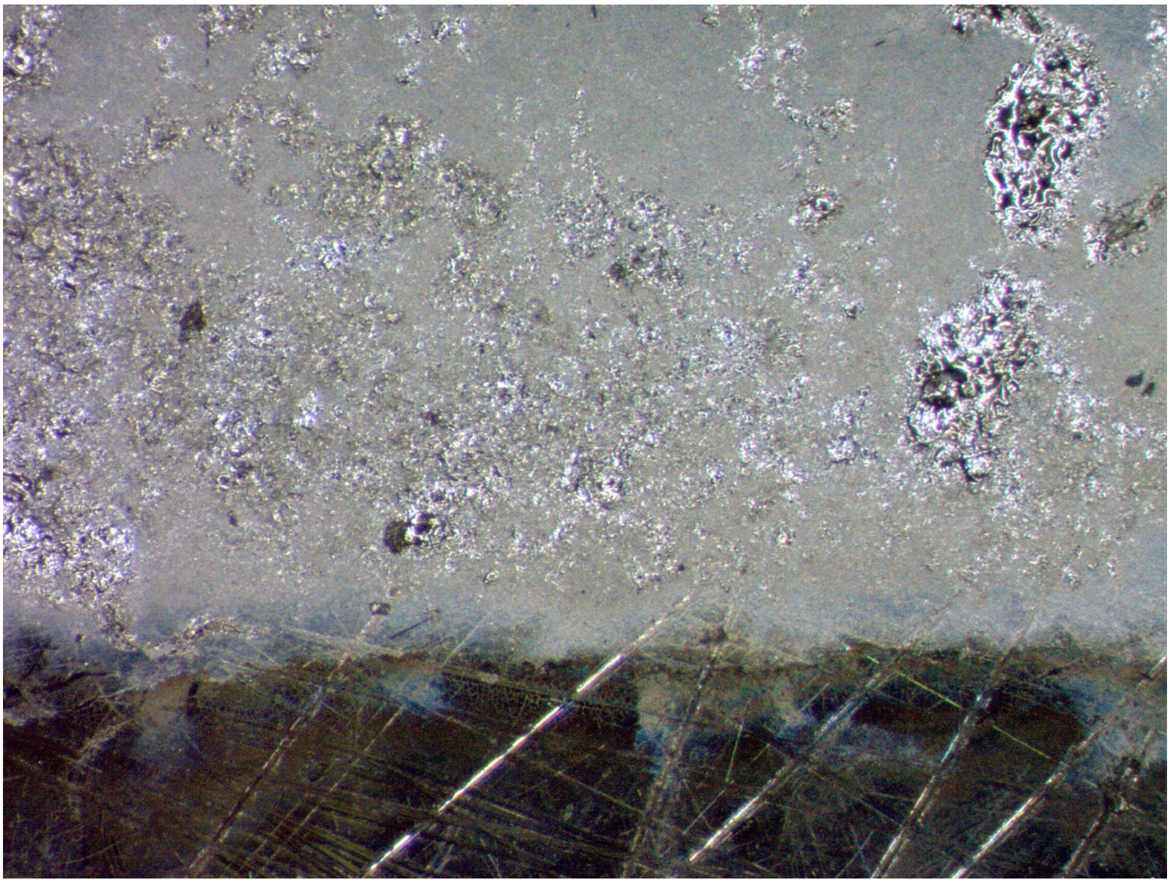

FIGURE 4.20: Micrograph showing the metallic meteorite sample surface. The boundary line where the glass insulator was is clearly visible in the lower third of the image. The lower region is dark because it is coated with carbon and has not been bombarded by plasma. Many cathode spot craters and traces are visible, but most are too small to be clearly seen at this low magnification of 3X. There are two large craters visible in the top right of the image, this region is expanded in figure 4.23 below.

To evaluate whether metallic meteorites could be used to fuel the VAT and VAIT, a metallic meteorite was used as the cathode in a planar VAT shown in figure 3.3. The test focused on determining whether the meteorite sample could produce a stable arc from which a stable ion current would arise which could be used in the VAIT. In this test the meteorite VAT was placed in the total ion collector shown in figure 2.2. The standard VAT circuit was used at 45.6V with a total capacitance of 4.87mF. The collector negative bias voltage was kept constant at -21V, rather than -60V. This was done to prevent the possibility of a direct current arc through the collector bias supply to the meteorite sample which could significantly damage it. Nonetheless, -21V bias was expected to block the vast majority of plasma electrons and still give a reasonably accurate picture of the ion current. Another factor influencing the ion current that could be measured was the geometry of the meteorite. The resin block encasing the meteorite shielded any plasma from escaping through that side of the thruster thereby reducing the ion current that could be measured by the collector.

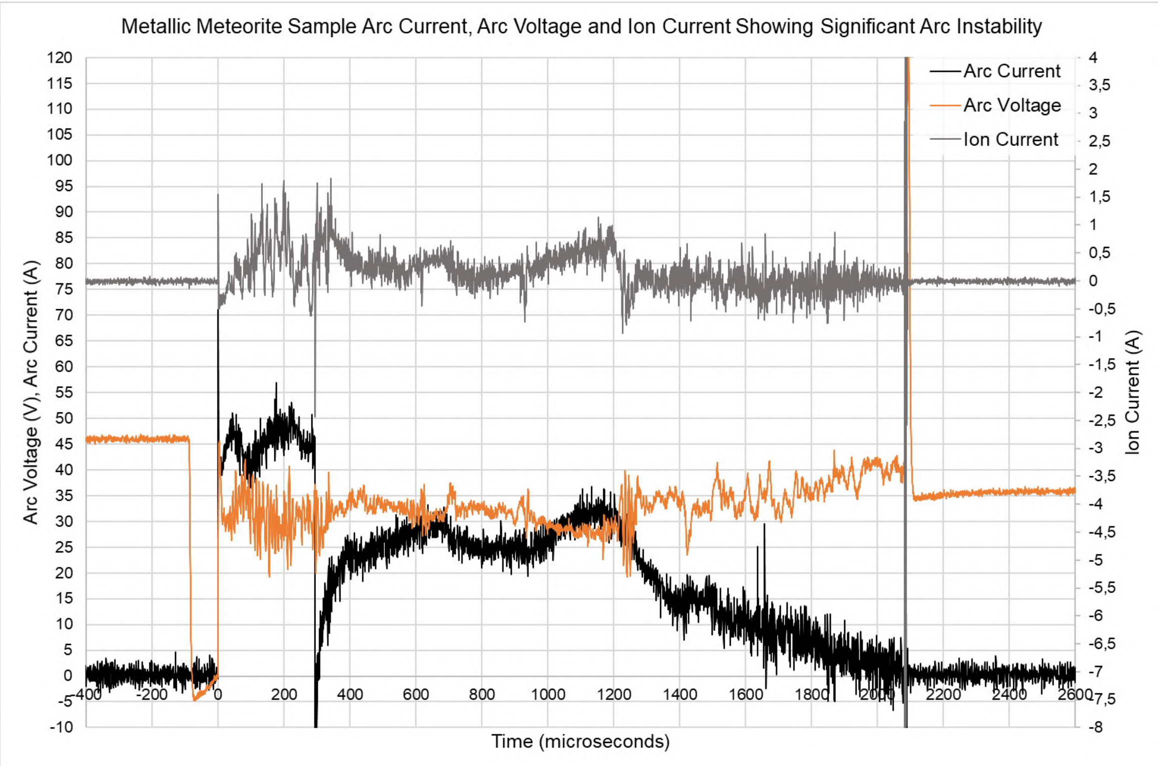

FIGURE 4.21: Arc current, arc voltage and ion current traces measured from the metallic meteorite VAT. Note especially the high arc voltage, low ion current and significant arc instability.

4.6.1 Unstable arc operation

Figure 4.21 shows the arc current, arc voltage and ion current from one arc pulse of the meteorite VAT. The arc current (black) and arc voltage (orange) are shown on the primary axis (left hand side) and the ion current is shown on the secondary axis (right hand side). Examining the arc voltage trace, the VAT circuit voltage is slightly above 45V and drops slightly below zero during the 80 μs square wave charge pulse which ends at t=0μs. After this the arc ignites as the square pulse ends and begins to burn reaching a peak above 50A within 200μs. Shortly thereafter, at t=300μs the arc rapidly extinguishes itself before recovering and continuing to burn until t=2000μs. This rapid arc extinction and re-ignition could be due to impurities such as volatiles in the meteorite. The average ion to arc current ratio for this pulse is only 0.98%. Iron and nickel both have arc burning voltages below 23V, Polk et al. (2008). So the fact that the measured burning voltage during the stable portions of the pulse is as high as 32V also warrants explanation. These questions are investigated in the next chapter.

4.6.2 Stable arc operation

Figure 4.22 shows another arc pulse, several pulses after the pulse shown in figure 4.21. This arc is much more stable showing a sharp rise to a 55A peak close to t=200μs and extinction at t=1200μs. The arc burning voltage is also significantly lower in this arc, reaching 27V at the arc current peak. Finally, the ion current is also significantly higher in this arc pulse for an average pulse ion to arc current ratio of 3.32%.

4.6.3 Large crater size difference

Figure 4.20 shows the boundary region of the meteorite cathode. The insulator protected the metal in the lower third of the image from any arc ignitions or plasma bombardment. The image shows multiple cathode spot craters scattered across the meteorite metal surface, with two large craters in the right side of the image. Because these craters are so much larger ($\approx$ 100) than the cathode spot craters seen in the center of the image it is unlikely that they were caused by nominal arc operation.

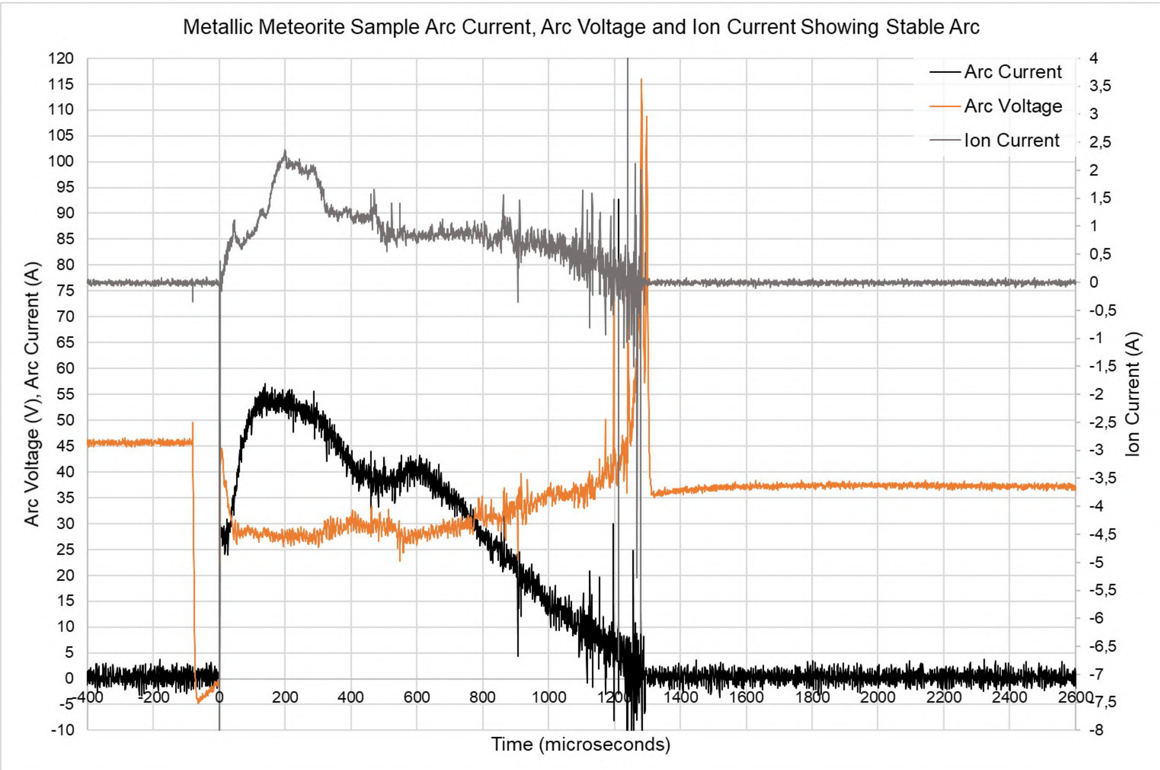

FIGURE 4.22: Arc current, arc voltage and ion current traces measured from the metallic meteorite VAT. Note the lower arc voltage, higher ion current and stable arc current in this pulse when compared to 4.21.

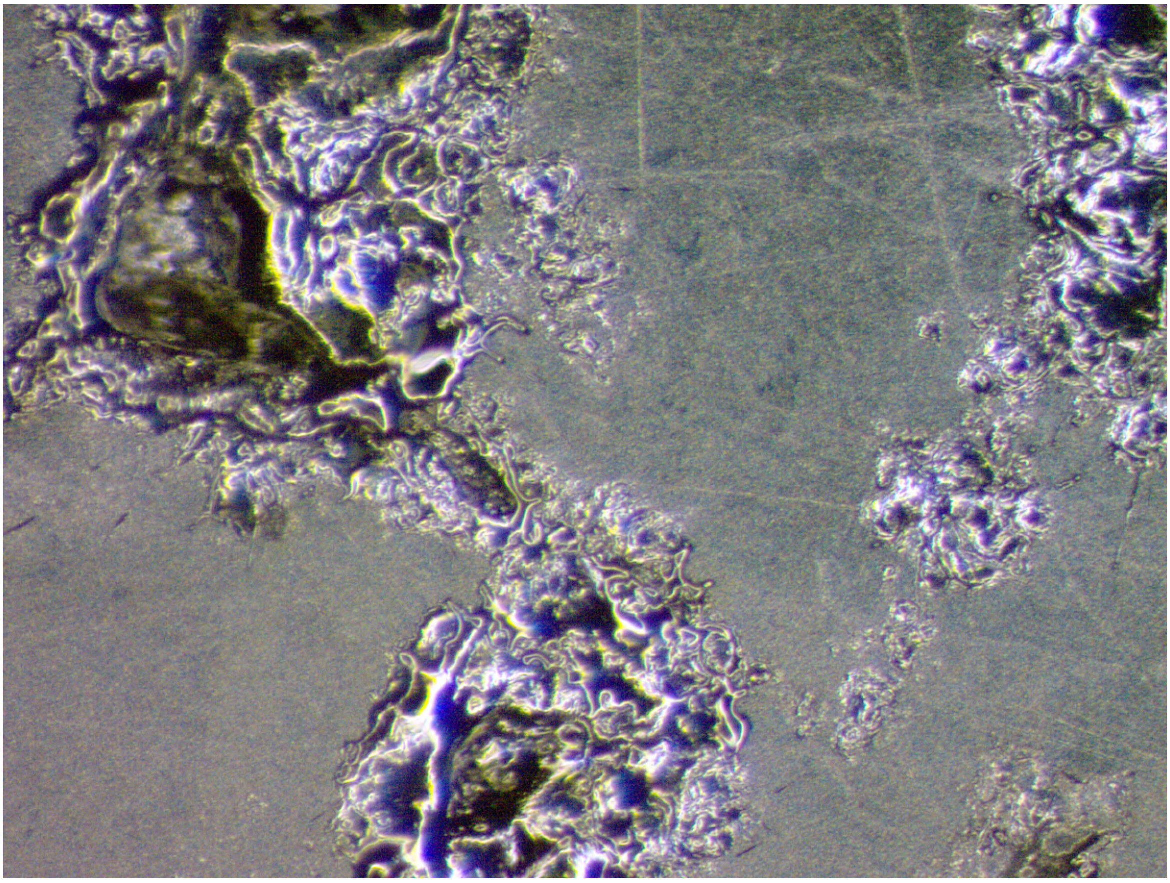

FIGURE 4.23: Micrograph of the metallic meteorite sample surface. This image is a close up of the region in the top right of figure 4.20, now at 8X magnification. The gaps between the craters show the pristine meteorite metal surface undamaged by the arc. Multiple cathode spot craters and molten metal are seen around these large craters. The large craters were most likely formed due to an impurity in the meteorite that was exposed by the arc.

Chapter 5

Discussion and Conclusions

5.1 Comparison with VAT

Theoretically the VAIT should have a higher thrust to power ratio than the VAT. This is because in an ion thruster the energy is split up between the ionisation and acceleration stages - with the bulk of energy typically going into the acceleration stage. Because the ion acceleration stage can be highly efficient (greater than 99%), even if the ionisation stage is only 10% efficient, a total system efficiency of $> 80\%$ is achievable, as was shown in theoretical performance calculations at the end of the last chapter. On the other hand, the highest efficiency the VAT can achieve is limited by the maximum ion fraction - a mostly unadjustable material dependent parameter that is less than 15% for the best fuels.

Despite this, the VAT still had a much higher thrust to power ratio than the VAIT tested. This was due to the fact that the ion thruster grid system only utilised a tiny fraction of the VAT ion current. Therefore a huge amount of energy was wasted producing ions that could not be used, which dramatically lowered both the efficiency and the thrust to power of the VAIT. In this chapter, the findings of this dissertation are discussed and attention is given to the reasons for the poor VAIT performance and high accel grid currents.

5.1.1 EMI from VAT and VAIT

A point worth considering is the electromagnetic interference (EMI) inherent in the electric/vacuum arc. One advantage that the VAIT has over the VAT is that the extremely electromagnetically noisy arc is shielded by the grid system in a manner reminiscent of commercial microwave oven shielding. The grid apertures used in this work were 1.5mm diameter, which is a common size for ion thrusters. EMI can be effectively shielded by a Faraday cage when the maximum size of the apertures in the cage in any direction is less than one quarter the wavelength of the radiation. This means that for the 1.5mm diameter grid apertures the highest frequency signal that would still be attenuated is:

$$\nu_{max} = 0.25 * \frac{c_0}{d_{grid}} = 0.25 * \frac{c_0}{1.5 * 10^{-3}} = 50GHz \tag{5.1}$$

The highest frequency currently used in mainstream satellite communications is Ka band which extends up to 40GHz - therefore it appears that the VAIT should have no problems with EMI on existing communications links, Amyotte et al. (2010). Additionally, this calculation is for a single grid, the two grid system used in this work should offer even better shielding and may provide effective EMI shielding up to higher frequencies less commonly used such as Q and W band, Biscarini et al. (2017). The VAT on the other hand relies on having a completely unshielded arc in at least one direction to allow for the plasma and vapors to escape the thruster. This could potentially cause problems if communications are intended to happen contiguously with thruster operation.

5.2 Problematic conductive buildup

In gas based ion thrusters, because the thruster operates at temperatures much higher than the propellant's boiling point (ie the propellant is a gas), any neutral or ionised propellant that impacts an insulator or any other thruster or spacecraft component is likely to simply bounce off and not deposit itself. In the VAIT however, as the propellants are metals and the thruster operates much below the boiling point of the propellant, any neutral or ionised propellant that encounters an inter-grid insulator or any other thruster or spacecraft component has a high likelihood of condensing on the surface, thereby creating a thin conductive layer. This was the biggest problem encountered with the ion thruster in this work. After fewer than 40 arc pulses, the plasma from the copper cathode would form thin conductive layer across the grid insulators and grid alignment wires - leading to a short circuit between the grids and the end of ion thruster operation. It is likely that using a copper cathode, the second most conductive metal, exacerbated this problem. The fact that only a very small fraction of the ions produced by the VAT were extracted by the grid system also could have increased this condensation problem, this factor is discussed more at the end of this chapter. Once this conductive layer had been formed, the grids had to be disassembled and the grids and insulators cleaned before operation could begin again. Obviously this is not practical for a satellite in space. The ion thruster design used in this work placed the grid alignment wires and insulators directly in line of site of the plasma. This was predicted to be an issue but due to time and resource constraints on the design it was the simplest way to keep the grids apart and the grid holes aligned. Experiments were run without the grid alignment wires but the grids quickly became misaligned and so it was necessary to keep the wires in place during thruster operation. In production ion thrusters, even those using gaseous propellant where condensation is not possible, great care is taken to avoid any insulator or other spacecraft component from coming into direct view of the ion beam. This is primarily to prevent erosion and sputtering from the high energy ions that could rapidly decay either the insulators or grid structures. It is likely that if the ion thruster built in this work used a similar design that kept the insulators and grid alignment wires out of line of sight of the plasma - thruster operation would have been possible for much longer periods. Examples of this type of sophisticated grid design can be found in Soulas et al. (1999), Soulas et al. (2002), and Kaufman & Robinson (1982). As these grid designs already exist and are always employed in flight rated thrusters, this point is not seen as a technical barrier to further VAIT development.

5.3 Unused fluxes influencing VAIT performance

5.3.1 Large unused mass flow rate

Comparing the total mass flow from the VAT with the ion current extracted, the total mass flow rate in the steady state for a copper vacuum arc ($E_r = 35\mu g/C$) at an arc current of 28A is,

$$\frac{dm_t}{dt} = 35\mu g/C \times 28A = 980\mu g/s \tag{5.2}$$

and the total ion mass flow rate through the grids from the measured 13.8mA screen current is,

$$\frac{dm_{i\ screen}}{dt} = 13.8mA \times \frac{63.55m_a}{2e} = 4.5\mu g/s \tag{5.3}$$

We find that the total mass flow rate is 214 times the total ion mass flow rate to the screen grid. This total mass flow rate is comprised of the following in descending mass order: ions, a significant number of liquid droplets known as macroparticles and a small amount of metal vapor, Daalder (1976). The macroparticles were not expected to affect the grid system as they are directed at low angles to the cathode surface, Mesyats & Zubarev (2015), and the VAT was 90mm away from the grid system. If the VAT was much closer to the grid system, as it would be in a more optimised design, it is possible that macroparticles could deposit themselves onto the screen grid and potentially also onto the accel grid. This could cause problems for long term thruster operation as a significant buildup of macroparticles could change the electric field shape around each grid hole and this could potentially affect beam formation and focusing leading to increased grid erosion and shorter thruster lifetimes. These issues, while important to consider in future research, do not affect the present work. While these droplets themselves were not expected to interact with the grid system, most of the neutral vapor is evaporated from these droplets, with a small contribution from cooling cathode spot craters, Daalder (1981). Therefore there are two fluxes that could be influencing the ion thruster performance results. Firstly, there is the large ion current considered to account for over 90% of the mass lost,

$$\frac{dm_{i\ total}}{dt} = 0.9 \times 35\mu g/C \times 28A = 882\mu g/s \tag{5.4}$$

and then there is the neutral vapor. Tuma et al calculated the neutral vapor flux from a copper vacuum arc using resonance line absorption. and found it to be between $1 - 2\mu g/C$, to account for 1-2% of the total erosion rate measured in their study, Tuma et al. (1978). Taking the lower bound of $1\mu g/C$, would give,

$$\frac{dm_n}{dt} = 1\mu g/C \times 28A = 28\mu g/s \tag{5.5}$$

So during VAIT operation, the ion current that does not get extracted by the grid system is 196 times the screen grid current, and the neutral vapor flux is over 6 times the screen grid current. With such large fluxes unrelated to the actual ion current through the grid system it is likely these large fluxes could cause undesirable phenomena leading to lowered ion thruster performance. Potential undesirable consequences of the ion flux and the neutral vapor are discussed below.

5.3.2 Unused ion current

The majority of this unused ion current will hit the glass walls of the plasma containment vessel with a smaller fraction impacting the screen grid. The average energy of these copper ions is:

$$\frac{1}{2} \times 63.55 m_a \times 12800^2 = 54 eV \tag{5.6}$$

Which is above the sputtering threshold of $\approx 40eV$ for silicon dioxide (the main component of the glass vessel), Todorov & Fossum (1988). Therefore this ion flux can be expected to sputter material from the glass vessel. A portion of these ions will also recombine and be re-emitted as neutrals. These ions and neutrals produced from recombination at the glass surface will eventually condense as the vessel surface is much below the freezing point of copper. Without more detailed knowledge on the compositions of each of these fractions, it is hard to speculate as to the effect of this sputtered material on the grid system and ion thruster performance. On the other hand, neutrals in ion thrusters are known to cause problems primarily through charge exchange collisions with beam ions. The effects of these neutrals are considered below.

5.3.3 Neutral vapor

A population of neutrals in the inter-grid region and just downstream of the accel grid can cause charge exchange collisions in the following way. Typically, a fast moving beam ion that has been accelerated by the inter-grid potential collides with a slow moving neutral atom, the charge is transferred and the fast moving beam ion becomes a fast moving neutral - and the slow moving neutral becomes a slow moving ion. These slow moving ions, unlike the high velocity beam ions, do not have sufficient energy to escape the accel grid potential. Instead they are attracted to it and impact the accel grid - increasing the accel grid current and causing accel grid erosion, Sangregorio et al. (2018). This occurs in the inter-grid region and downstream of the grid and is the main source of accel grid erosion which ultimately limits the lifetime of gridded thrusters, Goebel & Katz (2008). The cross section for symmetric charge exchange collisions in ion thrusters for xenon is of the order of 100Å^2, Miller et al. (2002). Assuming that the charge exchange collision cross section is similar for copper, we can estimate what proportion of the ions will encounter a neutral and produce a charge exchange collision. We may define the charge exchange cell parameter,

$$\zeta_{CEX} = NL\sigma \tag{5.7}$$

where N is the neutral density, L is the cell length, and σ is the charge exchange collision cross section, Dunning & Hulet (1996). For $\zeta_{CEX} = 1$ all of the ions passing through the charge exchange cell will experience a neutral collision. Integration of the averaged arc current during the ion thruster testing gives a total charge of $5.538mC$ during a single pulse. Using the value of $1\mu g/C$ of neutrals from Tuma et al. (1978) - the total number of neutrals produced per pulse is,

$$N_n = 1\mu g/C \times 5.538 \times 10^{-3} \times \frac{N_A}{63.55g} = 5.25 \times 10^{13} \tag{5.8}$$

Without a direct simulation Monte Carlo (DSMC) simulation, it is difficult to calculate the precise neutral density. Assuming that during the pulse the neutrals do not have time to condense and none are removed from the 1 liter volume system (before the pulse ends) then the neutral density will be,

$$N_n/V_{vessel} = 5.25 \times 10^{13} \times 1000\frac{l}{m^3} = 5.25 \times 10^{16}/m^3 \tag{5.9}$$

The background pressure in the vacuum chamber was measured to be $5 \times 10^{-8} Torr$. Since there are N_A molecules in $0.02478m^3$ of air at STP ($298K$, $100kPa$), the particle number per cubic meter is $\frac{N_A}{0.02478} = 2.43 \times 10^{25}$. The background particle density in the vacuum chamber is therefore,

$$5 \times 10^{-8} \times \frac{1}{760} \times 2.43 \times 10^{25} = 1.598 \times 10^{15}/m^3 \tag{5.10}$$

Therefore the neutral density, which is only a fraction of the total mass lost from the cathode, is significantly higher than the background gas density in the chamber. Taking the cross section to be 100 Å^2, setting the cell length L equal to the grid gap ($\approx 1mm$) and plugging in the neutral density calculated above,

$$\zeta_{CEX} = NL\sigma = 5.25 \times 10^{16} \times 10^{-3} \times 100 \times 10^{-20} = 5.25 \times 10^{-5} \tag{5.11}$$

from this low value of ζ_{CEX} we would not expect significant CEX collisions.

The neutral density calculated above assumed that the neutrals produced during the pulse would be distributed isotropically throughout the 1 liter vessel volume. However, pressure effects could increase the neutral density in the inter-grid region.

Pressure effects

The copper neutral particle density from the VAT is some 33 times the particle density of the background gas (mostly nitrogen). Using the ideal gas law we can estimate the pressure difference that would arise from this.

$$P = \frac{N}{V}kT \tag{5.12}$$

Neutrals from vacuum arcs have been found to have temperatures close to the melting point of the cathode material, Tuma et al. (1978). Therefore we assume $T_n = 1358K$ (the melting point of copper) and $T_{vac} = 300K$ (room temperature). The pressure ratio is then,

$$\frac{P_n}{P_{vac}} = \frac{N_n T_n}{N_{vac} T_{vac}} = \frac{5.25 \times 10^{16} \times 1358K}{1.598 \times 10^{15} \times 300K} = 148.7 \tag{5.13}$$

which would be further increased if the difference in atomic masses between neutral copper atoms and diatomic nitrogen is taken into account, $\frac{63.55}{28.02} = 2.3$.

If most of the neutrals do not immediately condense on the vessel walls this large pressure ratio could cause a pressure gradient force that would rapidly accelerate the neutrals out of the thruster and through the inter-grid region. This could dramatically increase the neutral density in the inter-grid region by several orders of magnitude, and thus would increase ζ_{CEX} by a similar factor. Furthermore this calculation only takes into account the pressure from the neutral vapor. The potential pressure gradient effect of the plasma pressure from the large unused ion flux is considered below.

Plasma kinetic pressure

The number of ions produced in a single pulse is,

$$35\mu C \times 5.538 \times 10^{-3} \times \frac{N_A}{63.55g \times 2.04} = 9.18 \times 10^{14} \tag{5.14}$$

If these ions spread out uniformly through the glass vessel then their density is,

$$n_i = 9.18 \times 10^{14} \times \frac{1000l}{m^3} = 9.18 \times 10^{17}/m^3 \tag{5.15}$$

the temperature of plasma in the cathode spot of a copper vacuum arc was determined by Utsumi (1971) to be 2570K. Taking this as the ion temperature gives us an upper bound on the plasma pressure from these ions,

$$P_{kin} = \frac{N}{V}kT = 9.18 \times 10^{17} \times k \times 2570 = 0.033Pa \tag{5.16}$$

The vacuum chamber pressure was $5 \times 10^{-8} Torr = 6.6 \times 10^{-6} Pa$. Therefore the pressure ratio from these ions would be on the order of $0.033/(6.7 \times 10^{-6}) = 5000$. Which is orders of magnitude higher than the neutral pressure ratio. The fact that only $\approx 30mA$ of ions made it to the screen grid suggests that the vast majority of ions and neutrals condense quickly on the vessel walls before entering the intergrid region.

Summary

In conclusion of this section, it is possible that the large unused mass flow rates affected the VAIT performance. The large unused ion mass flow rate could have sputtered material from the glass walls of the vessel or contributed to a higher neutral density. The neutral vapor density, if spread throughout the vessel isotropically was not expected to cause significant charge exchange collisions. It is possible that pressure effects from either the neutral pressure or the kinetic pressure of the plasma could have increased the neutral density in the intergrid region and increased ζ_{CEX}, which could explain to some extent the high accel grid current; however without further analysis or a DSMC simulation this is merely a conjecture.

5.3.4 Effect of increased arc current

As determined by the space charge calculation in 3.3 and the low measured screen and plate currents, the ion thruster was operating in a low ion current density, under-perveance regime far away from the space charge current maximum. Therefore a modest increase in the arc current was expected to modestly increase the ion current, and thus move the system closer to an optimal perveance regime with lower cross over grid interception. The fact that the opposite occurred with this marginally greater arc current was puzzling. After analysing the ion and neutral fluxes above it seems possible that at nominal operating levels with 30A peak arc currents, the system could have been experiencing charge exchange collisions and other unwanted effects related to the large unused ion and neutral fluxes. This could partially explain the high accel grid current of $\approx$ 10% during stable operation. The 30% increase in arc current, likely increased the unwanted effects to a point where stable ion thruster operation was not possible. This is likely why the ion thruster suffered such poor operation as shown in figure 4.19.

5.4 Comparison with existing ion thrusters

The National Aeronautics and Space Administration (NASA) State of the Art Small Satellite Technology Report comprehensively compiles and evaluates small satellite technology and it is used as a reference to compare the VAIT built in this work with existing propulsion systems for small satellites (Yost et al. (2022, NASA online report: Small Spacecraft Technology State of the Art Report)). The data below are updated as of October 2022. The BIT-3, PBI-40 and NPT30 are all RF ion thrusters. The Metal Plasma Thruster (MPT) is a vacuum arc thruster.

In order to make a comparison of the VAIT with existing propulsion systems, several assumptions were made. The upgraded plasma containment vessel used in Design 3 had a total volume of 1 liter. It is assumed all the electronics could be fit into 2 liters or 2000 cm^3. The best case performance value of 17.8mN/kW was used in the calculation, and it was assumed that this hypothetical VAIT would be run at

1% duty cycle for an average power of 45W. This best case is labelled theoretical, the actual measured performance is also shown for comparison.

Thruster (Manufacturer)	Propellant	Thrust mN	Specific Impulse s	Mass kg	Volume cm3	Power W
BIT-3 (Busek)	Iodine	1.15	2100	2.9	1616	75
PBI-40 (Pale Blue)	Water	0.17	500	1.8	1500	40
NPT30 (ThrustMe)	Xenon/Iodine	1.1	2400	1.7	2000	65
MPT (ASC)	Molybdenum	0.6	1756	0.85	700	50
VAIT (theor.)	Copper	0.80	8350	2	2000	45
VAIT (actual)	Copper	0.016	33	2	2000	34

TABLE 5.1: Table comparing the actual measured VAIT performance and theoretical best case VAIT performance to a number of existing RF gridded thrusters for small satellites (BIT-3, PBI-40 and NPT30) and a vacuum arc thruster (MPT ASC). Data from Yost et al. (2022, NASA online report: Small Spacecraft Technology State of the Art Report).

5.5 Recommendations for future research

The ion thruster built in this work had two major design flaws:

1. The placement of the insulators and grid alignment wires lead to rapid conductive layer buildup which ultimately led to grid arcing and the end of thruster operation after only 40-80 pulses.

2. The large inefficiency in the thruster due to the fact that the arc current could not be reduced to an appropriate level, therefore the ion grids only utilised a tiny fraction ($< 1\%$) of the ion current. This dramatically reduced the efficiency and thrust to power ratio of the thruster and may have contributed to the high accel grid current through neutral-ion charge exchange collisions.

The problems caused by these flaws have been discussed above in sections 5.2 and 5.3. In this section we make some recommendations for future research.

The conductive buildup could likely be solved simply with a more advanced grid design. The second problem would be easy to solve for larger satellites - the grids could simply be made large enough to accommodate the ion current. For smaller satellites the problem may be more difficult to solve. In this work, with the specific VAT designs and circuitry used, it was not possible to maintain stable arc pulse operation below approximately 28A. This meant that the minimum ion current was on the order of $f_i \times J_d \approx 0.1 \times 28 = 2.8A$ and the grid system could accept a maximum of only $0.19A$. The threshold current, which is the minimum current required to sustain a vacuum arc, has been measured for copper and appears to be approximately 1-2A (Muzyukin & Mikhailov (2021)). Although arcs near this level experience significant instability, through careful VAT and circuit design it should be possible to sustain arcs close to this level. With 2A arcs, the ion current would be only $0.1 \times 2 = 0.2A$, which is approximately the space charge current limit for the VAIT built in this work at 1500V, and therefore this ion current could be accommodated simply by raising the acceleration voltage. At this much lower ion current level it would be possible to utilise the entire ion current whilst still maintaining a small grid size (<100mm diameter). This would dramatically increase the thruster efficiency and provide a unique capability to very small satellites. However, more work must be done to prove whether VATs could be run for long periods at these much lower arc currents.

5.6 Potential for refuelling from metallic asteroids

As was shown in figure 4.21, the meteorite VAT experienced significant arc instability, higher than expected arc discharge voltages and lower than expected ion currents. Excessive carbon in the arc could be cause for the higher than expected arc voltage. However, if there was significant carbon in the arc then one would also expect to see a significant ion current, as carbon has the highest ion to arc current ratio of 19%, Anders et al. (2005). The fact that the ion current is significantly lower than the pulse shown in 4.22, which also had a low arc voltage, rules out the simple explanation of a carbon arc. Furthermore, there were several craters on the meteorite that were orders of magnitude larger than would be expected from nominal arc operation. This section investigates the composition of the parent meteorite, known as Sokoto, in order to explain these phenomena.

FIGURE 5.1: Acid-etched cut surface of a piece of Sokoto iron meteorite showing relatively coarse Widmanstatten texture. The silver lamellae are kamacite crystals; the darker lines and triangles between them are taenite, schreibersite and/or plessite (intergrowth structure). Base of sample 4.5 cm long. *Credit R.L. Gibson*

5.6.1 Metallic meteorites: background

Metallic meteorites such as Sokoto are composed almost entirely of the iron-nickel minerals kamacite and taenite, Reimold & Gibson (2010). Kamacite is a mineral that is composed of up to 7% nickel and the remainder iron, with small amounts of cobalt and other elements. It is a relatively common mineral in meteorites and is typically found in the form of elongated, parallel bands or lamellae that are oriented parallel to the crystallographic axis of the meteorite. Taenite, on the other hand, is a mineral that is composed of up to 65% nickel and the remainder iron, with small amounts of cobalt and other elements. It is typically found in the form of irregularly shaped grains or masses that are intergrown with kamacite. The main difference between kamacite and taenite is their nickel content. Kamacite has a lower nickel content than taenite, and as a result, it has a lower density and a lower melting point. Taenite, on the other hand, has a higher nickel content, which gives it a higher density and a higher melting point. These differences are important because they could affect the vacuum arc stability and the ion current produced.

Metallic meteorites can also contain volatile impurities such as carbon, sulfur, and phosphorus. These elements are considered volatile because they have relatively low boiling points and can easily vaporize under conditions of high temperature and low pressure, such as those found in the vacuum arc. Phosphorus is a relatively common impurity found in metallic meteorites, and it is often present in the form of the mineral schreibersite. Schreibersite is an iron-nickel-phosphide mineral that can form under reducing conditions, such as those found in the early solar system. It is often found as inclusions within other metallic minerals in meteorites. Other volatile impurities that can be found in metallic meteorites include nitrogen, oxygen, and noble gases in trace amounts, Badescu (2013).

5.6.2 Metallic meteorite sample: Sokoto

The meteorite sample used in this work was from the Nigerian Sokoto meteorite from 2008. Analysis of the meteorite performed by Professor Roger Gibson of the School of Geosciences, University of the Witwatersrand, Johannesburg, revealed it to be a nickel-iron meteorite with a coarse grained $> 1mm$ Widmanstatten texture shown in figure 5.1. Backscatter analysis of the meteorite sample (performed by Professor R.L. Gibson) is shown in figure 5.2.

5.6.3 Schreibersite and other impurities as an explanation for the arc phenomena

As shown in the SEM electron backscatter image in figure 5.2, the meteorite sample contains small, isolated pockets of schreibersite. There are also non-conductive impurities in the meteorite sample such as small silicate pockets seen as black blobs in the figure. It is possible that during the arc, the cathode spot could encounter such a pocket of schreibersite or another impurity. Under the intense conditions in the cathode spot, these volatiles could dissociate and rapidly evaporate from the meteorite surface - thereby leaving behind a much larger crater, as seen the micrograph in figure 4.23. The arc encountering these impurities likely lead to the significant arc instability, higher than expected arc burning voltage and lower than expected ion currents in figure 4.21.

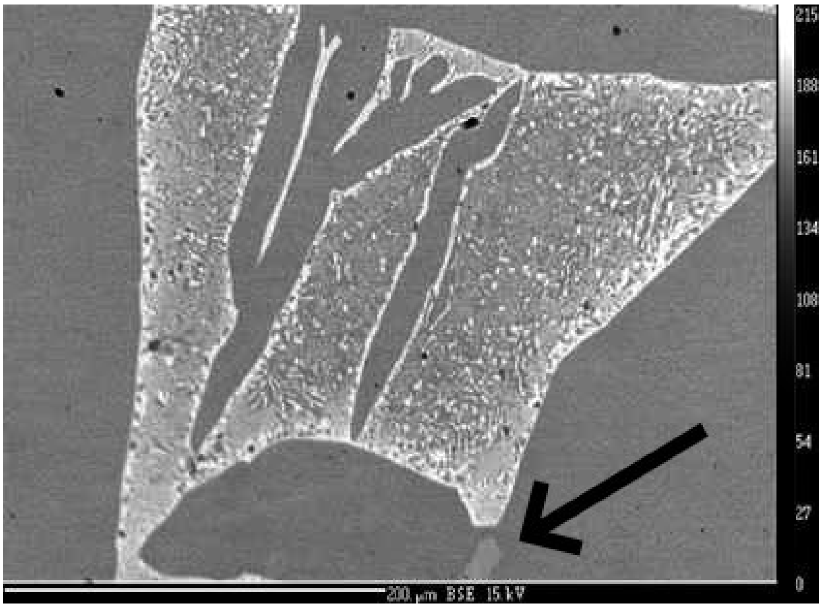

FIGURE 5.2: Backscatter electron image of plessite intergrowth between kamacite and taenite lamellae in Sokoto meteorite. Dark-grey – kamacite, white – taenite, black – silicate. The lighter grey phase at bottom, centre (see the arrow) is the Ni-Fe phosphide schreibersite. *Credit R.L. Gibson*

5.6.4 Conclusion on feasibility of using metallic meteorites as fuel for VAIT

From the results obtained in figures 4.21 and 4.22 and the analysis above - it can be concluded that metallic meteorites could provide a valuable source of propellant for the VAIT as long as the VAIT can handle certain periods of arc instability. The arc instabilities observed in this work were most likely caused by volatile impurities and did not cause failure of the VAT. During these unstable periods, VAIT performance would be reduced and it is possible that neutrals evaporated from these pockets could cause increased CEX collisions in the beam. The degree to which this could cause problems to the VAIT is highly dependent on the composition of the meteorite in question. If the meteorite is composed of a high percentage of volatiles and other impurities, it may be difficult to operate the VAIT for extended periods using this as a fuel source. However, from the limited testing conducted in this work, the impurities in this Sotoko sample did not pose a serious problem to reliable VAT operation. The meteorite sample that was used as the cathode had simply been cut and cast in resin for its previous analysis. This is promising as it suggests that a metallic asteroid could most likely simply be cut and an anode attached, as shown in figure 3.3, and used as fuel with no further processing required.

5.7 Concluding remarks

In this work, the vacuum arc thruster and vacuum arc ion thruster were introduced in the context of electric propulsion and their relevance to small satellites and potential in-space refuelling applications highlighted. The basic plasma physics relevant to gridded ion thrusters was presented including derivations of the Debye length, Bohm criterion and the Child-Langmuir equation. The performance figures of merit for vacuum arc propulsion systems were then derived and discussed. Several different vacuum arc thrusters, plasma containment vessels, grid systems and related circuitry were developed ab initio and described. Various pieces of measuring equipment such as custom current transducers and ion collectors were also built and their performance and limitations discussed. Grid arcing was a frequent phenomenon and significant effort was put into diagnosing and fixing the causes of the arcing. A miniature, low power vacuum arc ion thruster (and vacuum arc thruster as plasma source) which required only a few watts of average power and took up only 1 liter of volume excluding electronics was finally built. This VAIT used a modified coaxial VAT with an extended anode grid as the plasma source and a two grid acceleration system. Pulsed ion beams of up to 20$\pm$1.4mA, 3.23 $\pm$ 0.22keV copper ions lasting approximately 320 μs were successfully delivered to a collector plate downstream of the thruster. The copper cathode used as the fuel was much denser and cheaper than existing gridded ion thruster fuels. Therefore both primary objectives of this study were accomplished.

The VAIT performance was then calculated from the measured parameters and compared to the VAT. Due to a large mismatch between the ion current produced from the VAT and the ion current extracted and accelerated by the grid system the VAIT performance was shown to be inferior to that of existing gridded ion thrusters and the simple VAT. The VAIT built in this study had an electrical efficiency of $\eta_e = 2.28\%$, a thrust to power ratio of $0.474 mN/kW$, and a specific impulse of just

33s. If run at a duty cycle of 5% the VAIT would produce 16μN of thrust and consume 33.82W of power.

The thruster was operated in an under-perveance regime far from the space charge limit. This was confirmed through calculations and an analysis of the accel grid to screen grid current ratio during the pulse. Operating in this regime caused a high screen grid current fraction of approximately ten percent. Ion neutral collisions may have also played a role in increasing the screen grid current and this was briefly investigated. Ion thruster operation was only possible for $\approx$20 pulses due to a conductive buildup on the grid insulators and grid alignment wires that led to arcing.

VAT tests were also performed with a metallic meteorite as cathode. Despite some instabilities in the arc for the majority of pulses the VAT operated nominally and produced a suitable ion current. The arc instability was likely caused by schreibersite, which was known to be in the sample, or possibly another volatile impurity. These tests strongly suggest that the VAT/VAIT could be refuelled from a metallic asteroid with limited processing required, an exciting possibility.

In conclusion this work successfully accomplished both the primary and secondary objectives. This study adds a novel, miniature, low power and low beam voltage design to the limited literature on vacuum arc ion thrusters. Whilst still a very immature technology, the vacuum arc ion thruster may have applications as a future propulsion system for small satellites and in space refuelling applications.

Appendix A

Additional Material

A.1 Abandoned Measurement Attempts

A.1.1 Micro-controller voltage measurement attempts

Initially, it was thought that a micro-controller (STM32 Nucleo) with its voltage reading function could have sufficient accuracy to measure the various voltage signals in this work - so long as they were transformed to voltages between 0 and 3.3V. Some progress was made in this area, and using a micro-controller in communication with the main computer board (Raspberry Pi 3), was demonstrated to work. However, due to the lack of any shielding of the board or its measurement connections, a huge amount of electromagnetic interference (EMI) likely from the high voltage inductive trigger pulse and the arc burning was picked up by the micro-controller and could not be eliminated. Thus the idea was abandoned.

A.2 Long arc pulses

As the VAT and VAIT are pulsed devices. Their thrust is simply proportional to the impulse bit of each pulse multiplied by the repetition rate. In this way: the key figure of merit for both devices is the impulse bit. Due to the relatively low arc currents and arc pulse lengths used in this work <100A and <1ms respectively. The impulse bit of a single pulse is extremely small and very difficult to measure. In order to increase the ease of measurement the arc current or the arc pulse length could be increased. Increasing the arc current has drawbacks as even for low VAT arc currents. 50A, implies 2-5A of peak ion current which is already a major challenge to accommodate by the grid system. If this were increased by a factor of 10 to 500A arc current implying 20-50A peak ion current the situation would become untenable for the grid system. Thus it was decided to increase the arc pulse length. This was done by adding several stages to form a pulse forming network and increasing the capacitor values. Unfortunately, due to the nature of the circuit design by increasing the capacitor values it can increase the arc current peak and to some extent this is unavoidable.

With a three stage PFN and over 40mF of total capacitance, arc pulse lengths of up to 35ms with peak arc currents of 60-80A were produced. Some major downsides to these extremely long pulses were noticed. The major problem of the long arc pulses is the greatly increased heat load that the thruster has to process, akin to a welding arc in many ways. In the planar thruster, epoxy glue was used to hold the rectangular electrodes together over the glass slide insulator. The long arc pulses caused significant damage to this glue which lead to significant outgassing in the vacuum environment. The arc color was observed to change from the characteristic blue tone of the steel arc to a red glow from the glue compounds melting and outgassing. See figure A.1.

While the planar thruster glue caused problems, the large size of the electrodes was sufficient to not cause any gross melting of the actual cathode. The fact that the cathode was steel also played a significant role in this.

This was not the case for the coaxial thruster which had a comparatively much smaller cathode volume of 6.35mm x height. And it is believed that gross melting of the cathode occurred for every material tested.

Note on material properties and erosion rates

Three factors influence the degree to which the cathode can melt and cause extensive neutral production. Firstly the melting point of the material plays a big role. Second the thermal conductivity: if the cathode material conducts heat well, then the heat will be effectively conducted away from the surface of the cathode and less likely to cause melting. Finally the electrical resistivity plays a large role: if the electrical resistance is high, then the cathode will receive more heat load due to I^2R heating. This is complicated by the fact that the main heat source is ion bombardment but remains a concern.

FIGURE A.1: Camera still frame showing planar thruster firing an extended arc pulse of approximately 40ms. The arc color is characteristically blue/purple but in this frame it is clearly seen to be yellow. This frame was taken from the last few ms of the arc pulse, showing clear signs that the glue binding the planar anode and cathode together had suffered an intense heat load and began to melt.

Thus if we compare copper and bismuth it is clear that copper should be much more resistant to melting. While this is true, beyond a certain heat load any cathode material will melt and produce large numbers of neutrals Mesyats (1995).

A.3 Initial ion thruster designs

A.3.1 Design 1: Glass funnel design and hand drilled grids

The initial design used a 125mm glass funnel for plasma containment. The VAT source was placed in the throat of the funnel with the wires leading back down the tube. The initial grid design consisted of a set of two stainless steel plates with hand drilled aperture holes. As shown in figure A.2.

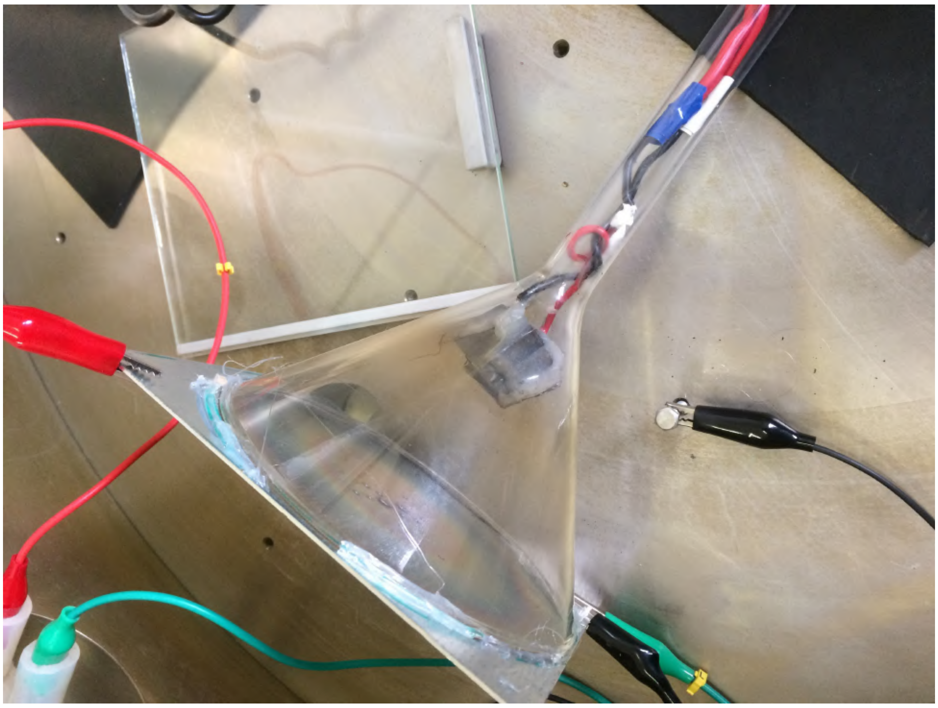

FIGURE A.2: Glass Funnel Design

The biggest issue with this design was the fact that the plasma source was far too close to the grids for proper operation to occur. Furthermore, the throat of the funnel was not completely sealed which also could have contributed to the grid arcing that was observed. The initial coaxial VAT had to be placed very close to the grids because there was limited space in the funnel and this contributed to the grids receiving extremely large peak ion currents which they simply could not accommodate. To alleviate these issues, a mini VAT was developed which was small enough to fit inside the throat of the funnel. In this way, the mini VAT could be moved forwards and backwards which changed the plasma flux to the grids. While this miniature VAT did manage to reduce the ion current density to a level where stable operation could occur, because the VAT was down the throat of the funnel, the plasma that did come out was extremely well collimated and resembled a beam with the same diameter as the funnel throat. This meant that a very small portion of the grids was saturated with an extremely high ion current density that it could not accommodate, while the rest of the grid system received almost no ions at all as seen in figure A.3.

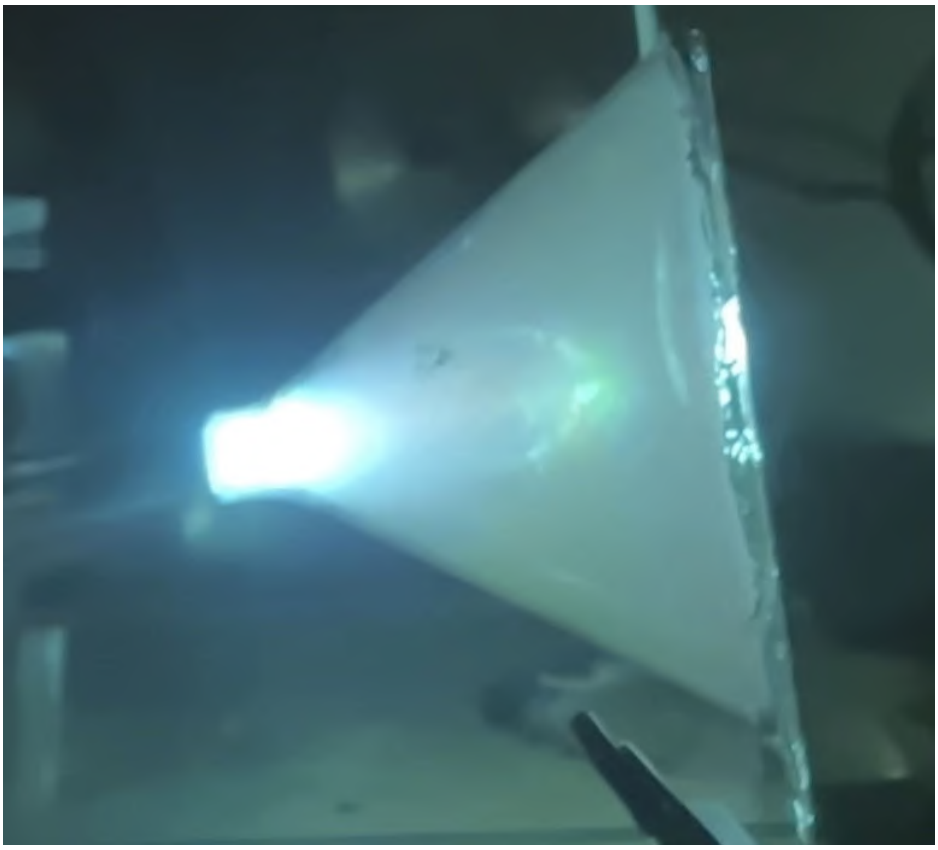

FIGURE A.3: Glass Funnel Thruster with mini-VAT in the throat of the funnel, note the collimated plasma jet presented to the grids.

The hand drilled grids were held apart by plastic bolts with 3mm nuts placed between them. This large grid gap considerably reduced the maximum electric field that could be attained and likely also contributed to the grid arcing.

A.3.2 Design 2: First cylindrical glass vessel

Next, a cylindrical glass vessel was used as the containment vessel for the plasma. This vessel, being much larger than the funnel and cylindrical in shape, allowed more flexibility in moving the VAT back and forth to reduce/increase the ion current density without collimating the ions into a narrow beam. Additionally, the vessel opening was smaller than the main cylinder of the vessel body, which was also thought to provide a somewhat more uniform plasma density to the grids. Furthermore a better grid material was used. 1mm stainless steel 1.5mm apertures 35% transparency was used for the grids.

Unfortunately, this vessel had no openings in the back for the VAT wires, and no holes were drilled to provide for this. This meant that the VAT wires had to come through the front of the grid system leading to many issues properly sealing and aligning the grids.

Bibliography

Amyotte, E., Demers, Y., Hildebrand, L., et al. 2010, in Proceedings of the Fourth European Conference on Antennas and Propagation, IEEE, 1–5

Anders, A. 1997, Physical Review E, 55, 969

Anders, A. 2009, Cathodic arcs: from fractal spots to energetic condensation, Vol. 50 (Springer Science & Business Media, New York)

Anders, A. 2012, Plasma Sources Science and Technology, 21, 035014

Anders, A., Brown, I. G., MacGill, R. A., & Dickinson, M. R. 1998, Journal of Physics D: Applied Physics, 31, 584

Anders, A., Oks, E. M., Yushkov, G. Y., et al. 2005, IEEE Transactions on plasma science, 33, 1532

Anders, A., Schein, J., & Qi, N. 2000, Review of scientific instruments, 71, 827

Anders, A., Yotsombat, B., & Binder, R. 2001, Journal of Applied Physics, 89, 7764

Aslanov, V. S. & Yudintsev, V. V. 2013, Journal of Guidance, Control, and Dynamics, 36, 1654

Badescu, V. 2013, Asteroids: Prospective energy and material resources (Springer Science & Business Media)

Biscarini, M., Montopoli, M., & Marzano, F. S. 2017, IEEE Transactions on Antennas and Propagation, 65, 1311

Boxman, R. L. 2001, IEEE transactions on plasma science, 29, 759

Brophy, J. R., Friedman, L., & Culick, F. 2012, in 2012 IEEE Aerospace Conference, IEEE, 1–16

Brown, I. G. 1994, Review of scientific instruments, 65, 3061

Brown, I. G. 2004, The physics and technology of ion sources (John Wiley & Sons)

Brown, I. G. & Shiraishi, H. 1990, IEEE transactions on plasma science, 18, 170

Calla, P., Fries, D., & Welch, C. 2018, arXiv preprint arXiv:1808.05099

Chabert, P. & Braithwaite, N. 2011, Physics of radio-frequency plasmas (Cambridge University Press)

Chen, F. F. et al. 1984, Introduction to plasma physics and controlled fusion, Vol. 1 (Springer)

Daalder, J. 1976, Journal of Physics D: Applied Physics, 9, 2379

Daalder, J. 1981, Physica B+ C, 104, 91

DeCarlo, S., Goodman, S., & Riker, D. A. 2022, A Pe Model of Neon exports from Ukraine (US International Trade Commission)

Dunning, F. B. & Hulet, R. G. 1996, Atomic, molecular, and optical physics: Atoms and molecules (Academic press)

Foster, J., Haag, T., Kamhawi, H., et al. 2004, in 40th AIAA/ASME/SAE/ASEE Joint Propulsion Conference and Exhibit, 3812

Francombe, M. H. & Vossen, J. L. 1994, Plasma sources for thin film deposition and etching, Vol. 18 (Elsevier)

Goebel, D. M. & Katz, I. 2008, Fundamentals of electric propulsion: ion and Hall thrusters, Vol. 1 (John Wiley & Sons)

Grondein, P., Lafleur, T., Chabert, P., & Aanesland, A. 2016, Physics of Plasmas, 23, 033514

Hantzsche, E. 1983, Beiträge aus der Plasmaphysik, 23, 77

Haque, A. F., Haque, M., Sultana, S., et al. 2019, Results in Physics, 15, 102519

Haque, S. E., Keidar, M., & Lee, T. 2013, in 33rd International Electric Propulsion Conference

Hashmi, M. S. J. 2014, Comprehensive materials processing (Newnes)

Hein, A. M., Matheson, R., & Fries, D. 2020, Acta Astronautica, 168, 104

Herman, D. A. & Unfried, K. G. 2015, in JANNAF SPS Subcommittee Meeting No. GRC-E-DAA-TN23198

Herniter, M. E., Lipscomb, G., & Pearce, K. D. 1989, High-Current-Density Thermionic Cathodes and the Generation of High-Voltage Electron Beams, Tech. rep., Finaly Technical Report, Office of Naval Reasearch, Michigan Univ. Ann Arbor Dept. of Electrical Engineering and Computer Science

Kaufman, H. R. & Robinson, R. S. 1982, AIAA Journal, 20, 745

Keidar, M., Schein, J., Wilson, K., et al. 2005, Plasma Sources Science and Technology, 14, 661

Keidar, M., Zhuang, T., Shashurin, A., et al. 2014, Plasma Physics and Controlled Fusion, 57, 014005

Kimblin, C. 1973, Journal of Applied Physics, 44, 3074

Kittel, C. & McEuen, P. 2018, Introduction to solid state physics (John Wiley & Sons)

Kolbeck, J. & Keidar, M. 2019, in Proceedings of the 36th International Electric Propulsion Conference, Vienna, Austria, 15–20

Kolbeck, J., Keidar, M., & Anders, A. 2016, in 52nd AIAA/SAE/ASEE Joint Propulsion Conference, 5040

Lafleur, T. & Rafalskyi, D. 2018, Plasma Sources Science and Technology, 27, 125004

Liu, F., Qi, N., Gensler, S., et al. 1998, Review of scientific instruments, 69, 819

Lun, J. 2013a, University of the Witwatersrand, South Africa, PhD Thesis, Performance improvement of vacuum arc thrusters

Lun, J. 2013b, Vacuum-Arc Asteroid Thurster (VAST)–A Design Concept for an Asteroid Space Transportation System

Medina, A., Tomassini, A., Suatoni, M., et al. 2017, Acta Astronautica, 134, 1

Mesyats, G. 1995, IEEE transactions on plasma science, 23, 879

Mesyats, G. & Zubarev, N. 2015, Journal of Applied Physics, 117, 043302

Miller, J. S., Pullins, S. H., Levandier, D. J., Chiu, Y.-h., & Dressler, R. A. 2002, Journal of Applied Physics, 91, 984

Muzyukin, I. & Mikhailov, P. 2021, Journal of Physics: Conference Series, 2064, 012015

Ngoc, N. M., Viet, D. T., Tien, N. H., et al. 2022, International Journal of Mechanical Engineering, 7, 633

Nikolaev, A., Oks, E., Savkin, K., Yushkov, G. Y., & Brown, I. 2012a, Review of scientific instruments, 83, 02A501

Nikolaev, A., Yushkov, G. Y., Savkin, K., & Oks, E. 2012b, Review of Scientific Instruments, 83, 02A503

Oks, E. M., Savkin, K. P., Yushkov, G. Y., et al. 2006, Review of scientific instruments, 77, 03B504

Piel, A. 2017, Plasma physics: an introduction to laboratory, space, and fusion plasmas (Springer)

Polk, J. E., Sekerak, M., Ziemer, J. K., et al. 2001

Polk, J. E., Sekerak, M. J., Ziemer, J. K., et al. 2008, IEEE Transactions on Plasma Science, 36, 2167

Puchkarev, V. & Murzakayev, A. 1990, Journal of Physics D: Applied Physics, 23, 26

Qi, N., Gensler, S., Prasad, R., et al. 1998, in 34th AIAA/ASME/SAE/ASEE Joint Propulsion Conference and Exhibit, 3663

Rafalskyi, D., Martínez, J. M., Habl, L., et al. 2021, Nature, 599, 411

Reimold, W. U. & Gibson, R. L. 2010, Meteorite Impact!: The Danger from Space and South Africa's Mega-Impact The Vredefort Structure, Vol. 1 (Springer Science & Business Media)

Ross, S. D. 2001, Space, Control and Dynamical Systems, Caltech 107-81, Pasadena, CA 91125, 1

Räisänen, O. 2012, Picture: Electrostatic ion thruster-en

Salter, A. W. 2016, Asteroid Mining 101: Wealth for the New Space Economy

Sanchez, J. & McInnes, C. 2011, Journal of Spacecraft and Rockets, 48, 153

Sangregorio, M., Kan, X., Ningfei, W., Ning, G., & Zhang, Z. 2018, Chinese Journal of Aeronautics, 31, 1635

Soulas, G. C., Haag, T. W., & Patterson, M. J. 2002, in 38th Joint Propulsion Conference and Exhibit No. AIAA Paper 2002-3834

Soulas, G. C., Haag, T. W., Patterson, M. J., & Rawlin, V. K. 1999, in 26th International Electric Propulsion Conference No. NASA/TM-1999-209650

Svensson, B., Holmén, G., & Burén, A. 1981, Physical Review B, 24, 3749

Tani, Y., Tsukizaki, R., Koda, D., Nishiyama, K., & Kuninaka, H. 2019, Acta Astronautica, 157, 425

Todorov, S. & Fossum, E. 1988, Applied physics letters, 52, 365

Tsiolkovsky, K. E. 1903, The Science Review, 5

Tuma, D., Chen, C., & Davies, D. 1978, Journal of Applied Physics, 49, 3821

Umstattd, R., Carr, C., Frenzen, C., Luginsland, J., & Lau, Y. 2005, American journal of physics, 73, 160

Utsumi, T. 1971, Applied Physics Letters, 18, 218

Waits, R. K. 2001, Journal of Vacuum Science & Technology A: Vacuum, Surfaces, and Films, 19, 1666

Wertz, J. R., Everett, D. F., & Puschell, J. J. 2011, Space mission engineering: the new SMAD (Microcosm Press)

Wirz, R. E., Katz, I., Goebel, D. M., & Anderson, J. R. 2011, Journal of Propulsion and Power, 27, 206

Yárnoz, D. G., Sánchez, J.-P., & McInnes, C. R. 2013, Celestial Mechanics and Dynamical Astronomy, 116, 367

Yost, B., Weston, S., Benavides, G., et al. 2022, NASA online report: Small Spacecraft Technology State of the Art Report